

Magnetoresistance in Composite Thin Films

Magnus Siegfried Rummey

Master of Philosophy (MPhil)

The University of York
Department of Electronics

September 2013

Abstract

In this work the magnetic properties of epitaxial co-evaporated Fe:MgO anti-granular films have been investigated. These films consist of MgO nanoparticles in an Fe matrix. Fe and MgO were co-evaporated on MgO(001) substrates in the ratio of Fe:MgO = 4:1, 3:1, 2:1 and 1:1 and ex-situ annealed in steps of one hour up to 6 hours enhancing the uniaxial anisotropy and saturation magnetization. An alternating gradient force magnetometer (AGFM) and a vibrating sample magnetometer (VSM) were used to determine the magnetic properties of the films. An enhancement of the saturation magnetization of up to 20 % was found. The Fe:MgO = 1:1 samples showed magnetisation reversal which was dominated by dipole-dipole interactions, whereas for higher Fe content samples the reversal was dominated by intergranular exchange interactions. The samples show different indications of thermally activated grains, in particular the Fe:MgO = 1:1 as deposited sample seems to have a large fraction of these grains. A 4-point-probe-system was used for magnetoresistance measurements. Isotropic and anisotropic components of magnetoresistance (MR) were found. The MR probably originates from anisotropic MR (AMR) and granular giant MR (GMR) and/or granular tunnelling MR (TMR) effects. The MR measurements support the conclusions from the magnetization measurements regarding the magnetic reversal mechanisms in the films. The previously existing MR measurement system was modified and most of the existing code of the measurement program was rewritten and extended. By doing so the reproducibility of the measurements improved from $\pm 0.2\%$ for MR [1] down to $\pm 0.0001\%$ for optimal measurement conditions. A program to calibrate the Gauss probe to a secondary standard probe was written.

Contents

Table of Contents	5
List of Figures	9
List of Tables	13
Acknowledgements	15
Declaration	17
1 Introduction	19
1.1 Overview	19
1.2 Applications	20
1.3 Presentations and Publications	21
2 Magnetism and Magnetoresistance	23
2.1 Magnetism of Thin Films	23
2.2 Domain Walls and Pinning	24
2.3 Anisotropy	27
2.3.1 Magnetocrystalline Anisotropy	27
2.3.2 Shape Anisotropy	28
2.4 Single Domain Particles	29
2.4.1 Definition of Single Domain Particles	29
2.4.2 Stoner-Wohlfarth Model	30
2.4.3 Remanence of Single Domain Particles	37
2.4.4 Switching Field Distribution	40
2.5 Intergranular Interactions	41
2.6 The ΔM Curve	41
2.7 Thermal Activation	43
2.8 The Fe/MgO system	45
2.9 Magnetoresistance	47
2.9.1 Electrical Resistance	47
2.9.2 Two current model of a ferromagnet	49
2.9.3 Ordinary Magnetoresistance	50
2.9.4 Anisotropic Magnetoresistance	51
2.9.5 Giant Magnetoresistance	51

2.9.6	Tunneling Magnetoresistance	53
2.9.7	Other Magnetoresistance Effects	56
3	Material Requirements for Spintronics	59
3.1	Magnetic Materials	59
3.2	Non-magnetic metals	60
3.3	Semiconductors	62
3.4	Insulators	64
4	Thin Film Growth	67
4.1	Vapour Deposition	67
4.2	Epitaxial MBE Growth	69
4.3	Growth by Sputtering	71
4.4	Samples Studied of this Work	72
4.5	Annealing	74
5	Measurement Systems	77
5.1	Vibrating Sample Magnetometer	77
5.2	Alternating Gradient Force Magnetometer	79
5.3	Magnetoresistance Studies	81
5.4	Area measurement using optical Microscope	89
5.5	Measurement of the Saturation Magnetisation	89
6	Experimental Results	91
6.1	Magnetization Processes	91
6.1.1	Properties of the As-deposited Films	91
6.1.2	Effects of Annealing in Zero Field	93
6.1.3	Effects of Field Annealing	94
6.1.4	Remanence Curves	97
6.1.5	ΔM Curves	101
6.2	Magnetoresistance Studies	106
6.2.1	MR at high fields	107
6.2.2	MR at low fields	109
7	Conclusions and Further Work	119
7.1	Conclusions	119

7.2 Further Work	120
Appendix	123
Glossary	127
List of Symbols	127
List of Abbreviations	130
Bibliography	133

This work uses the cgs unit system because the majority of scientists in the field of magnetic materials and in the magnetic recording industry are still using this system.

List of Figures

2.1	Schematic drawing of the (a) Bloch and (b) Néel type domain walls [2] . . .	25
2.2	Magnetization curves of single crystal iron for different directions [3]. . .	28
2.3	Shape anisotropy vs axial ratio of a prolate ellipsoid. Numerically calculated for Fe.	29
2.4	Schematic of a single domain particle with easy axis, magnetic moment, external magnetic field and the angles γ, θ and ϕ	31
2.5	Solutions $H(\theta)$ of equation 2.13 for a single domain particle with easy axis perpendicular to the magnetic field H . Solid line represents stable solutions, dotted line unstable solutions.	32
2.6	Solutions $H(\theta)$ of equation 2.16 for a single domain particle with easy axis parallel to the magnetic field H . Solid line represents stable solutions, dashed line meta-stable solutions and dotted line unstable solutions. . . .	34
2.7	M-H curves of a single domain particle with uniaxial anisotropy and different angles γ between magnetic field and anisotropy axis. [3]	35
2.8	Dependence of coercivity (red) and critical switching field (blue) on the angle between magnetic field and anisotropy axis.	36
2.9	Hysteresis loop of an assembly of non-interacting, randomly orientated, uniaxial single domain particles . [3]	36
2.10	Magnetisation measurement and resulting IRM and DCD curves.	38
2.11	Graphical explanation of the parameter S^*H_c on the M-H curve of the as deposited Fe:MgO=3:1 sample in hard axis direction.	40
2.12	Model of the structure of the MgO/Fe(001) interface [4].	46
2.13	Schematic density of states of Fe.	49
2.14	(a) Parallel and (b) anti-parallel configuration for two current model of the GMR effect.	52
2.15	Anti-parallel (a) and parallel (b) configuration of CPP TMR setup.	53
3.1	Schematic density of states (DOS) of Cr, Fe, Co and Cu [5].	61

4.1	Cross sectional view of a planar magnetron sputter source [6].	72
4.2	Eiko HDH-10000 Ultrahigh Vacuum (UHV) Molecular Beam Epitaxy (MBE) System [7]	73
5.1	VSM coil arrangement according to Mallinson [8]	77
5.2	Princeton Measurement Micromag 2900 AGFM.	79
5.3	Purpose-built MR prober.	81
5.4	Block diagram of calibration setup.	82
5.5	Most precise Gaussmeter Calibration measurement with a ramp rate of 0.3 G/s. (a) Measured Voltage of the Gaussmeter vs. Measured field with the F.W.Bell Series 9900 Gaussmeter and third degree polynomial fit. (b) Deviation from linearity. This means the y-Axis shows the measured value of the F.W.Bell Series 9900 Gaussmeter minus value predicted by a linear fit.(c) Deviation from third degree polynomial fit.	83
5.6	Offset due to slower integration times of F.W.Bell Series 9900 Gaussmeter compared with the P.S.U. Magnetometer.	83
5.7	DC-MR setup.	84
5.8	An MR measurement at highest resolution.	86
5.9	AC-MR setup.	87
5.10	m-H curve measured using VSM with and without slope correction.	90
6.1	As deposited samples of different compositions with easy and hard axis.	92
6.2	(a) DCD+IRM and (b) Irreversible susceptibility curves of the easy axis of the Fe:MgO=1:1 sample after 1h annealing in zero field.	99
6.3	ΔM curve of the easy axis of the Fe:MgO=1:1 sample after 1h annealing in zero field.	102
6.4	ΔM curve of the easy axis of the Fe:MgO=1:1 sample after 3h annealing in ≈ 70 Oe field.	103
6.5	ΔM curve of the easy axis of the Fe:MgO=2:1 sample after 5h annealing in ≈ 70 Oe field.	104
6.6	ΔM curve of the easy axis of the Fe:MgO=4:1 sample after 6h annealing in ≈ 70 Oe field.	104
6.7	ΔM curve of the easy axis of the Fe:MgO=3:1 sample after 3h annealing in ≈ 70 Oe field.	105
6.8	Schematic of the 4 different MR measurement geometries used.	107

6.9	MR curve of Fe : MgO = 2:1 in easy axis direction with current parallel to the magnetic field. left: As deposited sample. right: Sample after 4h annealing in ≈ 70 Oe field.	110
6.10	Schematic of the sample with easy axes and crystalline directions.	111
6.11	Magnetoresistance curve for the Fe:MgO=1:1 sample after 2h annealing in 70 Oe field.	111
6.12	Superimposed magnetoresistance (red and blue) and M-H (black) curve for the Fe:MgO=1:1 sample after 2h annealing in 70 Oe field.	113
6.13	MR curves of the 4h annealed samples consisting of Fe:MgO = 4:1. The directions of the current and magnetic field applications are indicated in the figures. The magnetic field is parallel to the current and parallel to the easy axis (a) and hard axis (b). The blue line denotes signals obtained under a decreasing magnetic field from the maximum positive field to the maximum negative field while the red line denotes those under an increasing magnetic field. [9]	114
6.14	MR curves of the 5h annealed sample consisting of Fe:MgO = 4:1. The magnetic field is applied in the hard axis of the sample, while the current is applied parallel and perpendicular to the magnetic field for the top and bottom curves, respectively. [9]	115
6.15	Magnetoresistance curve of Fe:MgO sample after 4h annealing in ≈ 70 Oe field. The directions of current and field are indicated in the inlay drawing.	116
1	SpinFET experiment of Koo <i>et al.</i> [10] . (A) setup with magnetization of terminals in y direction. (B) SpinFET setup. (C) SEM of setup, before construction of gate. (D) Signal dependence on gate voltage for different experiments. Plots of different experiments are shifted for clarity. (E) Spin valve MR measurement.	124
2	Nonvolatile Multiple-Valued Memory.	126

List of Tables

3.1	Structures and lattice constants for some important spintronic materials. . .	63
4.1	Coevaporation parameters for Fe:MgO sample preparations.	74
6.1	Parameters of magnetization curves for as-deposited samples.	92
6.2	Fe:MgO=1:1 sample after different annealing times in zero field.	94
6.3	Fe:MgO=1:1 sample after different annealing times in ≈ 70 Oe field. . . .	94
6.4	Fe:MgO=2:1 sample after different annealing times in ≈ 70 Oe field. . . .	95
6.5	Fe:MgO=3:1 sample after different annealing times in ≈ 70 Oe field. . . .	96
6.6	Fe:MgO=4:1 sample after different annealing times in ≈ 70 Oe field. . . .	97
6.7	DCD and IRM parameters after annealing (e.a.).	98

Acknowledgements

I would firstly like to gratefully acknowledge my supervisor Kevin O'Grady. I thank Luke Fleet, James Sagar, Nick Cramp, Robert Carpenter, Ian Wright and Gonzalo Vallejo Fernandez for giving me introductions into several machines I used. I thank for the help and support of the Nanocenter and its staff and users with TEM sample preparation and TEM, SEM, EDX and AFM measurements. I thank the technicians for maintaining machines in Electronics and Physics in particular Bob Hide, Jonathan Cremer and Dave Coulthard. I thank Camilla Danese the Postgraduate Admissions Coordinator.

I acknowledge that the idea to research samples with coevaporated Fe and MgO is from Atsufumi Hirohata. I carried on with this project which was started by visiting students Hong Hing and Xinyang Zhang from Department of Electronic Engineering of the City University of Hong Kong. They did the sample preparation together and under the supervision of Luke Fleet for the samples with Fe:MgO = 4:1, 3:1 and 2:1. They also started MR measurements with the not yet improved MR setup, therefore just noise was measured. James Sagar, Andrew Vick and Yu Zhang did the sample preparation of the Fe:MgO = 1:1 samples. Yu Zhang was also a visiting student from Department of Electronic Engineering of the City University of Hong Kong and he carried out some of the MR and AGFM measurement of these samples under my supervision. I am grateful for his contribution to this research.

The thesis of Lewis [11] was of great help to understand and write about AGFM.

Last but not least I want to thank my wife Xiao for her constant support and understanding, especially when I was working overnight at university.

Declaration

Some of the research presented in this thesis has resulted in some publications. These publications are listed in section 1.3 on page 21.

I declare that the work presented in this thesis is based purely on my own research, unless stated otherwise. References and acknowledgements to other researchers have been given as appropriate. This work has not been submitted for a degree in either this or any other university.

Signed

Magnus Siegfried Rummey

September 2013

Chapter 1

Introduction

1.1 Overview

Since the discovery of the giant magnetoresistance (GMR) effect in 1988 [12, 13] and the development of a read head for hard disc drives based on that effect, spintronics seems to be developing as a promising technology for other applications. In 1990 Datta and Das proposed an electronic analog of the electro-optic modulator [14] better known as a Spin Field Effect Transistor (FET). In this Spin FET spin polarized electrons are injected into a two dimensional electron gas. The electrons then travel from the injector to the detector. In the context of transistors the injector and detector are called a source and drain respectively. Between the injector and detector the spin of the electron can be switched by the electric field of a gate electrode. If the spin direction were altered then an electron is less likely to enter the drain. The result is a spin current which can be switched. This was experimentally demonstrated by Koo *et al.* [10]

In 1996 a new mechanism was proposed for exciting the magnetic state of a ferromagnet [15, 16] this mechanism is known as Spin Transfer Torque (STT) which is used for switching Magnetoresistive Random Access Memory (MRAM), commercially available since November 2012 [17].

1.2 Applications

Magnetoresistive materials and structures are used as sensors for magnetic fields. These are used in magnetic recording, MRAM, motion sensors or just simply to measure the strength of a magnetic field. The properties of a magnetoresistive material determine in which range of magnetic fields it can be used. The resistance determines how fast the sensor can measure. Low resistance magnetoresistive materials will be applied in MRAM.

Due to the large change of resistance, GMR and tunnelling magnetoresistance (TMR) are of great interest as magnetoresistive materials. One possibility for realizing a TMR or GMR effect is to use grains of a magnetic material in a non-magnetic matrix [18]. The resistance depends on the relative orientation of the magnetic grains which results in spin dependent electron transport. An external field can force the magnetic moments of the grains to align parallel and that reduces the resistance of such a material. The magnetic grains are typically well separated and interact with each other only via dipole-dipole effects [5]. Their size is typically a few nanometres. Generally the grains are super-paramagnetic and without a magnetic field thermal energy randomizes their orientations. Depending on the size of the grains large fields of typically more than 10kOe are needed to align the grains.

Metal-insulator nano-granular magnetic thin films are of great interest: Depending on the ferromagnetic concentration of these films they exhibit granular TMR or may be of interest as possible new soft magnetic materials. The metal-rich ferromagnetic insulating nano-granular film are interesting for high-frequency applications such as thin-film inductors or noise suppressors [19]. The large ultrahigh frequency magnetic permeability is attributed to a combination of large electrical resistance and large induced magnetic anisotropy [20]. The insulator-rich insulating nano-granular films can exhibit tunnel-type magnetoresistance which originates from spin dependent tunnelling.

The insulators researched so far include MgF_2 , AlF_3 and amorphous Al-oxides and the magnetic grains used are Co or Co-Fe alloys [20]. Fujimori *et al.* [20] speculate that the crystalline structure of MgF_2 and AlF_3 is responsible for the larger resistivity and TMR values compared with films using amorphous Al-oxides as the insulator. Since spin valves with MgO as the insulator have shown very large TMR values [21] it is an

interesting material to study for granular TMR. In particular the combination of Fe with MgO which can be grown epitaxially, means that a potential system exists.

Problematic for granular TMR devices is the low field sensitivity, since high fields are needed to align the small grains. One solution to this problem was found by Kobayashi *et al.* [22], who deposited a nano-granular film into a small gap between two soft magnetic films. Very small fields of 1 Oe or less caused a resistance change of a few percent. Another possibility to increase the field sensitivity is by alignment of the anisotropy axes [23] e.g. through field annealing. A third approach might be the use of larger grains which align more readily in lower fields.

The aim of this work was to measure magnetoresistance and magnetization curves of a set of given Fe:MgO samples of the nominal volume ratios Fe:MgO = 1:1, 2:1, 3:1 and 4:1. The samples were as deposited or annealed at 400 ° C for up to 6h. Furthermore this work aimed at interpreting the magnetoresistance effects found in the samples and drawing conclusions about the magnetisation reversal mechanisms and the interactions in the samples.

1.3 Presentations and Publications

- A poster with the title 'Nanofabrication Process Optimisation Using Negative PMMA Resist' at the JSPS York-Tohoku Research Symposium on 'Magnetic Materials and Spintronics' at The University of York on 27th of June 2011 and at the Current Research in Magnetism (CRIM 2011) event on 21st of September 2011 at the Durham University.
- A poster was presented at the INTERMAG conference in Vancouver in May 2012 and at the Condensed Matter Physics (CMP) Workshop at the 2nd of July 2012 in York and it resulted in the publication: 'Magnetic properties of epitaxial co-evaporated Fe:MgO anti-granular films' [9]

Chapter 2

Magnetism and Magnetoresistance

2.1 Magnetism of Thin Films

There are two major types of magnetic thin films: Single crystalline and polycrystalline. For single crystalline films the magnetisation reversal is driven by domain wall motion. In polycrystalline films the magnetisation reversal depends on the coupling mechanism between the grains which are described in section 2.5. Intergranular exchange coupling promotes the alignment of the magnetisation of the grains in the same direction. This results in a domain wall driven reversal process. The domain walls can be pinned at defects like grain boundaries and inclusions, which results in a higher coercivity compared to single crystalline films. For magnetic grains which are not coupled by intergranular exchange coupling the dipolar interaction dominates the magnetisation reversal process. The samples studied in this work are polycrystalline and the reversal of the magnetisation is dominated by dipolar interactions for the Fe:MgO=1:1 samples, while samples with higher Fe ratio show intergranular exchange coupling.

A region which is uniformly magnetized is called a domain and their borders are domain walls. Domain walls can be moved due to a field H . The force per unit area, or pressure, the field causes at the domain wall is proportional to the field H and depends on the angle of the magnetization of the adjacent domains. For a 180° wall the pressure is $2HM_s$ [3]. Considering a simple one dimensional model of a domain wall, the energy

of the wall depends on the position due to microstress or inclusions and is a continuous function of the position with local minima. The slope of this function is the force on the domain wall to return to the local minima. It is also the force needed to push the domain wall to this position. The force in this simple model is proportional to H and goes with the pressure. Starting from a local minimum and applying an increasing field, the domain wall will move until the force to drive it back to the minimum is equal to the force caused by the field. Assuming that the rate of change of the field is slow, as long as the slope is increasing the wall will move. If a point is reached where the slope then starts to decrease, the inflexion point, then the wall will find the next equilibrium point. The wall moves to this point as quickly as possible. This quick movement of the domain wall is the reason for Barkhausen jumps (see p. 26). It is not an instant movement as the word jump would suggest, but the wall has inertia. To describe the motion of the wall accurately the wall will be treated similar to a car driving up and down hills: We have a driving force, the motor (field), we have a force due to the gravity, we have an effective mass to describe the inert property and we have a drag (viscous damping parameter β) proportional to the velocity of the car (wall). This model is limited to slow moving domain walls and it results in analogous equations of the motion. If the field is high enough the domain wall motion can be modelled as a movement with constant speed v . The speed is proportional to a mobility constant C_{mobil} [3]. :

$$v = C_{mobil}(H - H_0) \quad (2.1)$$

H_0 is a constant for the field which needs to be overcome to have a constant movement of the domain wall. H_0 is approximately equal to the coercivity. C_{mobil} in the case of a 180° wall is [3].:

$$C_{mobil} = \frac{2M_s}{\beta} \quad (2.2)$$

2.2 Domain Walls and Pinning

Between two domains the magnetisation rotates gradually and these regions are called domain walls. The length over which this change occurs is the domain wall width. If the thickness of the film is comparable to the width of the domain wall the film is considered a thin film in the context of magnetism [2]. These films are typically $\lesssim 100\text{nm}$ thick. There

are two main types of domain walls: Bloch and Néel domain walls. In Bloch walls the magnetisation rotates parallel to the domain wall. Therefore there is no magnetic charge within the wall and that minimizes the stray field energy. In a thin film the wall ends at the surfaces of the film and the demagnetizing energy of the wall depends on the thickness of the domain wall as well as the thickness of the film. If the thickness of the domain wall is larger than the thickness of the film the wall prefers the Néel wall mode [2]. In a Néel wall the rotation of the magnetisation includes the normal vector of the domain wall. Schematics of both walls are shown in figure 2.1.

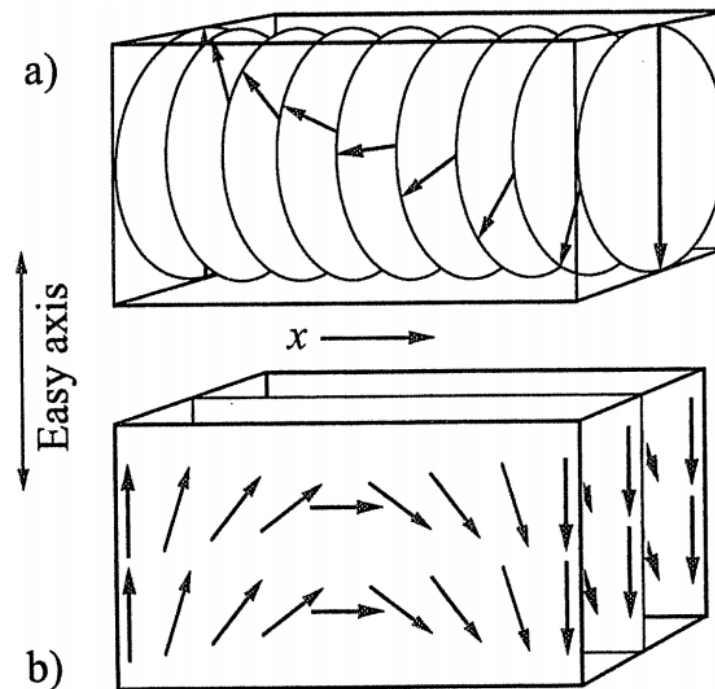


Figure 2.1: Schematic drawing of the (a) Bloch and (b) Néel type domain walls [2]

Domains prefer to align along defects within the material, especially along grain boundaries and inclusions. Inclusions are often nonmagnetic particles within a magnetic material. A domain wall which includes an inclusion benefits in 2 ways from that inclusion: 1. The area in the domain wall which is occupied by the inclusion reduces the energy for the domain wall in this area. 2. The inclusion within a domain possesses a dipolar like magnetic charge opposing the magnetic field of the domain. An inclusion at the domain wall possesses a dipolar like magnetic charge at each side of the wall resulting in approximately half of the magnetostatic energy of the inclusion outside of the barrier. Usually the second contribution is much higher and the ratio of the second contribution to the first rises with the size of the inclusion. An example calculation is found in Cullity and Gra-

ham [3] who calculate that this ratio is 140:1 for a spherical inclusion of $1\mu\text{m}$ diameter in iron. In this simple model a 7nm diameter inclusion would then have approximately the same contribution from both effects. Such inclusions are then smaller than the thickness of domain walls, so it reduces the energy of the domain wall, but contributes almost nothing to the magnetostatic energy. Inclusions of the size of a domain wall are the most efficient anchors for the domain wall per unit volume of inclusion [3]. Wade measured a 120° domain wall thickness of a 17nm thick randomly oriented polycrystalline Fe to be $(100 \pm 40)\text{nm}$ [24].

A domain wall can be moved by an external magnetic field. Inclusions and other defects in the material hinder the movement of domains. This effect is called domain wall pinning. An external magnetic field trying to move a domain wall can do this easily in regions without pinning sites. If a critical field is overcome the domain wall suddenly snaps free of a pinning site. This causes a sudden jump in the magnetisation known as a Barkhausen jump.

A sample in a high magnetic field is fully saturated and has no domain walls. Reducing the magnetic field and reversing the field direction leads to the formation (nucleation) of a domain wall at the nucleation field H_n . The nucleation field varies in the presence of strong exchange interactions and increases at lower temperatures. At higher temperatures the nucleation of domain walls can initiate before the field direction is reversed due to thermal activation.

The thickness of Fe films researched by Wade [24] is similar to the thicknesses of the samples studied in this work which were in the range 20 to 30nm. The inclusions in the samples studied were of the order of a few nanometers, typically below 10nm. Therefore it can be assumed that the inclusions were smaller than the thickness of a domain wall. The mean inter-particle distance for all samples investigated is always $\lesssim 12\text{nm}$ [25], which means that within a domain wall there are typically a few inclusions within the domain wall width. While the domain wall is moving through the film, for every inclusion which leaves the domain wall on one side, the wall finds another inclusion on the other side, reducing the inclusions to bulk like features. The strongest contribution to pinning is therefore expected from the larger particles at the tail of the distribution with stronger pinning strength due to their larger size.

2.3 Anisotropy

Anisotropy in magnetism means that the energy of a magnetic moment in a material depends on its direction e.g. relative to the shape and crystalline axes of the material. The directions with the lowest (highest) energy are called easy (hard) axes and the moments align spontaneous in the easy directions. The uniaxial anisotropy is defined via an anisotropy energy density K . This quantity gives rise to the anisotropy field in the Stoner-Wohlfarth model introduced in equation 2.14. The anisotropy can be measured by different methods e.g. by measuring the magnetization (M-H) curves. The magnetization work per unit volume of an infinitesimal part of the curve can be calculated from:

$$dW = HdM \quad (2.3)$$

The work for a closed cycle of an M-H curve is therefore equal to the area enclosed by the hysteresis. This work is called hysteresis loss. The different losses in different directions are due to different anisotropy energies.

2.3.1 Magnetocrystalline Anisotropy

Most magnetic materials are crystalline. It is reasonable to expect the symmetry to be reflected in the magnetocrystalline anisotropy of the material. Iron under standard conditions has a body-centered cubic (bcc) structure and so has 3 anisotropy axes. Figure 2.2 shows the magnetization curves of single crystal iron for different directions. The $\langle 100 \rangle$ directions i.e. $[001]$, $[010]$ and $[100]$ are the 3 easy axes, the $\langle 111 \rangle$ directions i.e. $[111]$, $[-111]$, $[1-11]$ and $[11-1]$ are the hard axes. Directions like $\langle 110 \rangle$ are in between easy and hard axis and might be called medium axes (or medium hard axis).

Iron films of 1.5nm to 80nm thickness grown on MgO using an MBE system show uniaxial crystalline anisotropy with anisotropy field of approximately 20 Oe induced by the angle of incidence of the Fe atoms during growth [26].

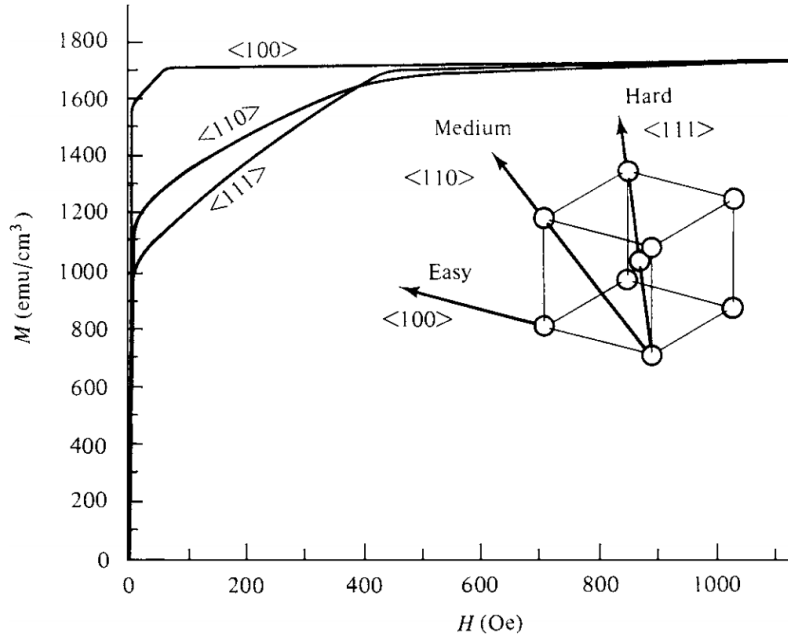


Figure 2.2: Magnetization curves of single crystal iron for different directions [3].

2.3.2 Shape Anisotropy

The shape of a magnetic particle and its magnetisation give rise to a demagnetizing field. To minimize the free-energy the direction of the magnetic moment of the particle is moved to a direction where the demagnetizing field is minimized. The demagnetizing field is proportional to a demagnetizing factor or demagnetizing coefficient N_d . Assuming the shape of the particle is a prolate ellipsoid, the demagnetizing factors for the long semi-axis c and the short semi-axes a and b ($a=b$) can be calculated from the axial ratio $g = c/a$ [3]:

$$N_c = \frac{4\pi}{g^2 - 1} \left(\frac{g}{\sqrt{g^2 - 1}} \ln(g + \sqrt{g^2 - 1}) - 1 \right) \quad (2.4)$$

$$N_a = N_b = \frac{4\pi - N_c}{2} \quad (2.5)$$

with N_a, N_b and N_c the demagnetizing factors along the a , b and c semi-axis of the ellipsoid. The shape anisotropy K_s of such a particle can be expressed using the demagnetizing factors and the magnetization as [3]:

$$K_s = \frac{1}{2} (N_a - N_c) M_s^2 \quad (2.6)$$

The magnetocrystalline anisotropy K_C of cubic materials is small due to the symmetry. For Iron $K_1 = 4.8 \times 10^5 \frac{\text{ergs}}{\text{cm}^3}$. Due to the high value of magnetization ($M_s = 1714 \frac{\text{emu}}{\text{cm}^3}$)

shape anisotropy dominates for small deviations from a perfect sphere shape. Figure 2.3 shows the numerical calculation of the shape anisotropy depending on the axial ratio g .

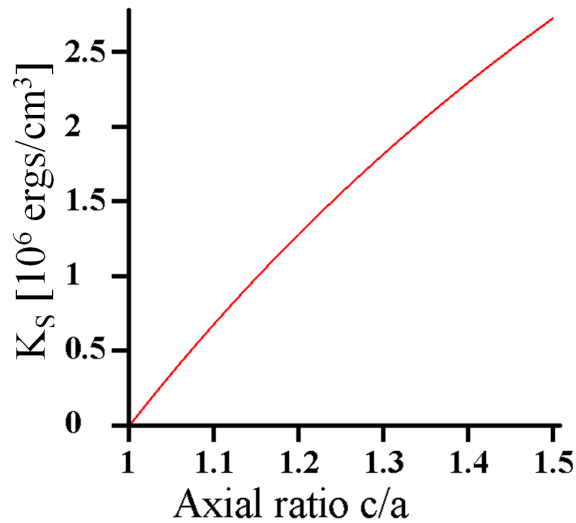


Figure 2.3: Shape anisotropy vs axial ratio of a prolate ellipsoid. Numerically calculated for Fe.

It can then be calculated that the shape anisotropy is dominant for an axial ratio $g > 1.065$. This means that for Fe particles with small deviations from a sphere the uniaxial shape anisotropy will dominate over the magnetocrystalline anisotropy. All real iron particles have this degree of elongation leading to real systems having uniaxial anisotropy. These deviations are also too small to be resolved by TEM analysis. Typical measured values for K for quasi spherical particles of cubic materials is of the order of $2 \times 10^6 \frac{ergs}{cm^3}$ [27].

2.4 Single Domain Particles

2.4.1 Definition of Single Domain Particles

Particles are called single domain particles (SDP) if the atomic magnetic moments within the particle are always parallel, independent of external magnetic fields. They therefore always consist of one single domain and are too small to support a domain wall inside them. Brown [28] calculated upper and lower bounds for a critical radius for a spherical particle with uniaxial anisotropy. Below the lower bound radius the particle has the lowest-

free-energy state as a SDP, however the lowest-free-energy state may not be reached [29]. Calculating for the parameters of Fe $M_s = 1700 \frac{emu}{cm^3}$, exchange constant $C^* = 2 \cdot 10^{-6} \frac{ergs}{cm}$ and the first-order magnetocrystalline anisotropy constant $K_1 = 4.5 \cdot 10^5 \frac{ergs}{cm^3}$ Aharoni calculates a critical radius between 8.46 nm and 11.0 nm using Brown's formulae [29]. His numerical computations also suggest that the real critical radius is closer to the lower bound. Recently Brown's model was generalized for ellipsoids [30]. Even if not all magnetic moments are parallel for all external fields, a description as a single-domain particle might still be a good approximation and therefore models assuming single-domain particles, like the Stoner-Wohlfarth model are still appropriate.

2.4.2 Stoner-Wohlfarth Model

The magnetic hysteresis of SDPs and of materials consisting of SDPs was calculated by Stoner and Wohlfarth [31]. The change of magnetization in SDPs can take place only by rotation of the magnetization vector. Since only the direction of this vector changes, the dynamics of the SDP can be expressed by just the 2 angles of the vector. An external magnetic field exerts a torque $\vec{\tau}_{dp}$ on a magnetic moment pulling the magnetisation in the direction of the field. The magnetocrystalline and/or shape anisotropy of the particle exerts a torque $\vec{\tau}_{an}$ pulling the magnetisation towards an easy axis. The magnetisation will then find a stable or meta-stable position where the torques nullify each other. These positions of equilibrium may be found by using the equation for the energy depending on both angles and finding all local minima by setting the gradient = 0 and calculating for the solutions the second partial derivative test. In the simplest case we assume uniaxial anisotropy and have easy axis, magnetisation vector and external magnetic field in the same plane, leaving just one angle to describe the state of the SDP. The energy E_{an} representing the anisotropy K can be expressed by the angle θ between magnetization and easy axis:

$$E_{an} = KV \sin^2(\theta) \quad (2.7)$$

V is the volume of the particle. The torque τ_{an} is then calculated as [32]:

$$\tau_{an} = -\frac{\partial E_{an}}{\partial \theta} = -2KV \sin(\theta) \cos(\theta) \quad (2.8)$$

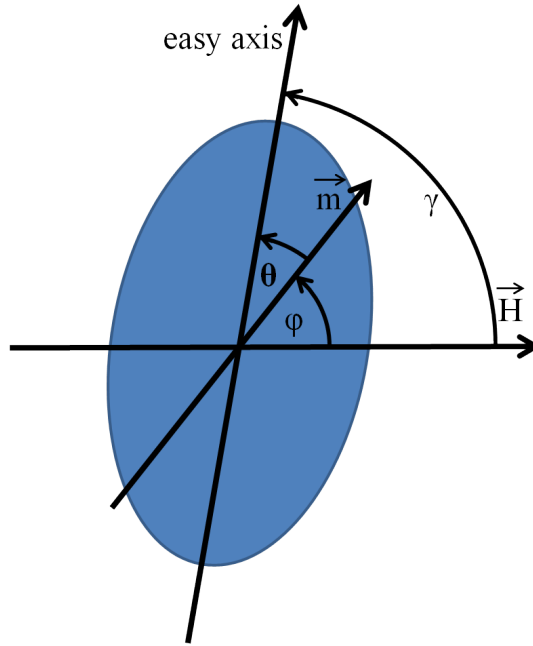


Figure 2.4: Schematic of a single domain particle with easy axis, magnetic moment, external magnetic field and the angles γ, θ and ϕ .

The torque τ_{dp} on the magnetic moment \vec{m} due to the angle ϕ between magnetic moment and external field \vec{B} is:

$$\tau_{dp} = \|\vec{\tau}_{dp}\| = \|\vec{m} \times \vec{H}\| = mH \sin(\phi) \quad (2.9)$$

The SDP is in a state of equilibrium if the sum of the torques equals zero:

$$0 = \tau_{dp} + \tau_{an} = mH \sin(\phi) - 2KV \sin(\theta) \cos(\theta) \quad (2.10)$$

We define now an angle γ of the magnetic field to the easy axis as shown in figure 2.4 to replace $\phi = \gamma - \theta$ and get:

$$0 = \tau_{dp} + \tau_{an} = mH \sin(\gamma - \theta) - 2KV \sin(\theta) \cos(\theta) \quad (2.11)$$

Assuming an external field perpendicular to the easy axis ($\gamma = 90^\circ$) then the equation is:

$$0 = \tau_{dp} + \tau_{an} = mH \sin(90^\circ - \theta) - 2KV \sin(\theta) \cos(\theta) \quad (2.12)$$

And it follows:

$$0 = \cos(\theta)(mH - 2KV \sin(\theta)) \quad (2.13)$$

This equation has 4 solutions which will be called P1, P2, P3 and P4. The dependences

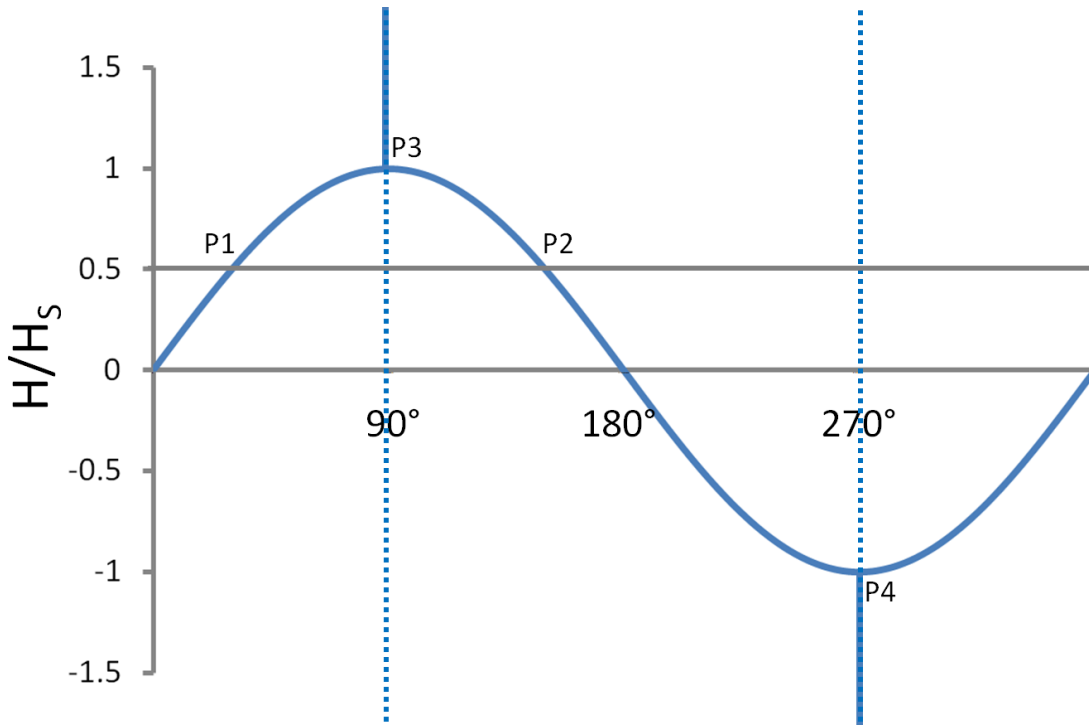


Figure 2.5: Solutions $H(\theta)$ of equation 2.13 for a single domain particle with easy axis perpendicular to the magnetic field H . Solid line represents stable solutions, dotted line unstable solutions.

$H(\theta)$ of these solutions is shown in figure 2.5. The second factor becomes 0 if $\sin(\theta) = \frac{mH}{2KV} = \frac{M_s H}{2K}$. This condition has two solutions P1(H) and P2(H) if

$$-1 < \frac{M_s H}{2K} < 1 \implies -\frac{2K}{M_s} < H < \frac{2K}{M_s} \implies \|H\| < H_K \quad \text{with} \quad H_K = \frac{2K}{M_s} \quad (2.14)$$

with H_K the anisotropy field. The first point P1 is between 0° and 90° and the other is $P2 = 180^\circ - P1$. The first factor in equation 2.13 is $\cos(\theta)$ and is =0 if θ is 90° (solution P3) or 270° (solution P4). For $H = H_K$ ($H = -H_K$) there is just one point $P1=P2=90^\circ =P3$ ($P1=P2=270^\circ =P4$) making the second factor of the equation 2.13 zero and for $\|H\| > H_K$ the second factor term cannot = 0. This means for large fields $H > H_K$ there are just the 2 solutions to the equation 2.13. For $H < H_K$ ($H > -H_K$) P3 (P4) is an unstable point equilibrium since the contributions for both torques close to this point of equilibrium drive the magnetic moment away from this point. For $H > H_K$ ($H < -H_K$) P3 (P4) is a stable point equilibrium and there are magnetic moment and external field parallel. Starting from $H > H_K$ and decreasing the magnetic field, P3 will become unstable as soon as $H < H_K$ and the magnetic moment randomly decides to go to the point P1 or P2. With further decreasing magnetic field the magnetic moment moves with P1 (or P2) from 90° to 0° (or

180°). The measured magnetisation in the direction of the magnetic field is proportional to the projection of the magnetic moment on the axis of the magnetic field. This means that an M-H curve is a straight line between the critical field H_K where the curve reaches saturation and the point where no magnetic field is applied. In this process there are no jumps of magnetisation and it is completely reversible. Since the probability for the momentum of particle to follow the P1 solution is equal to the probability to follow the P2 solution, a material made of these particles is demagnetized when the field is turned off after saturation. However if the angle γ between easy axis and field slightly deviates from 90° then all moments will move with either P1 for $\gamma < 90^\circ$ or P2 $\gamma > 90^\circ$ and this results in all magnetic moments pointing parallel in the easy axis direction and the material is saturated instead of demagnetized. In reality the easy axes of the particles are often not perfectly parallel aligned and a finite temperature wiggles the magnetic moment making it possible for particles to have their moment move with P1 or with P2 when the field drops below H_K even if there is a slight deviation from $\gamma = 90^\circ$. This makes it possible to demagnetize samples by applying a field perpendicular to the easy axis. The thin films studied in this work had their easy axis in the plane of the thin film. A field normal to the film plane can demagnetize the sample, but the samples holders were not able to ensure an accurate enough alignment to reach complete demagnetization this way. An example of a sample demagnetized by this method can be found in Cullity and Graham [3].

If the magnetic field is applied along the easy axis ($\gamma = 0^\circ$) the equation 2.11 becomes:

$$0 = \tau_{dp} + \tau_{an} = mH \sin(-\theta) - 2KV \sin(\theta) \cos(\theta) \quad (2.15)$$

And it follows:

$$0 = -\sin(\theta)(mH + 2KV \cos(\theta)) \quad (2.16)$$

The 4 solutions to this equation differ just in position and stability from the solutions to equation 2.13. The dependences $H(\theta)$ of these solutions is shown in figure 2.6. The first factor of equation 2.16 is 0 if θ is 0° (solution P3) or 180° (solution P4). The second factor is 0 if $\cos(\theta) = -\frac{mH}{2K}$. This condition has two solutions P1(H) and P2(H) if $\|H\| < H_K$. Starting from $H = H_K$ the first point P1 moves for decreasing H from 180° to 90° for $H > 0$ and for increasing negative H from 90° to 0° . The other point P2 is $360^\circ - P1$. For $H = H_K$ ($H = -H_K$) there is just one point $P1=P2=180^\circ = P4$ ($P1=P2=0^\circ = P3$) making the second factor of the equation 2.16 zero and for $\|H\| > H_K$ the second

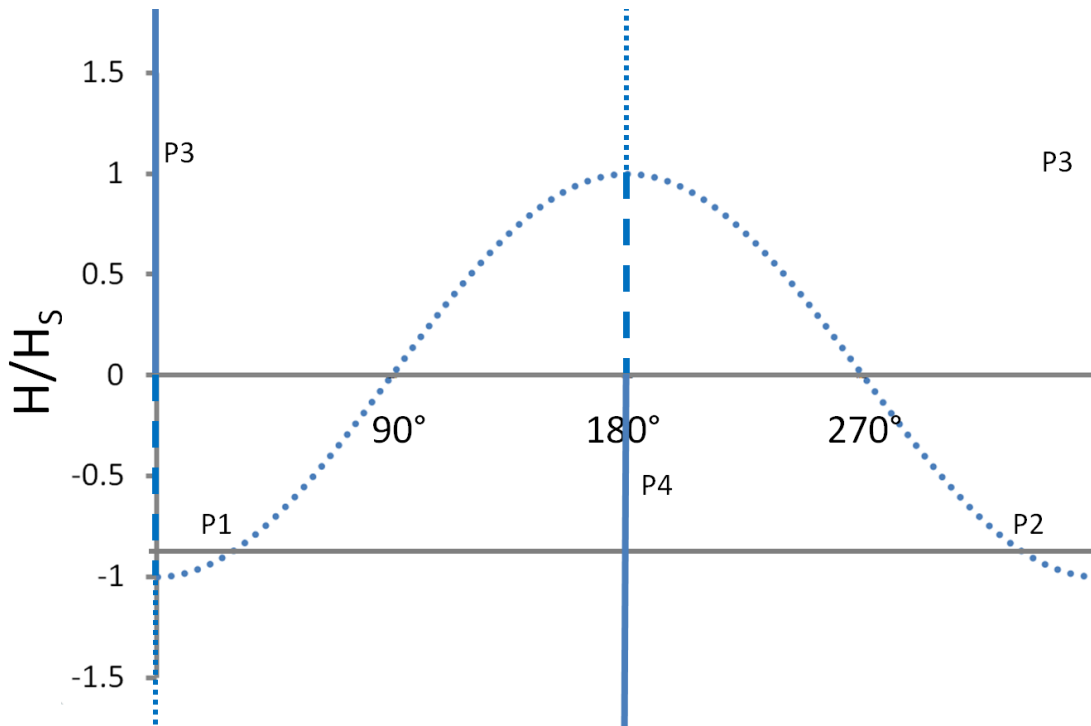


Figure 2.6: Solutions $H(\theta)$ of equation 2.16 for a single domain particle with easy axis parallel to the magnetic field H . Solid line represents stable solutions, dashed line meta-stable solutions and dotted line unstable solutions.

factor term cannot be 0. This means for large fields $\|H\| > H_K$ there are just 2 solutions to the equation 2.16. For $H > H_K$ the point P3 at 0° is the stable solution and P4 at 180° is unstable. The solutions P1 and P2 are unstable points of equilibrium. A small deviation from these points will move the system to states P3 or P4. Starting from a field $H > H_K$ and reducing the magnetic field, the point P3 will not become unstable at $H = H_K$ since both contributions to the torque for states near P3 drive the magnetic moment back to P3. When reversing the direction of the external magnetic field, the point P3 stays meta-stable as long as $\tau_{an} > \tau_{dp}$ since the sum of both torques still drives states near P3 back to P3. When H approaches $-H_K$ the points P1 and P2 approach P3. Shortly before reaching this field the thermal energy is enough to displace the magnetic moment randomly beyond P1 or P2 and then the state of the system switches irreversibly to P4. Neglecting the thermal energy the SDP switches exactly when $H = -H_K$. This results in a perfectly square and irreversible M-H-loop. For other angles of magnetic field to easy axis between these two extremes the reversal process is a mixture of reversal and irreversible processes and calculated M-H curves for some of these cases are shown in figure 2.7. The most significant difference between the cases just discussed and other

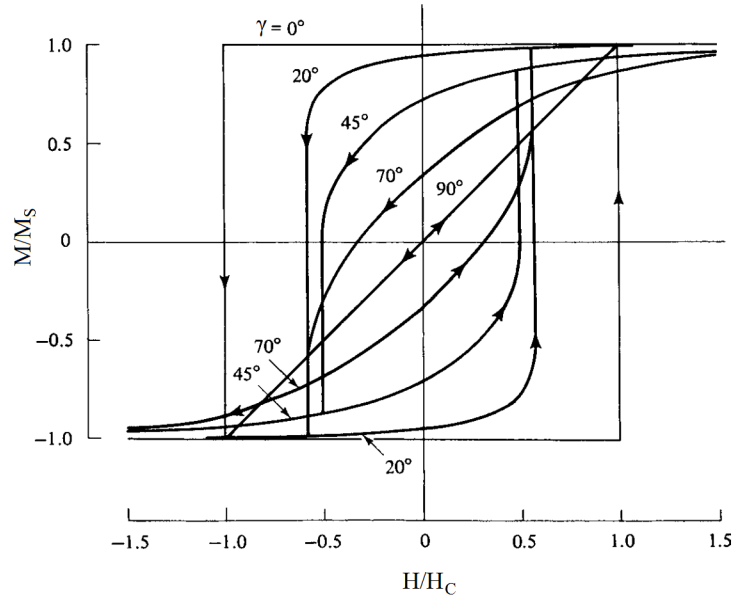


Figure 2.7: M-H curves of a single domain particle with uniaxial anisotropy and different angles γ between magnetic field and anisotropy axis. [3]

angles is that for a magnetization in direction of the external field, there is an anisotropy torque. Since the torque of the external field becomes zero for this direction, there is always an effective torque drawing the magnetic moment towards the nearest easy axis. With increasing external field the moment moves towards the direction of the external field. For decreasing fields the moment relaxes into the nearest easy axis. The remanence is the projection of the moment pointing along the easy axis onto the axis of the external field direction. The remanence magnetization M_R is therefore:

$$M_R = M_s \cos(\gamma) \quad (2.17)$$

For increasing negative H at first the magnetic moment is reversibly moved away from the easy axis until the angle θ between moment and easy axis reaches the critical angle θ_C [3]:

$$\tan^3(\theta_C) = -\tan(\gamma) \quad (2.18)$$

When the critical angle is reached, the moment moves to the next point of equilibrium. Figure 2.8 shows the angular dependence of the normalized coercivity as a red line and the normalized critical field for the irreversible switching process as a blue line. For γ smaller than 45° the jump changes the direction of the magnetization, so the coercivity H_C is equal to the critical field. For γ larger than 45° the magnetization direction changes within the reversible movement of the moment. Stoner and Wohlfarth [31] then calculated

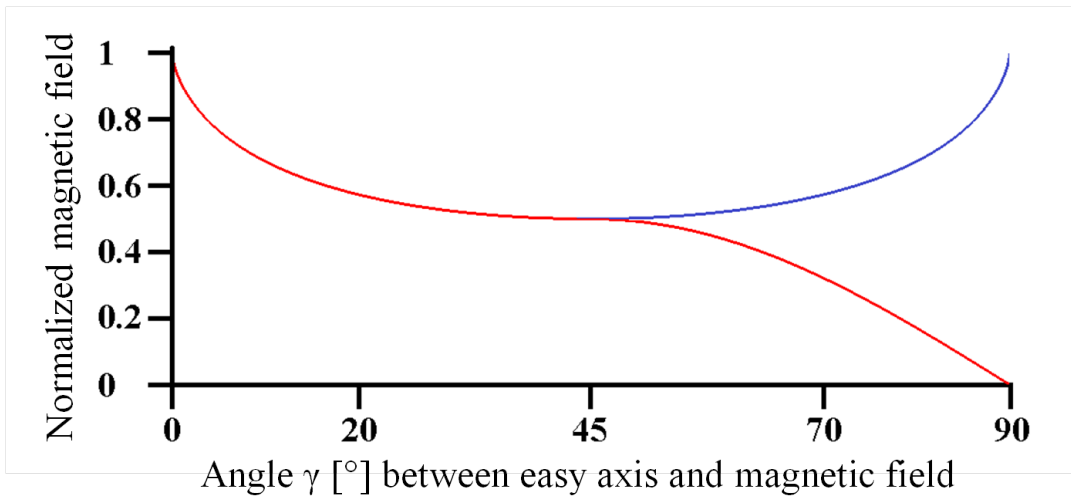


Figure 2.8: Dependence of coercivity (red) and critical switching field (blue) on the angle between magnetic field and anisotropy axis.

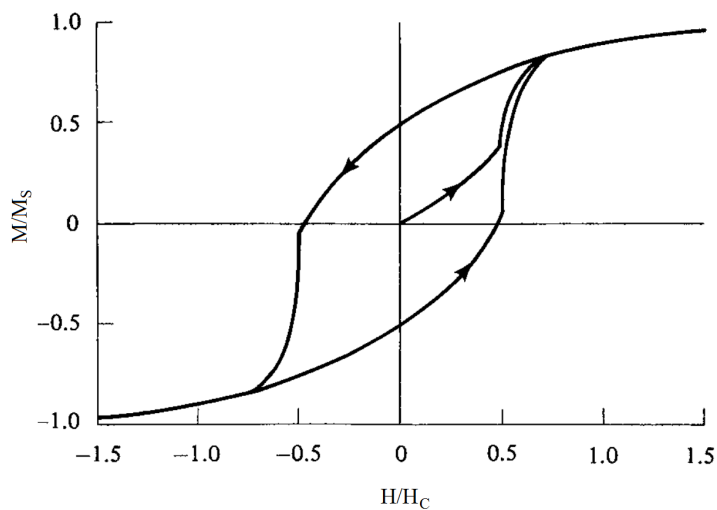


Figure 2.9: Hysteresis loop of an assembly of non-interacting, randomly orientated, uniaxial single domain particles . [3]

the hysteresis loop for a bulk material with non-interacting SDPs and randomly orientated easy axes as shown in figure 2.9. This loop was calculated as a three dimensional average of all possible different loops. The normalized remanence is 0.5 and the normalized coercivity is $0.479 H_K$. A remanence different from this indicates either that the grains are interacting or that the easy axes are not randomly orientated. Systematically analyzing the remanence of minor loops and measuring the deviations from the Stoner-Wohlfarth model then allows conclusions to be drawn about the interactions in the material [33].

2.4.3 Remanence of Single Domain Particles

Without an external field all moments of non-interacting SDPs point in their easy axis directions. The sum of their moments divided by the volume of the material is the remanent magnetization. Irreversible processes, as discussed in the previous section, are responsible for changes in the remanence. In a hysteresis loop of non-interacting SDPs with uniaxial easy axis parallel to the magnetic field, all processes are irreversible, therefore M-H measurements are remanence measurements. For uniaxial anisotropy there are two anti-parallel possibilities in which the moment can point. Applying an increasing field to this material, the magnetic moment does not change unless a particle reaches its critical switching field. Since the switching is irreversible it does not reverse when the field is switched off. Measuring the irreversible part of the magnetization is a remanence curve.

There are two principle remanence curves: The isothermal remanence magnetization (IRM) curve and the DC-demagnetisation curve (DCD).

To measure the IRM curve, the sample is demagnetized and then a small field is applied and the remanence measured, then step by step larger fields are applied and the remanence is measured. The diagram of remanence versus applied field is then the IRM curve. For a reproducible IRM measurement the sample needs to be demagnetized in a way where the IRM curve for positive field direction is identical to the IRM curve for negative field direction. This means that for each different H_K of particles in the material half of the magnetization has parallel and half anti-parallel alignment.

The DCD curve starts from the remanence magnetization after saturating the sam-

ple and then step by step an increasingly negative field is applied and the remanence is measured. For better reproducibility the sample should be positively saturated after each measurement of the remanence. Figure 2.10 shows the path of the magnetisation during an IRM and DCD measurement and the resulting IRM and DCD curve. The DCD curve is usually displayed for positive fields unlike the diagram in figure 2.10.

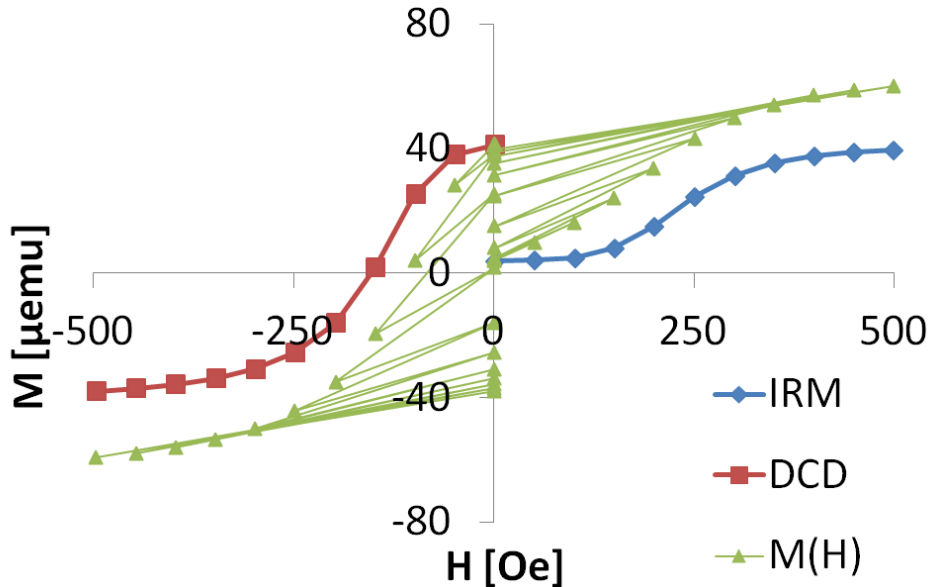


Figure 2.10: Magnetisation measurement and resulting IRM and DCD curves.

Assuming that the particles in a non-interacting SDP material with uniaxial anisotropy differ in shape or magnetocrystalline anisotropy, they have different values of H_K . This means that the remanence curves contain the information of the distribution of H_K . The differentiation of the remanence curves by the external field gives the irreversible susceptibility and that is a direct measure for the switching field distribution [33]. Assuming the material with parallel aligned easy axis, in an IRM curve for each different H_K of particles in the material half of the magnetization has parallel alignment before H_K is reached and all have parallel alignment after H_K is reached. For the DCD curve all particles have parallel alignment before $-H_K$ is reached and all have anti-parallel alignment after $-H_K$ is reached. This means that the magnetization change of the DCD curve at $-H_K$ is twice as large as the magnetization change for the IRM curve at H_K for each different H_K of particles. This argument can also be applied for all irreversible processes measured by the remanence measurements of all directions for non-interacting SDPs with aligned or

randomly orientated easy axis. These concepts give rise to the Wohlfarth relation [34]:

$$\overline{M}_d(H) = 1 - 2\overline{M}_r(H) \quad \text{with} \quad \overline{M}_{d,r}(H) = \frac{M_{d,r}(H)}{M_{d,r}(\infty)} \quad (2.19)$$

With M_d the remanent magnetisation of the DCD curve and M_r the remanent magnetization of the IRM curve and $M_{d,r}(\infty)$ the remanence magnetization after the material was fully saturated. However for the use of equation 2.19 it is critical that the IRM curve is measured from a correctly demagnetized state.

Achieving such a state requires careful experimental procedures. One way to demagnetize a sample is to heat it above the Currie temperature and then cool down in zero field. Any magnetic field e.g. the magnetic field of the earth can induce a magnetization during cooling. To prevent this the sample can be rotated in all directions and/or be in an alternating magnetic field whilst the sample is slowly cooled down. This method ensures a completely demagnetized state, but heating the sample can also cause re-crystallization and change the properties of the sample. Since the Currie temperature of Fe is above the annealing temperature of the samples studied, this method cannot be used. Another method of demagnetizing is called dc cyclic erasure [35]. The magnetic field is swept with decreasing amplitude. According to the Stoner-Wolfarth model each fraction of particles with a certain H_K has then either a positive or negative magnetization direction. In the switching field distribution the fractions with positive and negative directions alternate with the decrement of the alternating field. If the field decrement is much smaller than the switching field distribution and also smaller than the step size of the remanence measurement, then the sample appears to be sufficiently well demagnetized to perform an IRM measurement. However it is problematic to demagnetize samples with narrow switching field distributions or strong exchange coupling with this method [35]. Another way of demagnetizing a sample is by using an AC magnetic field. This is accomplished by pulling the sample out and away from a coil with AC current passing through it and/or reducing the AC current through the coil. There are also commercially available demagnetizers in the shape of a thick pen, which produce an AC magnetic field at the tip. The tip is put on the sample and then very slowly removed.

2.4.4 Switching Field Distribution

The irreversible susceptibility is a measure of the switching field distribution and is determined by differentiation of IRM or DCD curves. The switching field distribution can be characterized by the full width half maximum FWHM of the irreversible susceptibility curves once the area has been normalized to unity. Another interesting parameter is the remanent coercivity H_r , which is given by $DCD(H_r) = 0$. For the IRM curve a similar field H'_r can be defined as $IRM(H'_r) = 0.5$. At these fields half of the magnetic volume has switched irreversibly. Additionally fields where one quarter and three quarters of the volume have switched can be determined. The difference between these fields normalized by H_r gives a parameter Δh which is approximately equal to $1-S^*$ [36]:

$$S^* = 1 - \frac{M_r(\infty)}{H_c \frac{dM(H)}{dH} \Big|_{H=H_c}} \quad (2.20)$$

where S^* is the coercivity squareness and H_c the coercivity. The parameter S^*H_c is the field where a tangent at the coercivity reaches the remanent magnetization as shown in figure 2.11. If a material shows more than one peak in the irreversible susceptibility it may be possible to find a multi-peak model to give the FWHM for each peak. Otherwise these parameters are not appropriate to describe multi-modal magnetisation reversal.

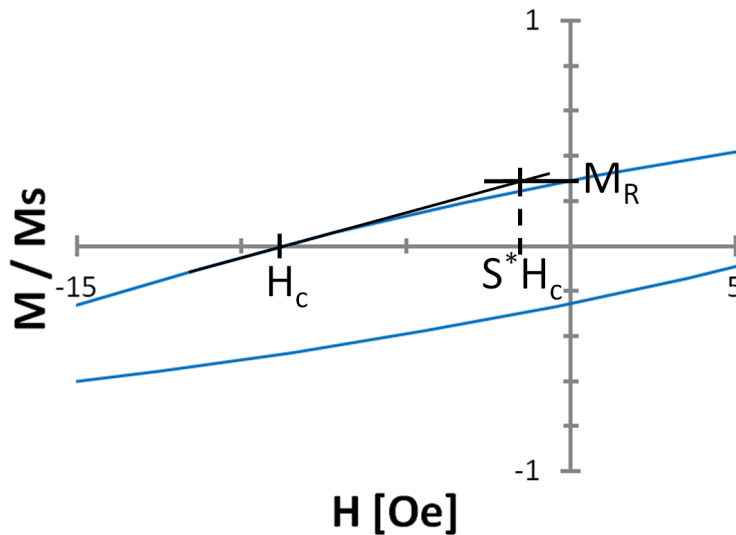


Figure 2.11: Graphical explanation of the parameter S^*H_c on the M-H curve of the as deposited Fe:MgO=3:1 sample in hard axis direction.

2.5 Intergranular Interactions

Intergranular exchange coupling is dominated to a first approximation by the nearest neighbours of a grain. Between two grains with indexes 1 and 2 the intergranular exchange coupling energy E_e can be described phenomenologically as [37]:

$$E_e = -J^* \vec{m}_1 \cdot \vec{m}_2 \quad (2.21)$$

For each grain the energy is summed over all nearest neighbours and then the total energy is the sum of the energies of all grains. The exchange integral J^* is modelled to be proportional to r_{cc}^{-2} with r_{cc} the centre-to-centre distance of the grains. It is described via an effective field \vec{H}_e often normalized to the anisotropy field:

$$\vec{h}_e = \vec{H}_e / H_K \quad (2.22)$$

The normalized intergranular exchange interaction field \vec{h}_e at a grain due to the moment \vec{m}_2 of a second grain is :

$$\vec{h}_e = 2J^* m_1 / H_K \vec{m}_2 = C^* \vec{m}_2 \quad (2.23)$$

With C^* is the intergranular exchange coupling constant.

The magnetostatic interaction energy has a component due to self-demagnetisation energy and due to dipole-dipole interactions between the grains. To calculate this energy for a grain an effective magnetic moment can be calculated representing the magnetic moments of all grains. This effective moment is a sum over all magnetic moments with a geometric correction factor for each moment. This correction factor depends on the shape and relative position of the grain. Usually just a few nearest neighbours are calculated and a mean field approximation is used. Another approach for simplifying a simulation is the use of periodic constraints. A detailed calculation can be found in Mee and Daniel [38].

2.6 The ΔM Curve

Equation 2.19 can be written as:

$$0 = \overline{M_d}(H) - (1 - 2\overline{M_r}(H)) = \overline{M_d}(H) + 2\overline{M_r}(H) - 1 \quad (2.24)$$

Interactions between grains will cause a deviation from this equation and this deviation is expressed as ΔM [39]:

$$\Delta M(H) = \overline{M}_d(H) + 2\overline{M}_r(H) - 1 \quad (2.25)$$

Positive values of ΔM indicate that $2 \times \text{IRM}$ is increasing faster than the DCD is decreasing and that means that the magnetized state of the material is energetically preferred. This means a positive coupling between the grains ergo intergranular exchange coupling. Negative values of ΔM indicate that the DCD is decreasing faster than $2 \times \text{IRM}$ is increasing and that means a demagnetized state is energetically preferred and that means that the dipolar interaction between the grains dominates the magnetization reversal. Samples may show positive and/or negative ΔM values during reversal. A ΔM curve always starts at 0 for $H=0$. A deviation from this indicates that the sample at the start of the IRM measurement was not fully demagnetized. When the sample saturates, the ΔM curve also returns to zero.

ΔM curves are very useful for analyzing strongly interacting systems like the materials used by the recording media industry [40]. It has been used to assess interactions between nanoparticles [41–45], nanowires [46], in nanostructured materials [40,47], nanocomposites [48] and thin films [33]. In these studies a negative ΔM values were usually observed when the magnetic nanoparticles or the magnetic cores of nanoparticles were separated. Positive ΔM values were observed, when the particles are in contact. This transition from negative to positive ΔM values through aggregation of nanoparticles by annealing is demonstrated in the work of Zeng *et al.* [42]. This can be explained by the short range of the intergranular exchange interaction compared to the longer range dipole-dipole interaction.

Mayo *et al.* [33] studied interactions in CoNiCr thin films on Cr underlayer as prepared by Yogi *et al.* [49]. For a 10nm Cr underlayer ΔM increased with the field to a value of more than 1.25, then plunged to a small negative value and then recovered to zero. Strong exchange interactions are responsible for this behaviour. The reversal was cooperative switching of the magnetic domains with a magnetic overshooting due to an avalanche-type effect within the bulk of the material. For increasing underlayer thickness the maximum ΔM value decreases and the peak broadens. This is attributed to a decrease in the interaction between the grains. For an underlayer thickness of 200nm the ΔM curve shows a negative interaction profile. CoNiCr grains grow on top of a Cr

grains and align on the granular texture of the underlayer. With increasing thickness of the Cr underlayer the CoNiCr grains separate from one another and with increasing distance the dipolar interaction becomes dominant. Numerical simulations of Zhu and Bertram confirmed this experiment and its interpretations [50].

2.7 Thermal Activation

In every real physical system thermal energy is present and this energy is used randomly by the system. Assuming a SDP with a uniaxial anisotropy at $T = 0\text{K}$ the magnetic moment is aligned along the easy axis. As long as the thermal energy is small compared to the anisotropy energy the magnetic moment will lie close to the easy axis. For higher temperature thermal energy can switch the magnetic moment. If the thermal energy is significantly larger than the anisotropy energy the magnetic moment will be oriented randomly in all directions and an ensemble of such particles is demagnetized. Applying an external field H to such a material will tend to align the moment in the field direction. This behaviour is that of a paramagnet and since the moments of the particles are much larger than those of atoms the material is called a superparamagnet. The normalized magnetisation $\frac{M}{M_s}$ in a paramagnetic material follows the Langevin function [3]:

$$\frac{M}{M_s} = \coth(\alpha) - \frac{1}{\alpha} \quad (2.26)$$

where α :

$$\alpha = \frac{mH}{k_B T} \quad (2.27)$$

With m the absolute magnetic moment of a single particle and k_B Boltzmann's constant. Since the material is demagnetized without an external magnetic field, it has no remanence and coercivity. A material with superparamagnetic particles of different sizes will exhibit a magnetisation curve composed of a sum of Langevin functions. However $\frac{H}{T}$ is the argument of each Langevin function and therefore magnetisation curves measured at different temperatures will superimpose when plotted versus $\frac{H}{T}$ [3]. This behaviour and the absence of hysteresis define a superparamagnet.

If an ensemble of particles with uniaxial anisotropy and having a thermal energy comparable to the anisotropy energy is saturated by a high field and the field is then reduced

to zero the magnetisation will decay with a relaxation time τ_N such that,

$$M(t_M) = M(0)e^{-t_M/\tau_N} \quad (2.28)$$

with t_M is the elapsed time and is the relaxation time after which the magnetisation is reduced to $\frac{1}{e}$ ($\approx 37\%$). Materials are defined as superparamagnetic for a typical dc measurement if the relaxation time is smaller than 100s [3]. This time was chosen since it is a typical time period for a measurement. The relaxation time depends on the anisotropy energy KV of a particle and the thermal energy $k_B T$ which for the alligned case is [3]:

$$\tau_N^{-1} = f_0 e^{-\frac{KV}{k_B T}} \quad (2.29)$$

f_0 is a frequency factor and has a value of $\approx 10^9 \text{s}^{-1}$ and is taken as constant [3]. The dependence on temperature means that for any superparamagnetic material with anisotropy a critical 'blocking temperature' T_B can be calculated below which the material ceases to be a superparamagnet. The dependence on the anisotropy energy KV means that for any temperature a critical particle volume V_P can also be found.

$$V_P = \frac{\ln(10^{11})k_B T}{K} \approx \frac{25k_B T}{K} \quad \text{and} \quad T_B = \frac{KV}{\ln(10^{11})k_B} \approx \frac{KV}{25k_B} \quad (2.30)$$

Usually materials consist of a distribution of particle-sizes, so the calculation of the critical volume indicates which fraction of the grains are superparamagnetic. The particles also vary in shape and the shape strongly influences the anisotropy as shown in equation 2.6 and that makes it difficult to determine from grain size analysis the fraction of superparamagnetic particles in a material. Calculating for a Iron prolate ellipsoid particle with an axial ratio of 1.1 the critical size for the long axis is 15.3nm.

In the same way as the anisotropy was treated as an energy barrier KV for the thermal energy in SDP systems, pinning sites of domain wall motion can be treated as energy barriers for the thermal energy in systems which are dominated by domain wall motion. For a single energy barrier an exponential time dependence behaviour as in equation 2.28 is expected, where KV is replaced by the pinning energy barrier [51]. However in real experiments with magnetic materials the time development of the magnetic moment to sudden changes in the external field tends to be logarithmic in time [51–54]:

$$M = S \ln\left(\frac{t_{ime}}{t_0}\right) + const. \quad (2.31)$$

with S is the time dependence coefficient and t_0 a time constant. The logarithmic behaviour is due to the distribution of energy barriers, which result in a spread of relaxation

times [54, 55]. S depends on the applied field and is according to Street and Wooley [52] proportional to the irreversible susceptibility χ_{irr} .

$$S = \chi_{irr} H_f \quad (2.32)$$

with H_f is a fictitious fluctuation field representing the effect of thermal energy [53, 56]:

$$H_f = \frac{k_B T}{V_{ac} M_s} \quad (2.33)$$

with V_{ac} the activation volume. The activation volume is the smallest volume of a material that can reverse in a single step. Using the energy barrier distribution for magnetization reversal E_b Gaunt [51] showed that

$$H_f = \frac{k_B T}{\left(\frac{\partial E_b}{\partial H}\right)_T} \quad (2.34)$$

is equivalent to equation 2.33 for SDP and for strong domain wall pinning, while for weak domain wall pinning:

$$H_f = \frac{k_B T}{2V_{ac} M_s} \quad (2.35)$$

For non-interacting SDP the activation volume is the particle volume. For materials reversing by domain wall motion, the activation volume is the effective volume of the material covered by a single jump between pinning centres for a domain wall motion process [56].

The time dependence of the magnetisation influences the measurement of normal magnetization curves. The magnetization value of a measurement with a lower ramp rate will be higher for increasing fields and lower for decreasing fields compared with higher ramp rate measurements. Therefore the measured coercivity $H(M=0)$ and the measured remanence $M(H=0)$ will be higher for higher ramp rates [57].

2.8 The Fe/MgO system

Bulk Iron is a soft magnetic material, meaning low coercivity. However the coercivity can rise when other materials are included due to pinning centres for domain wall motion. The saturation magnetization of bulk Iron is $M_s = (1746 \pm 8) \frac{emu}{cm^3}$ at 0K [58] and

$M_s = 1714 \frac{\text{emu}}{\text{cm}^3}$ at 20°C [3]. Iron under standard conditions is α -Iron and has a body-centred cubic (bcc) structure. The structure is reflected in cubic anisotropies in physical properties e.g. magnetization curves. The first order magnetocrystalline anisotropy constant at $T=300\text{K}$ is $K_1 = (4.8 \pm 0.1) \cdot 10^5 \frac{\text{ergs}}{\text{cm}^3}$ [59]. Iron turns to γ -Iron when heated over 912°C which is face-centred cubic (fcc) and further heating turns it to δ -Iron at 1394°C . 1538°C is the melting point. The temperatures of the phase changes are important for annealing procedures to reduce or increase stress and defects in the material. Uncontrolled oxidation on the sample surface of thin Fe films decreases the saturation magnetisation [60] and increases the electrical resistance. The exchange length in α -Fe is approximately 23nm [61]. After this length the exchange interaction is negligible.

Magnesium oxide MgO is strongly diamagnetic with a susceptibility of $-2.53 \cdot 10^{-7} \frac{\text{emu}}{\text{gOe}}$ [62]. It has a cubic, rock salt structure. It reacts with water and adsorbs water from the air at its surface. Therefore it is necessary to heat an MgO substrate to 400°C for about one hour before film growth. Fe can be grown epitaxially on MgO in the (001) direction due to the epitaxial relationship between $\text{Fe}(001)[110]$ and $\text{MgO}(001)[100]$ [63]. Figure 2.12 shows a model of the structure of the MgO/Fe(001) interface. A single layer MgO is shown on top of a single layer Fe. The MgO lattice is rotated by 45° relative to the Fe lattice. The oxygen atoms of the (first) MgO layer are on top of the Fe atoms. The square shows the borders of a single MgO unit cell.

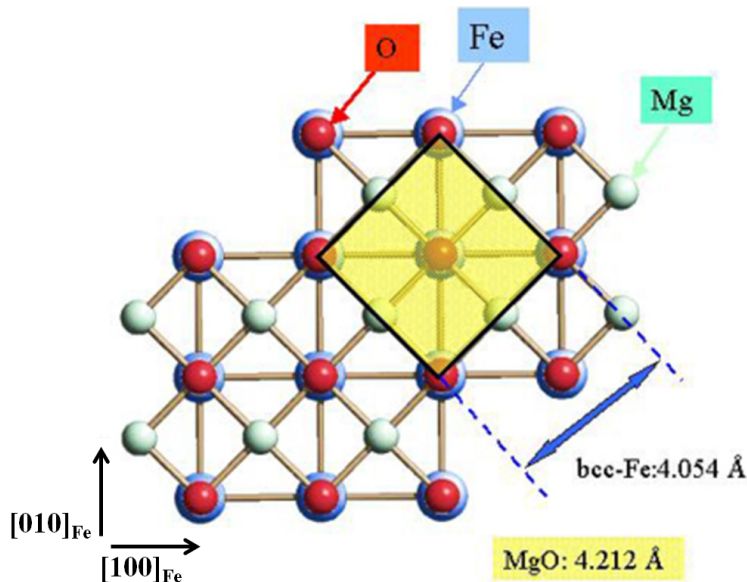


Figure 2.12: Model of the structure of the MgO/Fe(001) interface [4].

Fe-MgO-Fe tunnelling barriers have been studied extensively and are predicted to have

more than 1000% TMR [63]. García-García *et al.* [64] researched granular TMR in discontinuous Fe/MgO multilayers. They deposited epitaxial superlattices of Fe/MgO with Fe of thickness between 0.4nm and 1.5nm and MgO of thickness of 3nm by Pulsed Laser Deposition (PLD) on an MgO substrate. They found a percolation threshold of ≈ 0.8 nm for the Fe film thickness. Below that threshold the Fe formed superparamagnetic grains which show granular TMR. The TMR is up to $\approx 10\%$ at 30K and $\approx 3\%$ at RT. The sheet resistance at the thickness threshold was $1540\Omega\text{cm}$ and sharply increased for thinner Fe films.

Li and Freeman [65] calculated a 27% increase in the magnetic moment of an interfacial monolayer of Fe in an MgO matrix. Matsuo *et al.* [66] found experimentally an enhancement of the moment of Fe in MgO matrices. For films with a volume ratio Fe:MgO =3:1 this study also found an enhanced saturation magnetization of $\approx 20\%$ [9].

2.9 Magnetoresistance

Magnetoresistance in general is the dependence of the resistance on a magnetic field. In 1856 William Thomson (Lord Kelvin) was the first to discover this effect.

2.9.1 Electrical Resistance

The resistance of thin metal films can be fundamentally different from the bulk material. In a bulk metal the conductance is explained by the overlap of the valence and conduction bands. These bands are usually calculated by use of periodic boundary conditions and assuming a model of an infinite crystal with periodic potential [67]. The edges of the material are completely neglected. In thin films the edges cannot be neglected. When atoms come close, bonding, antibonding and nonbonding molecular orbitals are formed. These orbitals develop into bands the more atoms are brought together until the material becomes bulk-like. For a thin gold film, the sheet resistance is strongly dependent on the thickness of the film and also depends on the interface materials [68].

Another resistance effect in thin films can arise from the growth mode. If the growth mode is island growth, there is initially no direct path for a current to go through the sample as long as the islands are not connected. Tunnelling is the only possible transport mechanism in the film [69]. This results in a very high resistance with a strong temperature dependence. When the islands start to connect the current can find a path and with further connections the number of paths increases. Heating the substrate during growth or annealing can increase the homogeneity of the film and reduce the resistance.

In layer-by-layer grown metal films, the resistance can oscillate with the thickness which correlates with the intensity oscillations of the RHEED pattern [70](see section 4.2). This oscillatory behaviour is superimposed on the expected behaviour given by the model of Fuchs [71]:

$$\rho = \rho_0 \left(1 + \frac{3}{8} \frac{\lambda^*}{t} \right) \quad (2.36)$$

Where ρ is the resistivity of the film, ρ_0 the bulk resistivity, λ^* an effective mean free path and t the thickness of the film. The effective mean free path depends on the fraction of electrons which scatter inelastically from the surfaces and it depends on the interface materials [68]. A permalloy gold interface was found to increase the surface scattering and thickness dependence of the Au film significantly [68]. For Au below a thickness of about 5nm the resistance rises significantly. Au films of thickness larger than 30nm are well understood by considering angular dependent surface scattering, grain-boundary scattering and the bulk resistivity [71].

In the samples studied in this work a 5nm gold film is used as a capping layer. In the resistance measurement it is electrically parallel to the Fe:MgO film. A thick Au film will short-circuit the resistance measurement and prevent observations of magnetoresistance. A very thin Au film cannot protect the Fe in the film from oxidizing and the sample would change its properties. A protective layer of MgO would be an alternative but it would be difficult to make electrical contact with the film. Also the overall resistance would rise and increase the noise and heating of the sample if the same current is used. Bearing these things in mind a decision was made to use an Au capping layer of thickness 5nm.

2.9.2 Two current model of a ferromagnet

The two current model of conduction in a ferromagnet [72–79] assumes that the conduction of electrons is due to two independent spin channels. The model is simple and limited by the fact that these channels can influence each other by electrons flipping from one channel to the other. However this can often be neglected when it comes to understanding effects like GMR.

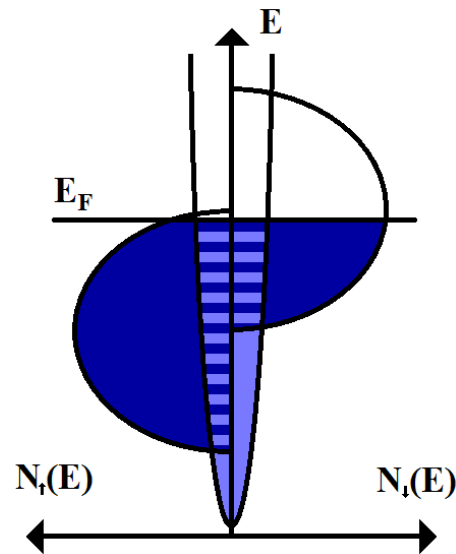


Figure 2.13: Schematic density of states of Fe.

Figure 2.13 shows a schematic diagram of the density of states (DOS) of Iron. Light blue colour in this figure represents the light electrons of the 4s-band, whereas dark blue colour represents the heavy electrons of the 3d band. Light or heavy electrons means the electrons have a low or high effective electron mass m^* . The electrons are in full energy levels up to the Fermi energy E_F . The left side of the figure shows the majority spin states and the right side the minority spin states, respectively, identical to spin up(\uparrow) and spin down(\downarrow), respectively, in uniformly magnetized materials [5]. The effective electron mass influences the mobility μ_{mobil} of the electrons [80]:

$$\mu_{mobil} = \frac{q}{m^*} \bar{\tau} \quad (2.37)$$

with $\bar{\tau}$ the average scattering time and q the charge of the electron. The electrons of the 3d band are less mobile because they have a much higher effective mass m_{3d}^* than the 4s

electrons [72]:

$$m_e \approx m_{4s}^* \ll m_{3d}^* \quad (2.38)$$

With m_e the mass of a free electron. This makes 4s electrons predominant for charge transport while 3d electrons contribute little. For each of the spin channels Matthiessen's Rule can be applied to calculate its resistance: The resistance of each spin channel is approximately the sum of the resistance of the electrons scattered within the s band (R_{s+s+} or R_{s-s-}) and the resistance of electrons scattered from the s to the d band (R_{s+d+} or R_{s-d-}):

$$\frac{1}{R} = \frac{1}{R_{s+s+} + R_{s+d+}} + \frac{1}{R_{s-s-} + R_{s-d-}} \quad (2.39)$$

The + (-) in the notation represents the majority (minority) spin channel of the charge carriers. In ferromagnets at Fermi energy E_F there are for both spin directions different DOS in the 3d-band, while the 4s-band the DOS is the same for both spin directions. The scattering from 4s to 3d for each spin direction is proportional to the occupied states of 4s and the free states of 3d close to the Fermi energy. Since the occupied 4s states are the same for both spin directions, whereas the free states from 3d differ strongly for both spin directions, the scattering probability is higher for the spin states with a higher density of free 3d states at the Fermi energy. This results in a higher resistance for electrons of this spin direction. For example ferromagnetic Nickel has no empty 3d majority states (3d+). The resistance contribution R_{s+d+} from s-d scattering is therefore zero. The resistance in the majority channel is solely due to s-s scattering (R_{s+s+}). In the minority channel there is s-d scattering (R_{s-d-}) in addition to the s-s scattering (R_{s-s-}), resulting in a higher resistance for that channel and therefore a higher spin current for majority spin state charge carriers.

2.9.3 Ordinary Magnetoresistance

All conducting materials show a resistance change in magnetic fields due to the Lorentz force. This resistance change is very small for metals unless the field is very high. A magnetic field \vec{B} causes a Lorentz force \vec{F} on a charge carrier when the charge q is moving with a speed \vec{v} :

$$\vec{F} = q(\vec{E} + \frac{\vec{v}}{c_0} \times \vec{B}) \quad (2.40)$$

With \vec{E} the electrical field and c_0 the speed of light in vacuum. This force is perpendicular to the direction of the motion and therefore causes an elongation of the path an electron takes through a material. This means that the scattering probability rises with the magnetic field and therefore also the resistance R . The resistance $R(B)$ is proportional to the square of the magnetic field induction B perpendicular to the plate [81]:

$$R(B) = R_0 \frac{\rho_B}{\rho_0} (1 + \mu^2 C_{MR} \cdot B^2) \quad (2.41)$$

Where: R_0 is the resistance of the material in the magnetic field $B = 0$, $\frac{\rho_B}{\rho_0}$ is the magnetoresistance coefficient, μ is the carrier mobility, and C_{MR} is a coefficient depending on the geometry of the sample.

2.9.4 Anisotropic Magnetoresistance

The anisotropic magnetoresistance effect (AMR) is dependent on the orientation of the magnetization of a material with respect to the direction of the current. This effect is explained by the spin orbit interaction (SOI). The magnetic field and the spin orbit interaction influence the scattering of electrons by mixing the 3d+ and 3d- states. This mixing is anisotropic and causes more free states in the 3d band with wave vector direction parallel to the magnetisation than those perpendicular to it. This results in a higher probability of s-d scattering when electrons travel parallel to the magnetization and a lower scattering probability when they move perpendicular to it. The resistance perpendicular is therefore lower than the resistance parallel to the magnetic field. A more detailed overview of MR and its applications can be found in the book of Tumanski 'Thin Film Magnetoresistive Sensors' [81].

2.9.5 Giant Magnetoresistance

The Giant Magnetoresistance effect was discovered by Grünberg [12] and Fert [13] independently in 1988. They received the Nobel Prize for Physics in 2007. Their research was done with multilayer systems of ferromagnets and non magnetic metals and the current was applied along the layers. This is called 'current in plane' (CIP) geometry. Larger

resistance changes were later found for the 'current perpendicular to the plane' (CPP) geometry. In this geometry the current flows first through a ferromagnet then through a non magnetic metal and finally through a second ferromagnetic layer. The resistance depends on the relative direction of the magnetization of both layers. The resistance is lowest for parallel and highest for anti-parallel magnetization directions. Assuming a simple 2 current model with just these two extreme cases and identical ferromagnets as shown in figure 2.14, we can calculate the resistance R of such a device from the resistance of majority electrons R_+ and minority electrons R_- in the ferromagnet and the resistance of the non-magnetic metal $R_{nonmagnet}$:

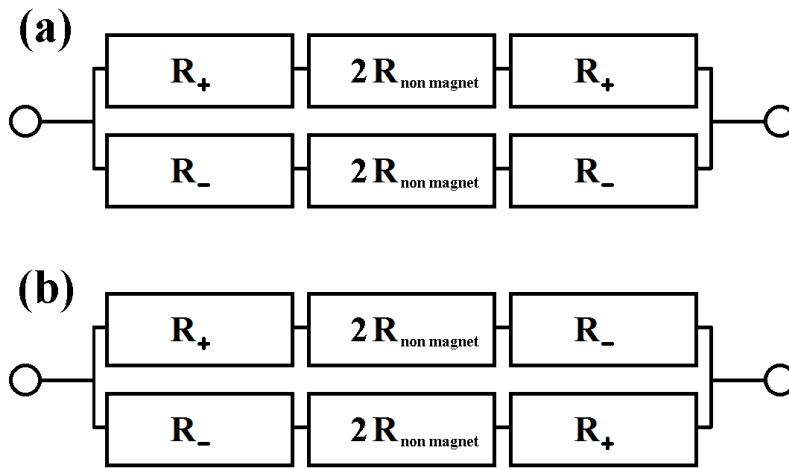


Figure 2.14: (a) Parallel and (b) anti-parallel configuration for two current model of the GMR effect.

$$R_{parallel} = \frac{1}{\frac{1}{R_- + 2R_{nonmagnet} + R_-} + \frac{1}{R_+ + 2R_{nonmagnet} + R_+}} \quad (2.42)$$

$$R_{anti-parallel} = \frac{1}{\frac{1}{R_+ + 2R_{nonmagnet} + R_-} + \frac{1}{R_- + 2R_{nonmagnet} + R_+}} \quad (2.43)$$

Since half the conductivity in the non magnetic material is for each spin channel the spin resistance in this channel is $2 \cdot R_{nonmagnet}$. It can be shown that the parallel resistance is lower than the anti-parallel resistance whenever the resistance of minority and majority spin electrons differs.

2.9.6 Tunneling Magnetoresistance

In 1975 Jullière discovered that the conductance of FeGeCo junctions depends on whether both magnetic layers are parallel or antiparallel to each other due to the spin polarization of the conduction electrons [82]. The resistance of ferromagnets which are separated by an insulator on the relative orientation of these ferromagnets is called tunnelling magnetoresistance (TMR). The discovery of TMR at room temperature in 1994 [83, 84] opened the possibility of applications such as highly sensitive magnetic-field sensors, magnetic read heads, and non-volatile magnetic memories. Jullière reported a TMR ratio

of 14% at 4.2K. A TMR ratio of 18% at room temperature was found by Miyazaki [83]. Utilizing coherent tunnelling, Fe/MgO/Fe junctions are predicted to show more than 1000% TMR [63]. In 2009 Ikeda et al. reported a TMR ratio of 604% at 300K and 1144% at 5K for CoFeB/MgO/CoFeB pseudo-spin-valves [21]. Such a large TMR ratio satisfies the requirement to ensure short integration times when reading information from magnetic random access memories (MRAM). However, the resistance must not be too high since a small resistance area product (RA) would allow for faster switching times [85]. In 1995 Fujimori et al. discovered a granular TMR effect in $Co : Al_2O_3$ granular thin films [18]. Ferromagnetic particles dispersed in an insulating matrix are interesting for various spintronic applications especially spin-polarized co-tunneling devices. Epitaxial and polycrystalline co-evaporated Fe:MgO systems were studied by Tanaka et al. in terms of their structure [86] and by Matsuo et al. in terms of their magnetic properties [66]. García-García et al. measured the TMR in discontinuous Fe/MgO multilayers [64]. They found TMR values of up to 9.2% for epitaxial multilayers deposited by PLD on MgO substrates. Despite the fact that TMR was discovered 13 years before the GMR, little attention was paid to that effect until the discovery of GMR. The principle of a TMR

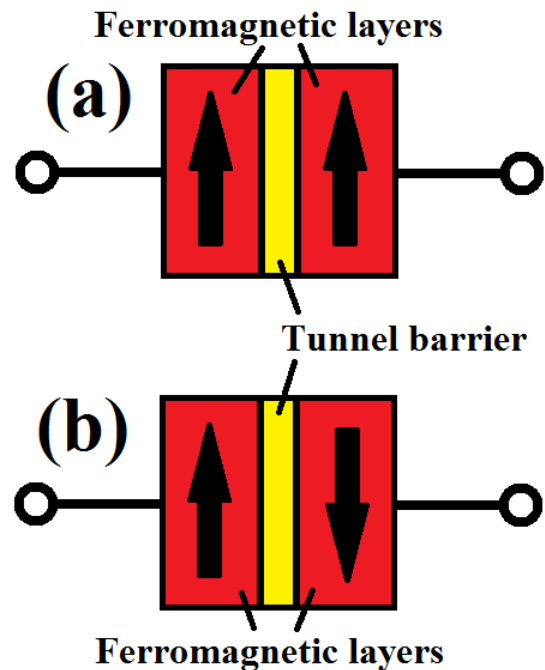


Figure 2.15: Anti-parallel (a) and parallel (b) configuration of CPP TMR setup.

system is similar to a CPP GMR system with the only difference being that the conductor between both ferromagnets is replaced by an insulator as shown in figure 2.15. The TMR ratio is:

$$TMR = \frac{R_{\uparrow\downarrow} - R_{\uparrow\uparrow}}{R_{\uparrow\uparrow}} \quad (2.44)$$

where $R_{\uparrow\uparrow}$ is the resistance if the magnetic moments are aligned parallel (figure 2.15 (a)) and $R_{\uparrow\downarrow}$ for the antiparallel (figure 2.15 (b)) case. Tunnelling requires that an electron on one side of the barrier is in the same state in the band-structure where there is an empty state on the other side of the barrier. The electron cannot change its wave-vector nor the symmetry of its wave function during a tunnelling process. In reality the insulating layer often provides defects where the electron can scatter or even pass the barrier without the need to tunnel directly from one side to the other. These defects reduce the overall resistance of the tunnelling barrier but also reduce the TMR effect. As an electron needs a sufficient energy to cross the barrier it acts as an energy filter. The probability for tunnelling also depends on the thickness of a barrier. An electron which does not tunnel perpendicular to the insulating layer follows a longer path resulting in an effectively thicker barrier. The thickness reduces the probability of tunnelling exponentially meaning that electrons with a sufficiently high wave vector projection on the axis perpendicular to the insulating layer can cross the barrier. This way the barrier acts as a filter for wave vectors and filters out electrons with a high wave vector projection parallel to the plane of the insulator and just elections with close to perpendicular wave vectors are able to tunnel.

The TMR ratio for a tunnelling junction can be calculated from the polarisations P_1 and P_2 of the electrons on both sides of the barrier [87]:

$$TMR = \frac{2P_1P_2}{1 - P_1P_2} \quad (2.45)$$

The polarisation P is defined as

$$P = \frac{D_{\uparrow} - D_{\downarrow}}{D_{\uparrow} + D_{\downarrow}} \quad (2.46)$$

D_{\uparrow} and D_{\downarrow} are the densities of electrons with spin up and down, respectively. These are the occupied states. In general occupied states are calculated by integrating the product of DOS and Fermi-Dirac distribution over all energies. Spin-flip scattering within the tunnelling barrier and leak currents through the barrier reduce the TMR ratio. Therefore experiments usually find lower TMR values than those predicted by equation 2.45.

In granular TMR the electrons are transported by tunnelling from one grain to the next through the film. This makes granular TMR similar to the conductance process for thin films with island growth before the islands come into contact as described in section 2.9.1. In granular TMR the ferromagnetic grains are separated by an insulating material. There is no direct path for the current and tunnelling from one grain to the next is required for conduction.

Takahashi [88] showed that the TMR ratio in magnetic tunnel junctions can be significantly increased by a Coulomb blockade. It is well known from quantum dots (QD), that their electrons occupy discrete energy levels. These levels are often approximated using a simple particle-in-a-box model [89]. The distances between these levels depends on the size of the quantum dot: The smaller the dot the larger the difference between the levels. The energy needed for tunnelling of an electron into a ferromagnetic QD depends on the level of the first unoccupied level in this grain. After an electron tunnels to a QD the next free level is much higher than the level of the electron which has just arrived. If there is a small voltage applied the additional electron in the QD will prevent further electrons from tunnelling into this QD. This is called a Coulomb blockade. The additional energy needed to tunnel into the next higher state is the Coulomb charging energy. Without this energy an electron needs to leave the QD, again by tunnelling, before a new electron can tunnel into the QD. This process of sequential tunnelling of electrons is called cotunnelling and several potential applications may make use of this process e.g. a single-electron-transistor (SET) and granular TMR materials, where small grains act as quantum dots. In SETs the quantum dots are usually produced by lithography whereas in granular TMR the quantum dots are a result of the growth process of the film. Transport models assume that in between two larger grains one or more small gains act as quantum dots and are required for the transport. The tunnelling process depends strongly on temperature. Cotunnelling transport is dominant if the Coulomb charging energy is larger than the thermal energy $k_B T$. This can be achieved by small QD or low temperatures. For very small QD the Coulomb blockade can be observed in SET at room temperature (RT) [90]. At 5K temperature in a granular Fe-Al₂O₃ film with a Fe volume fraction of 0.45 cotunnelling was observed [91].

There are several models [64,91–94] and simulations [23,95] for the TMR of granular

films. The TMR for granular films is given by [64]:

$$TMR = -P^2 \left(\frac{M}{M_s} \right)^2 \left(1 + \sqrt{E_C \delta s \kappa T k_B} e^{-k_B T / E_{mr}} \right) \quad (2.47)$$

where P is the spin polarization of the tunnelling electrons, E_C is the energy necessary to generate a pair of neighbouring charged grains during the tunnelling process, T is the temperature, k_B is the Boltzmann's constant, E_{mr} is an energy value associated with spin-flip scattering processes which can change the spin of the electrons involved in the tunnelling event and κ is [92]:

$$\kappa = \frac{\sqrt{2m^*(U_{bar} - E_F)}}{\hbar} \quad (2.48)$$

where \hbar the reduced Planck constant and U_{bar} an effective potential barrier.

Yang [95] simulated the effect of dipolar and intergranular exchange interactions on granular TMR. He found that in the absence of exchange interactions the TMR decreases with rising dipolar interaction but for strong exchange interactions the TMR increases with rising dipolar interaction. It was also found that the maximum TMR is reached at the coercivity. Mao and Chen also found by simulation that the maximum TMR is nearly independent of dipolar interactions while it decreases with an increasing exchange interaction [23]. They simulated TMR for non-interacting particles with uniaxial anisotropy and the dependence of the TMR curve on the direction of the anisotropy of the particles and found that maximum TMR is independent of the distributions of the anisotropy axes. However the field sensitivity is highest (lowest) for anisotropy axes aligned along (perpendicular to) the applied field direction.

2.9.7 Other Magnetoresistance Effects

Magnetoresistance can also depend on the sample shape. A magnetic field in the direction of the current can trap the electrons in helical paths and therefore increase the path length. This path length increase will increase the resistance in a bulk material. However for a current flowing in a thin film, the same effect will reduce the surface scattering. This scattering becomes increasingly dominant in the total resistance for thinner films. Therefore for very thin films the resistance can decrease with increasing magnetic field.

Domain walls have also influence on the magnetoresistance. Assuming a 2 current model, domain walls, increase the resistivity by mixing minority and majority spin channels and therefore eliminating the short-circuit provided by the low resistivity spin channel in a single domain ferromagnet. External magnetic fields can deform and move domain walls and domains can expand until a magnet is completely saturated. This eliminates domain wall scattering and therefore reduces the resistance. More sophisticated models of domain wall scattering predict a resistance increase or decrease when a magnetic field is applied [96].

Chapter 3

Material Requirements for Spintronics

3.1 Magnetic Materials

The giant magnetoresistance effect (GMR) was discovered in 1988 [12, 13] and soon after applied in read heads of hard disk drives. It was first found in current in plane (CIP) experiments, but the effect is much stronger when the current flows perpendicular to the layers (CPP). In a GMR sensor there is a fixed (pinned) magnetic layer and a free magnetic layer separated by a non-magnetic metal. The free layer takes the orientation of the external fields, while the pinned layer is not influenced by external fields and it keeps its magnetization direction through exchange coupling with an antiferromagnetic film, usually IrMn. The magnetoresistance (MR) of the sensor is proportional to the vector product of the magnetization of both layers:

$$MR \propto \vec{M}_1 \cdot \vec{M}_2 = M_1 M_2 \cos(\epsilon) \quad (3.1)$$

With ϵ the angle between the magnetizations of both magnetic layers. The pinned layer is perpendicular to the easy axis of the free layer. This ensures a maximum sensitivity to changes in the magnetic field. Another advantage of this operating point is that the change in MR is quasi-linear to the change of the angle ϵ for small angles. For high MR the magnetization of both layers also must be large and for high sensitivity the coercivity of the free layer must be as low as possible. CoFe or CoFeB is therefore a good choice for the pinned layer. Permalloy (NiFe) can be used as a free layer due to its low coercivity,

but its magnetization is much lower than CoFe. To use CoFe as free layer low coercivity can be achieved by growing the material with small grains [97–99].

Ikeda *et al.* [21] found very high TMR values in spin valves with the material system Ta/Co₂₀Fe₆₀B₂₀/MgO/Co₂₀Fe₆₀B₂₀/Ta. To optimize the tunnelling barrier they annealed the system at different temperatures and found that it was critical to anneal the structure at high temperature above 500° C. They also showed that an improvement of MgO barrier quality, in terms of the degree of (001) orientation and stress relaxation, takes place at annealing temperatures above 450° C. Due to the good lattice match between Fe and MgO the systems of Fe/MgO are expected to show high TMR [63, 100].

Half-metals like Heusler alloys are also of great interest in spintronic devices. At the Fermi energy the band structure is metallic for one spin direction, while it has a band gap for the other spin direction. This means that the current within the material is completely polarized. A TMR could theoretically be infinite and theoretically a pure spin current could be injected into nonmagnetic materials. However epitaxial growth with good interface properties are difficult to achieve [101].

3.2 Non-magnetic metals

Copper is used in GMR devices as a spacer layer due to the good band matching to both Fe and Co as shown in figure 3.1. The majority band, indicated by a + in the diagram, of Co and Fe matches the same band in Cu, while the minority bands do not match. This allows an efficient spin injection from the Co and Fe into Cu. The minority band of Fe and Co matches the band structure of Cr.

GMR was originally found when researching artificial antiferromagnets. In such a material magnetic layers are separated by non-magnetic spacer layers and the layers align to each other antiparallel. This alignment is due to interlayer exchange coupling. Interlayer exchange coupling is periodic between positive (ferromagnetic) and negative (antiferromagnetic) depending on the thickness of the spacer layer. An external magnetic field can align the layers of a synthetic antiferromagnet parallel and then the resistance decreases due to the GMR effect. Parkin [102] systematically researched the antiferromagnetic

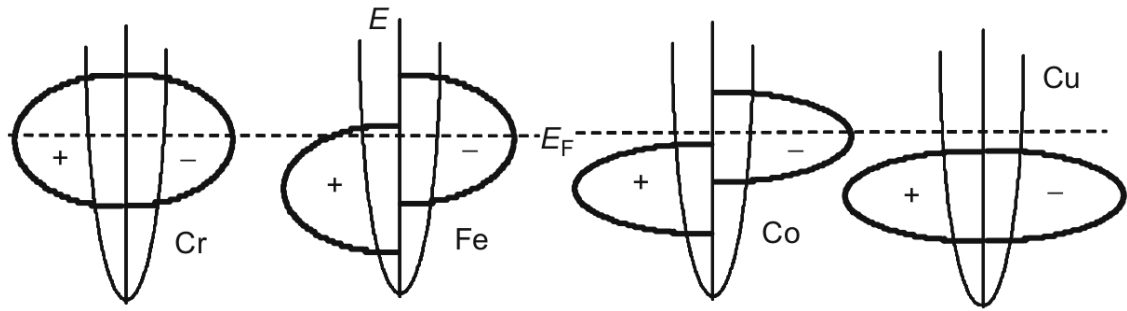


Figure 3.1: Schematic density of states (DOS) of Cr, Fe, Co and Cu [5].

interlayer exchange coupling of different 3d,4d, and 5d transition metals sandwiched between Fe, Co, Ni, or Ni alloy magnetic layers. Coupling was found using V, Cr, Cu, Nb, Mo, Ru, Rh, Ta, W, Re and Ir and no coupling was found using Ti, Zr, Hf, Pd, Pt, Ag and Au spacer layers. The exchange strength oscillates with the thickness of the spacer layers. The oscillation period is approximately 1nm and almost independent of the transition metal used as the spacer. Only for Cr is the oscillation period much larger at 1.8nm to 2.0nm. The strength of the coupling systematically increases from the 5d to 4d to 3d elements and increases exponentially with the number of d electrons along the 3d, 4d, and 5d periods [102].

Antiferromagnetic interlayer exchange coupling is not necessary for GMR effects. Another possibility is to have an exchange coupled fixed layer and a free layer. The preferred direction of the free layer can be set by shape anisotropy to be perpendicular to the fixed layer as discussed earlier. The third possibility is to have non-coupled layers with random orientation of the magnetization. This random orientation can be ordered by an external magnetic field and therefore give rise to a resistance drop through the GMR effect. If these un-coupled layers are replaced by single domain particles in a nonmagnetic matrix, a granular GMR effect is obtained [103]. Berkowitz *et al.* found this effect in a Co-Cu film. There is virtually no solubility of Co in Cu therefore a heterogeneous polycrystalline film consisting of Co and Cu grains can be produced by sputtering. It was found that the magnetoresistance scales inversely with the average particle diameter. This behaviour was modelled by including spin-dependent scattering at the interfaces between the particles and the matrix, as well as the spin-dependent scattering in the Co-rich particles [103].

GMR devices have now been replaced by TMR devices in almost all applications with the exception of high temperature applications. Copper as a material for transporting spin

current is still used in all-metal systems for spin transfer torque and Permalloy is typically used for injectors and detector/switchable particles [104, 105]. Gold is used to connect the permalloy particle from the other side because it increases the spin absorption into the permalloy [106].

3.3 Semiconductors

Semiconductors are of great interest for spintronic applications because of the large spin-flip length. In a magnetic metal this length is just a few nanometers, in non-magnetic metals it can be a few hundred nanometers at RT or up to about $1\mu\text{m}$ for Cu at 4.2K [107]. For semiconductors the spin flip length can be much larger. GaAs can have a spin-flip length of more than $100\mu\text{m}$ [108]. The spin flip length depends on the spin lifetime and the diffusion speed which is proportional to the mobility of the electrons. The mobility of electrons in GaAs is approximately 3 to 4 times larger than that in Silicon. Another advantage of GaAs is the direct band gap which produces light through the recombination of electrons and holes. Polarized electrons produce circular polarized light [109, 110]. The band gap is directly related to the wavelength of the light and can be modified to fit the needs of the application by substituting atoms (e.g. AlGaAs). A material system of GaAs/GaAlAs($\approx 5\text{nm}$)/GaAs can form a 2 dimensional electron gas (2DEG), where all electrons move within a 2D plane. This is required for a spin transistor [10, 14]. Spintronics on silicon could combine the state of the art conventional chip technology with spintronics.

However a major problem for semiconductor spintronics is the spin injection. The resistance of all semiconductors is much larger than the resistance of ferromagnetic metals. This resistance mismatch, also called "impedance mismatch problem", gives rise to a fundamental obstacle for spin injection from a ferromagnetic metal into a diffusive semiconductor [111]. To overcome this mismatch high resistance magnetic materials like dilute semiconductors or magnetite can be used as injectors or the injection can be done through a tunnel barrier. A Schottky barrier can also serve as tunnel barrier [7, 112]. CoFe/MgO/ GaAs injectors are of great research interest and can reach levels of polarizations of up to 70% in spin diodes with almost no temperature dependence [109, 110].

Also for Si the prevalent method is to insert an artificial (oxide) tunnel barrier between a ferromagnet and silicon [113]. However for Si with low to moderate doping concentration the contact resistance is determined not by the tunnel oxide but by the much larger Schottky barrier [113]. A large contact resistance can decrease the spin accumulation in some devices. It also prevents high frequency operation and for wide Schottky barriers the transport does no longer occur by tunnelling but by thermionic emission [113]. To reduce the width of the Schottky barrier and prevent carrier depletion in the semiconductor, a high doping concentration of the semiconductor can be used [113, 114].

For spin injection the surfaces are very important. Different materials have different lattice constants which cause defects and stress at the surface. Defects can cause a short in the tunnel barrier. They can cause spin-flip scattering and therefore reduce the degree of polarization. Stress changes the lattice constant locally and therefore changes the local band structure and electronic and magnetic properties. At an atomic level the stress at the interface is more or less inhomogeneous. Therefore there is great interest in making smooth and well defined interfaces. Usually epitaxial growth with good lattice matching is needed. Annealing procedures at high temperature is also required to produce such surfaces. However excessively high temperatures may cause unwanted diffusion or chemical reactions. Tiny amounts of chemical impurities can change the electrical properties of semiconductors significantly and small amounts of impurities in the injector can reduce the spin polarization. Table 3.1 shows the lattice constants of a range of materials which might be used as spin injectors.

	Structure	Lattice constants[nm]
Si	Diamond cubic	0.357 nm [115]
GaAs	Zinc blende	0.357 nm [116]
MgO	rock salt	0.421 nm [117]
Al ₂ O ₃	trigonal ($R\bar{3}c$),cubic spinel ($Fd\bar{3}m$) like and other	cubic: ≈ 0.357 nm [118]
Fe	bcc	0.286 nm [119]
Co	hcp ,(bcc)	bcc: 0.2827 nm [120]
CoFe	bcc,fcc,hcp	bcc: 0.2830 - 0.2862 nm [120]

Table 3.1: Structures and lattice constants for some important spintronic materials.

Iron can be grown epitaxially on GaAs because the lattice constant of GaAs is almost exactly double that of Fe with a lattice mismatch of 1.35%. The interface can have dif-

ferent atomic configurations [7]. Bulk Cobalt at RT is hcp. However when it is grown epitaxially on GaAs it crystallizes in a bcc structure [120]. This phase is metastable and stabilized by the lattice match to the GaAs. FeCo alloys are bcc if the Fe atoms are at a level of greater than 25%. Alloys with less Fe obtain progressively mixed phases of bcc, fcc and hcp [120]. It is reasonable that all mixtures of Fe and Co can grow epitaxially on GaAs in a bcc phase since the bcc-lattice constant changes almost linearly between Iron and Cobalt [120, 121]. Different Heuser alloys can also be grown epitaxially on GaAs. However it is difficult to obtain highly ordered, stoichiometric and thermally stable thin films, which are required for spin-polarization. The Heusler alloy Co_2FeSi can be grown epitaxially on GaAs(001) and it shows a spin polarization of about 60% [122].

Using a Si(111) substrate it is possible to grow Fe(111) epitaxially with Fe[110] parallel to Si[110] [123]. It is difficult to grow Co epitaxially on Si. The metastable fcc phase can be grown epitaxially on Si(001) and Si(111) using a thin Cu buffer layer [124]. Several Heusler compounds (e.g. Fe_3Si [125] and Co_2FeSi [126]) can be grown epitaxially on Si(111). Furthermore Magnetite (Fe_3O_4) can be grown epitaxially on Si(001) [127].

3.4 Insulators

Insulators are important for several applications: They are used to provide tunnelling contacts for TMR devices and spin injectors. They are also used to insulate the gate of a FET or SpinFET and finally to preventing leakage currents through the substrate. Before the implementation of semiconductor on insulator wafers one of the main sources of power consumption in chips was leakage currents. Silicon on insulator is now the standard wafer for chip production. Such wafers are produced by e.g. implantation of oxygen into the silicon, followed by annealing to create a buried SiO_2 layer. Another way to produce such a wafer is by thermally oxidizing a silicon wafer and a second layer of silicon is wafer-bonded on top of it.

There are at least seven different phases of Alumina (Al_2O_3) [118]. The trigonal α -Phase is thermally stable and known as corundum or sapphire. It is very hard, very dense and a very good insulator. It can be grown as a single-crystal and cut into wafers. Si can

be grown epitaxially on top of this material. The wafer diameters are up to 20cm [128] which is small compared to standard Si wafers which are up to 40cm in diameter. These wafers are expensive and only used for applications which need very good insulators such as high power applications, RF applications and for chips in satellites due to their radiation resistance. Corundum induces stacking faults and twins into the Si when it is grown on top of it. These can be removed by a procedure of implantation and annealing. Another method for the fabrication of high quality single crystalline layers on corundum is wafer bonding [129]. However it is difficult to make good quality thin epitaxial layers of corundum required for tunnel barriers or gate insulators. Alumina can be grown epitaxially in a metastable cubic phase (γ phase) on Si(111) [130] making it interesting as tunnelling barrier or gate insulator. However high-quality amorphous Aluminium oxide seems to be more practical [131, 132] for Si and GaAs.

For gate and tunnelling contacts engineers try to reduce the thickness of the insulating layer in order to decrease the contact resistance and to increase the operating speed of the devices. For tunnelling barriers as small as 1nm the problem of short-circuits through the barrier, so called pinholes, becomes a major problem. Other metal oxides like TiO_2 , TiAlO_3 and MgO were researched to overcome this problem [21, 133–135].

MTJs with amorphous Al_2O_3 have TMR ratios of $\approx 70\%$ at room temperature. MTJ with MgO barriers were found to have much higher TMR ratios. Epitaxially grown MgO barriers between Fe layers were found to have up to 180% TMR [136]. With MgO sandwiched between CoFe on an amorphous substrate a TMR of 220% was found [133]. Djayaprawira *et al.* [134] showed that MgO tunnelling barriers are significantly improved when the MgO is grown on amorphous CoFeB and annealed instead of polycrystalline CoFe and found TMR ratios of 230% at RT. Based on this finding Ikeda *et al.* [21] then found much larger TMR ratios of 604% at 300K in the same material system by optimizing the annealing procedure.

Chapter 4

Thin Film Growth

There are two approaches to nanotechnology which are bottom up and top down. Thin film growth plays an important part in top down technologies. It is needed to bring different materials into contact.

4.1 Vapour Deposition

The most common way of growing thin films in research laboratories is vapour deposition. There are two different vapour deposition systems: chemical vapour deposition (CVD) and physical vapour deposition (PVD). In CVD precursors are used which react and/or decompose on the substrate surface. In PVD a solid or liquid source is evaporated and this vapour is then deposited onto a substrate.

CVD processes are usually undertaken in a gas atmosphere. In a typical CVD process gas with precursor molecules flows through a chamber with heated wafers. The heat stimulates the reaction/decomposition of the precursors and enhances the mobility of the molecules on the surfaces of the wafers. The reaction/decomposition of the precursors may also be stimulated by a plasma or laser. CVD can be used to produce thick films. CVD processes are beyond the scope of this work and a good introduction into CVD and all other thin film processes described in this section can be found in J.L. Vossen and W.Kern 'Thin Film Processes II' [6] .

In PVD the evaporation is usually done by heating the source. There are several different ways of heating. In thermal evaporation the container of the source is heated either directly by putting the source into a conduction boat and driving current through or indirectly by heating the crucible that contains the source like in Knudsen effusion Cells (K-Cells), which additionally have precise temperature control and a shutter. Another method is Electron beam evaporation: Electrons are accelerated and then hit the source and therefore heating up the spot of impact. The advantage of this technique is that the source can be rather easily exchanged within an evaporation system without venting the vacuum system. The disadvantage is that the temperature control is not precise. There is a temperature gradient between the point where the electron beam impacts and the crucible. This will cause more evaporation from that point and may even drill a hole in the source. If the source heats up too much it can cause boiling and splashing of droplets. To counter this effect some electron beam evaporation systems have a steering magnet causing a constant change of the impact position of the electron beam. Another disadvantage of evaporation systems is that materials such as alloys often have different evaporation temperatures for the different components. This leads to a different stoichiometry in the vapour compared to the source. Also the stoichiometry of the vapour of a source can change with the time of use of the source. To cope with this problem sources with intentionally different stoichiometry can be used and evaporation simultaneously from more than one source (co-evaporation) can be used. Another way to solve this problem is the use of pulsed laser deposition (PLD). Very short laser pulses heat the area of impact rapidly and a plume ejects from this point on the source. The source is moved between pulses to prevent the laser from drilling a hole and to have reproducible evaporation from each pulse. The amount of material evaporated is then proportional to the number of pulses giving accurate thickness control of the deposited film. The disadvantage of PLD is the slow deposition speed and the limited size of the substrate area on which material can be deposited with uniform thickness. A detailed introduction into PLD is given by Chrisey and Hubler [137]. An introduction into PVD including MBE and sputter deposition is given by Schuegraf [138].

4.2 Epitaxial MBE Growth

For PVD the deposition rate plays an important role for quality of the deposited material. For slower deposition the atoms or molecules have more time to find the most energetically stable position for them on the substrate. Heating the substrate will also increase the mobility of the atoms on the surface. This way crystalline growth will be more likely and the film tends to have less defects. High temperature can also cause defects in crystals especially if they are cooled too fast. High substrate temperatures can also cause an intermixing of substrate atoms with atoms of the film, therefore the temperature must be controlled carefully. Single crystal substrates can cause the film to have preferred crystalline directions with respect to the crystalline direction of the substrate. These films are then called epitaxial. In the simplest case the material has an identical structure to that of the substrate. This is then called homoepitaxial growth. In other cases the lattice constants of the films are similar or have common multiples of the lattice constant of the substrate. In this case a different material may grow epitaxially on a substrate and this is called heteroepitaxial growth. Any lattice mismatch causes stress in the film and usually also defects at the interface.

There are three principle growth modes for epitaxial films: Layer-by-layer growth mode, also known as Frank-van der Merwe growth mode, island growth mode, also known as Volmer-Weber growth mode and combination of previous mentioned modes, known as layer-plus-island growth mode or Stranski-Krastanov growth mode [139–142]. The energy state of an atom on the surface of a material depends on the neighbouring atoms. The more neighbours are missing the less stable is an atom. The atoms can move on different speeds on the surface depending on the temperature and the atomic binding. Through this process the atoms find more stable locations. For each additional neighbour the atomic position becomes more stable. From this point of view one layer forms after another as soon as the layer is complete, because any atom at a higher level than the first incomplete level can find a more stable position within this layer. The other influence on the energy is the lattice mismatch. This way layer-by-layer growth is limited to homoepitaxial growth while the other modes appear in heteroepitaxial growth.

A Molecular Beam Epitaxy (MBE) system is an Ultra High Vacuum (UHV) system

to grow epitaxial films. The mean free path in the vacuum should be large compared to the distance between the evaporation source and the substrate. This ensures there is no interaction between the vapour molecules and the gas and no gas molecules in the film. K-Cells and PLD can be used as MBE sources. With some limitations electron beam evaporation systems can also be used. Most MBE systems have a substrate heater and temperature controllers. Quartz Thickness Monitors are used to measure the thickness of the film during the growth process. A Quartz Thickness Monitor consists of a quartz single crystal which is driven by an AC current through the piezoelectric effect. The resonance frequency drops when additional mass is evaporated onto the resonator. To a first approximation the frequency shift is proportional to the additional mass [143]. Knowing the density of the evaporated material and the sensor area, the thickness can be calculated. PVD sources usually do not evaporate in all directions at exactly the same rate, so there is a factor due to the fact that the sensor is at a slightly different direction from the source compared to the substrate. By measuring the thickness via another technique like TEM or an ellipsometer the proportionality factor can be determined and the system calibrated.

Another instrument often used to monitor the growth in an MBE system is Reflection High Energy Electron Diffraction (RHEED). Electrons are accelerated to typically about 20kV and are reflected under a low angle of about 2° to the substrate during growth. The periodic surface structure causes a diffraction pattern in the reflected beam due to Bragg-reflection. Analysing this pattern allows conclusions to be drawn about the periodic surface. In general surface atoms are missing neighbouring atoms in one direction and that results in so called 'dangling bonds'. These dangling bonds result in a high surface energy and to reduce this surface energy, the atoms order themselves in a supra lattice at the surface called a surface reconstruction. Here the indices indicate how many unit cells from one cell of the supra-lattice. The symmetry and periodicity are also found in the RHEED diffraction pattern and help identify the configuration of the surface atoms. During the growth of the crystal the intensities of individual spots on the RHEED patterns change. A plane surface gives the highest intensity spots. As the first layer of atoms assembles the intensity decreases due to the two different levels that occur where atoms have already arrived at the surface and where the substrate has not been coated. Assuming a layer-by-layer growth mode, whenever a layer is completed a maximum in the intensity is reached and whenever a layer is half occupied, a minimum is reached. This results in a periodic

intensity change during growth. This way it is possible to count the number of layers deposited. A detailed introduction in RHEED is given by Dhez and Weisbuch [144].

4.3 Growth by Sputtering

Sputtering is a technique where impacting ions (typically Argon) transfer energy to surface atoms of a target to eject atoms. Sputtering can be used for removing material such as thin films, but in sputter deposition the target is the source of a material and its atoms fly to the substrate and deposit onto it. The process is almost as stoichiometric as PLD, but much faster than PLD, making it common for industrial purposes. Epitaxial films are difficult to achieve by sputter deposition. The atoms sputtered onto the substrate usually have more energy compared to other PVD techniques. This results in a better adhesion of the films. It also causes more atom-mixing at the interface, meaning a less sharp interface between substrate and film. Furthermore shadowing parts from deposition by masks is less accurate. There are several different sputtering techniques. They differ in the localisation and way the ions or atoms are produced which impact at the target.

The simplest sputter deposition technique is DC-sputtering. A DC voltage between substrate and target of typically a few hundred volts is applied. This produces a plasma and a current flow. The positively charged ions of the plasma are accelerated onto the negatively charged target and sputter material to the substrate. This technique requires a conducting substrate and target. Alternatively a high frequency voltage can be used for sputtering insulators (RF-sputtering). Magnetron sputtering is the most important industrial sputtering deposition technique. A magnetic field is applied parallel to the target to elongate the distance travelled by the electrons between the target and the anode. This results in more collisions with gas atoms and a higher degree of ionisation of the plasma.

A different approach is to produce a plasma in a separate chamber (e.g. by microwave radiation) and then guide the plasma (High-target-utilization sputtering), ions (Ion-beam sputtering) or atoms (Atom-beam sputtering) to the target. It is also possible to add CVD features to a sputtering process in a process known as reactive sputtering. More informa-

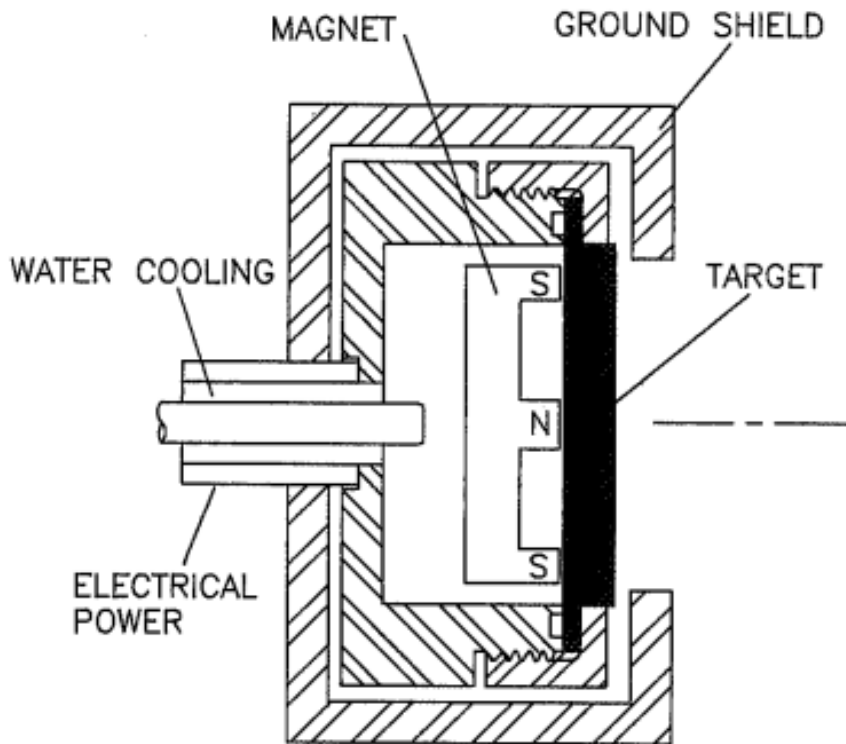


Figure 4.1: Cross sectional view of a planar magnetron sputter source [6].

tion on sputtering is given by Brodie and Muray [145].

4.4 Samples Studied of this Work

MBE Sample Preparation

Sample preparation was undertaken using a Eiko HDH-10000 Ultrahigh Vacuum (UHV) Molecular Beam Epitaxy (MBE) system. This system had a base pressure of 1.4×10^{-8} Pa. The system consists of a transfer chamber and a main chamber. The main chamber has a K-cell and 2 electron beam evaporation sources each with 5 exchangeable crucibles. Such PVD sources are described in section 4.1. Each source has its own quartz thickness monitor. The MBE system is also equipped with RHEED, a substrate heater, a substrate cooler and a masking system which can be used as a shutter. A description of such components can be found in section 4.2. The transfer chamber has a 1kW DC sputtering source. Sputtering is described in section 4.3.

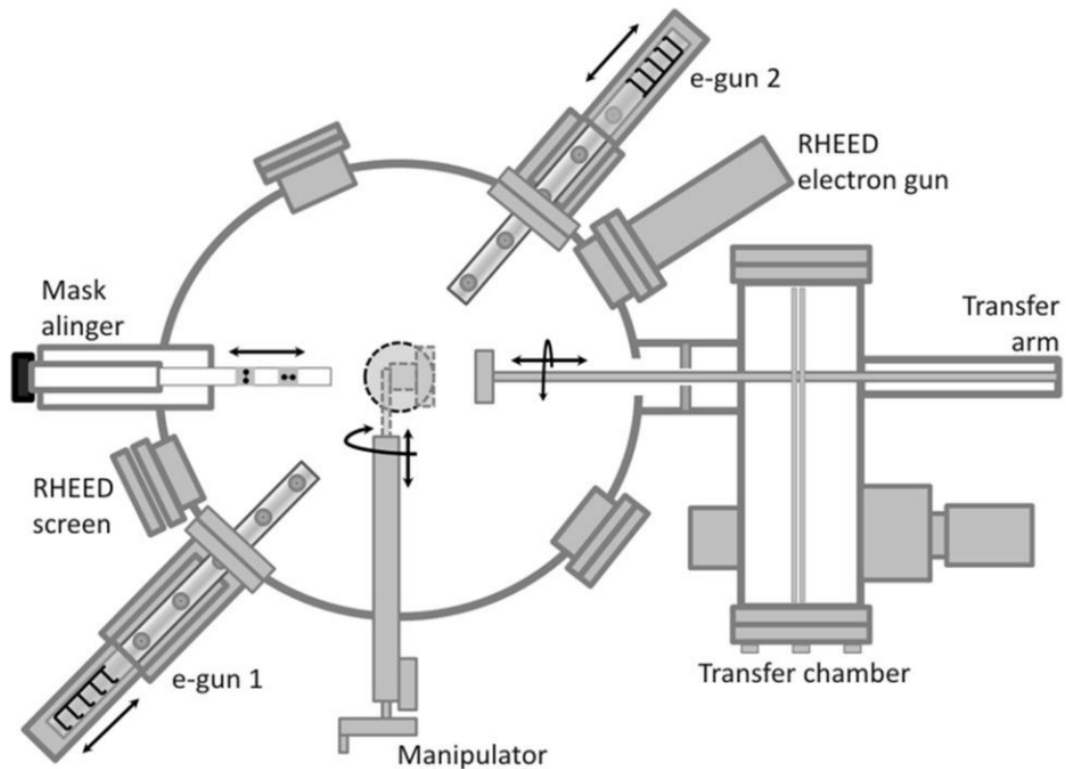


Figure 4.2: Eiko HDH-10000 Ultrahigh Vacuum (UHV) Molecular Beam Epitaxy (MBE) System [7]

Four MgO(001) substrates ($5\text{mm} \times 5\text{mm} \times 0.5\text{mm}$) were first cleaned in an ultrasonic bath with acetone and then rinsed with isopropanol (IPA) and blown dry with a nitrogen gun. They are then mounted onto a sample holder. The sample holder is put into the transfer chamber. The transfer chamber is pumped down to about 10^{-6} Pa. The sample holder is attached to a transfer arm. The connection between both chambers is opened and the sample holder is transferred into the main chamber using the transfer arm and heated for more than 1 hour at 688K for cleaning. Iron (Fe) and magnesium oxide (MgO) were co-evaporated at room temperature. Both sources, Fe and MgO, were evaporated by electron beam evaporation and the rates were individually monitored by the quartz thickness monitors. The Fe:MgO thickness ratios prepared were 1:1, 2:1, 3:1 and 4:1 with the parameters shown in Table 4.1. The samples were capped with 5 nm of gold (Au).

		Fe:MgO ratios			
		1:1	2:1	3:1	4:1
Equivalent thicknesses [nm] $\pm 10\%$	Fe	10.0	19.0	22.5	18.4
	MgO	10.0	9.5	7.5	4.6
Growth rate [nm/s] $\pm 10\%$	Fe	0.005	0.015	0.015	0.020
	MgO	0.005	0.007	0.005	0.005

Table 4.1: Coevaporation parameters for Fe:MgO sample preparations.

Further Preparation

The samples were ex-situ annealed at 673K for up to 6 h in 1 h steps under a vacuum of <0.01 Pa. The edges of the samples were not covered due to the shadow cast by the sample holder in the MBE system and a small amount of silver paint was used at the edges of the sample to make contacts for MR measurements.

4.5 Annealing

Annealing is a temperature treatment affecting the structure of materials. The temperature is below the melting point of a material. At high temperature atoms can move by diffusion to find atomic positions of lower energy. The effect is similar to the temperature effect on film growth described earlier in section 4.2. Annealing can reduce stress in the sample. This is achieved by reducing the amounts of defects. Grains boundaries can also be considered as defects and to reduce these the grains grow. Small grains have a larger ratio of atoms on the grain surface to those in the bulk, making small grains less stable than bigger grains. This results in a growth of bigger grains while smaller grains are absorbed. This restructuring process usually requires at least a temperature of 80% of the melting point in Kelvin. Below this temperature the atoms will stay roughly in the same position. Hence only small defects are removed. The annealing temperature was well below 80% of the melting temperature of Fe and MgO ensuring a reduced mobility of the atoms and preventing an intermixing of atoms of the film with the MgO substrate or with the protective Au capping layer. Bulk Fe under normal pressure has a phase change at 910° C from α -Fe (bcc) to γ -Fe (fcc). For Fe particles in MgO matrix this γ -Fe can form

already at lower temperatures and the phase can then still be found at room temperature after the annealing. Nagao *et al.* reports γ -Fe after 2h annealing at 500° C [146]. With 400 ° C the annealing was under that temperature and the ratio of Fe:MgO was much smaller 2:25 to 5:25 therefore no γ -Fe could be found in the TEM diffraction patterns. The temperature also influences how well atoms of one type can be absorbed by a crystal of another type. The higher the temperature the higher is the mobility of the atoms and defects. This leads to higher rates in generation and curing of defects and more atoms of a different material can be absorbed in a crystal. The cooling speed then determines whether the atoms segregate from the crystal. When cooling too quickly, the defects generated and different atoms lose their mobility before they can leave the crystal leading to stress. A slow cooling rate can lead to segregation of the different material atoms at the grain boundaries and core-shell like structures are formed.

The samples studied in this work were Fe:MgO and the segregation of MgO at the grain boundaries of the Fe was expected to lead to a high TMR but this effect was not observed. Higher temperatures and slower cooling speeds would probably have been necessary to achieve this segregation process. For a full account of annealing processes see [147].

Chapter 5

Measurement Systems

5.1 Vibrating Sample Magnetometer

A Vibrating Sample Magnetometer (VSM) measures the magnetisation of a sample by vibrating it in the vicinity of coils. A magnet moved with respect to a coil induces a voltage due to the changing magnetic flux through the coil and this voltage is measured. According to Foner [148] H. Plotkin described in 1951 a vibrating sample magnetometer for use with a solenoid, where the pickup coil is positioned coaxial to the magnetic field. Simon Foner published his version of a VSM in 1956 [148] and in more detail in 1959 [149]. In 1966 John Mallinson published a coil configuration optimised by 'the application of the Principle of Reciprocity' [8]. This is the coil configuration now called Mallinson-coils and is used in every modern VSM. Four identical pick-up coils are positioned coaxial to the magnetic field as shown in figure 5.1.

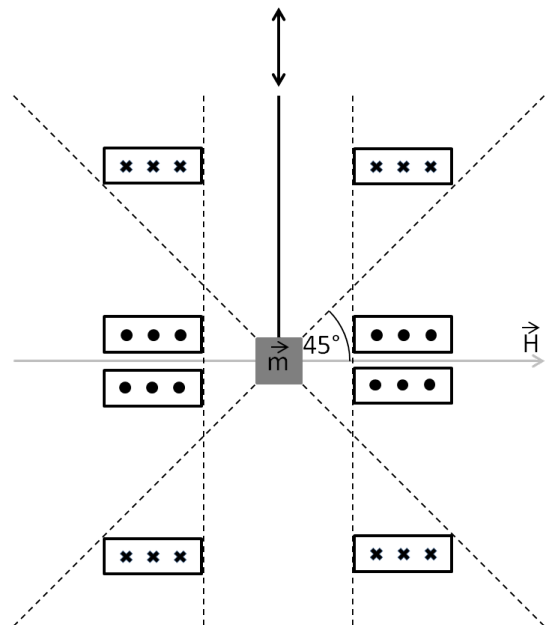


Figure 5.1: VSM coil arrangement according to Mallinson [8]

Four identical pick-up coils are positioned coaxial to the magnetic field as shown in figure 5.1.

The ADE Model 10 VSM uses 2 sets of Mallinson-coils to measure the magnetisation as a vector. The coils of the second set have perpendicular axes to the axes of the first set and also perpendicular to the direction of the sample vibration. The electromagnet which produces the external field can be rotated around the sample. The sample can be cooled with liquid nitrogen or heated up to 500° C.

A sample is mechanically vertically vibrated with a frequency of typically 81Hz, since this frequency has no harmonic frequency of 50Hz or 60Hz. The magnetic moment \vec{m} of the sample causes an alternating magnetic flux due to the movement of the sample. This moment can be intrinsic from a magnetic material or also be induced by an external horizontally applied magnetic field. The alternating magnetic flux induces into the pickup coils an alternating voltage. This voltage is measured using lock-in amplifier and is proportional to the magnetic moment of the sample. The vibration frequency and phase is triggering the lock-in amplifier. For the VSM used in this report this trigger signal is picked up by another set of coils. They measure the movement of a permanent magnet, which is attached to the same rod as the sample, but outside of the solenoid. The most common measurement mode is to measure the dependence of the magnetic moment on an external magnetic field.

The Gaussmeter of the VSM is calibrated comparing a measurement of this Gaussmeter with a measurement of a Bell Series 9900 Gaussmeter which is a secondary standard. A field standard is measured. This ensures that field strength during both measurements is identical. The magnetisation measurement is calibrated using a Palladium calibration sample of well defined susceptibility.

The sample was attached to a glass sample rod. The sample and sample rod were cleaned before and after each measurement in IPA using ultrasonic bath. The sample was attached to the sample rod using a small amount of vacuum grease and it was firmly held in this position with a wrapping of Teflon tape. Attention was paid to have the sample always in the middle between the coils when mounting the sample rod into the VSM. Fields of up to 20kOe were used to determine the saturation magnetisation of the samples. The step size of the M-H loops was 500Oe, since just the high field region is of interest for saturation magnetisation. At least 3 loops per sample were measured. The saturation magnetisation was then determined as described in section 5.5 on page 89.

5.2 Alternating Gradient Force Magnetometer

An Alternating Gradient Force Magnetometer (AGFM) is a measurement setup for magnetic properties. The susceptibility of a material causes a force in a non-uniform magnetic field. This force is proportional to the magnetization of the sample and by measuring this force of a sample, the magnetization can be determined. In a Faraday balance this force is measured using a force balance. In an AGFM a field gradient is produced by small 2 coils (gradient coils) opposing each other. When applying an alternating current to these coils, it results in an alternating field gradient and therefore in an alternating force. This alternating force

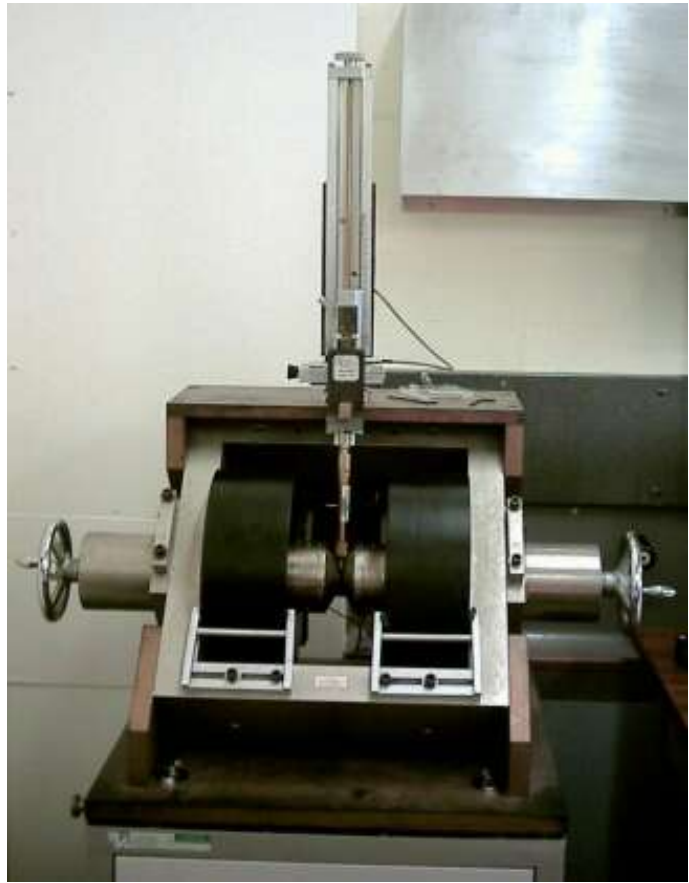


Figure 5.2: Princeton Measurement Micromag 2900 AGFM.

is measured by placing the sample on the free end of a cantilever rod and measuring the force with a piezoelectric sensor, which converts its bending moment into an electrical signal. The strongest signal is gained, when the alternating frequency is equal to the mechanical resonance frequency (typically between 100 Hz and 1000 Hz) of the cantilever. A lock-in amplifier is used to analyze the signal. To measure the dependence of the magnetization of a sample on an external magnetic field, the gradient coils are attached at the pole pieces of an electromagnet.

The quality factor Q of the cantilever can reach over 100. For the measurements reported here it was usually between 10 and 20. Quality factors >10 are sufficient for reproducible measurements. Another important criteria of reproducible measurements is

the calibration. The calibration must be done with a sample of similar shape and magnetic moment. 'This is necessary to minimize errors due to amplifier non-linearity and the magnitude of the field gradient away from the centre of symmetry of the gradient coils' [11]. As a calibration standard a Ni calibration sample with a saturation magnetization of 5.96 memu was attached to a MgO substrate by a very small amount of vacuum grease in the same way as the samples are attached to the cantilever. The mass and size of the calibration sample was much smaller than the mass and size of the MgO substrate. This resulted in an inaccurate calibration. A Palladium calibration sample (weight (72.721 ± 0.006) mg) and the comparison with VSM measurements made it possible to estimate the factor of the miscalibration and recalibrate it. Palladium is a Pauli paramagnet with a specific susceptibility of $5.3317 \frac{\mu\text{emu}}{\text{g}\cdot\text{Oe}}$ [62]. This means it has a linear response to an external magnetic field. By adjusting the external field the magnetization is set to a value of comparable to the range of calibration.

The saturation magnetization values of the samples investigated were in the range of less than 100 μemu up to 1 memu. Hysteresis loops were measured and corrected for the diamagnetic offset, by assuming, that the samples were saturated at 70% of the maximum applied field of 10 kOe. This is a built in function of the AGFM measurement program. The slope correction value itself can also give useful information about diamagnetic and paramagnetic components of a material. The diamagnetic moment of the sample holder will also be removed.

For the AGFM measurements a 'Princeton Measurement Micromag 2900' was used. The field gradient in this AGFM can be up to $4 \frac{\text{Oe}}{\text{mm}}$ for a gradient setting of 1 and $0.4 \frac{\text{Oe}}{\text{mm}}$ for a setting of 0.1. Considering a sample of $5 \text{ mm} \times 5 \text{ mm}$ and a gradient of $4 \frac{\text{Oe}}{\text{mm}}$, the magnetic field is 10 Oe higher at the edge than it is in the centre of the sample, causing ≈ 10 Oe inaccuracy when determining for example the coercivity. The smaller the field gradient and the smaller the sample, the more accurate is the total field H at the sample. However the signal is also smaller and therefore the measurement of the magnetization M is less accurate. When measuring M-H curves using the AGFM the choice of the gradient is a trade-off between determining M accurately and having a well defined H field at the sample.

The stiffness of the legs of an AGFM-probe depends on the temperature. It influences

therefore the resonant frequency, quality factor and calibration. The resonant frequency, quality factor and calibration can also be affected by different masses due to the amount of vacuum grease used or slightly different sample sizes. This makes it difficult to determine accurate absolute values of M and even more difficult to make temperature dependent M measurements. The AGFM is therefore usually used to measure normalized curves where M is always shown as a fraction of the saturation magnetisation M_S . For this task the AGFM is much faster than a VSM with greater accuracy. The VSM can make reliable measurements of absolute M at different temperatures.

5.3 Magnetoresistance Studies

The Magnetoresistance (MR) setups described here have in common that they are all controlled by LabView programs. The computer uses a multifunctional Data Acquisition (DAQ) PCI card (NI PCI-6010) to control the current delivered by the power supply. It also controls the switch for reversing the polarity of the current and ac-

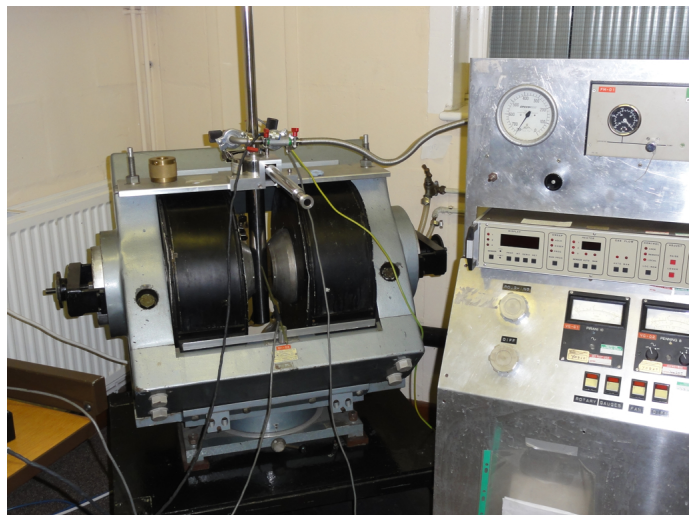


Figure 5.3: Purpose-built MR prober.

quires a field measurement from the Gaussmeter. The Hall probe is as close as possible to the sample, but outside of the cryostat. The sample sits on top of a sample rod and is contacted by 4 spring loaded tips. The resistance is measured in a standard 4-point-probe setup. The sample rod is inside a cryostat. The cryostat can be evacuated, by a rotary pump and a diffusion pump, and cooled down by liquid Nitrogen or Helium. The temperature is controlled by an Oxford Instrument Intelligent Temperature Controller (ITC 4).

Calibrating the MR setup

The cryostat was taken out of the electro-magnet and a hall probe was placed at the position of the sample. The hall probe is part of the secondary standard, a F.W.Bell Series 9900 Gaussmeter. A Lab view program, based on the original MR program,

was written, but instead of measuring the resistance, it measured the secondary stan-

Figure 5.4: Block diagram of calibration setup.

Figure 5.4 is a block diagram of the calibration setup. It shows a central coil with a red vertical line through its center. To the left of the coil are four stacked boxes: 'Computer/LabView', 'Power Supply', 'Polarity Switch', and 'Gauss Meter'. To the right of the coil is a box labeled 'F.W.Bell Series 9900 Gaussmeter'. Blue arrows indicate the control signal path: from 'Computer/LabView' to 'Power Supply', 'Polarity Switch', and 'Gauss Meter'; from 'Power Supply' to the coil; and from 'Polarity Switch' to the coil. A red arrow indicates the measurement path: from the coil to the 'Gauss Meter', and from the 'F.W.Bell Series 9900 Gaussmeter' to the 'Computer/LabView'.

standard and produces a file with the information about the applied control voltage at the power supply, measured voltage from the normal Gaussmeter and the measurement of the secondary standard. The block diagram of this setup is shown in figure 5.4. Several loops with different amount of measurement points and different field settling times were done resulting in different ramp rates. The Gaussmeter voltages were fitted linearly against the secondary standard measurements. A cubic like deviation from linearity was found as shown in figure 5.5 (b). A third degree polynomial fit was used as shown in figure 5.5 (a). This measurement was that with the lowest ramp rate. It had 12004 measurement points and 4s settling time for each point resulting in a ramp rate of about 0.3 G/s. The deviation from this fit appears to be random as shown in figure 5.5 (c). The need to fit with a third degree polynomial may be attributed to the Gaussmeter probe sitting outside of the centre of symmetry of the field, while the probe of the secondary standard sits at the centre. If the field ramp rate was too high and the field settling time too low, the deviation from the fit showed offsets. These offsets have their origin in the different integration times used by the Gaussmeters. For increasing (decreasing) fields the Bell Gaussmeter shows a lower (higher) field value than the other Gaussmeter, meaning that the integration time of the Bell Gaussmeter is longer. This offset is linear with the ramp rate as shown in figure 5.6 for field settling times smaller than or equal to 1s.

DC-MR setup

The MR setup is controlled by a LabView program. The program is based on the program of a previous PhD student [1], but most parts have been rewritten by me. The major

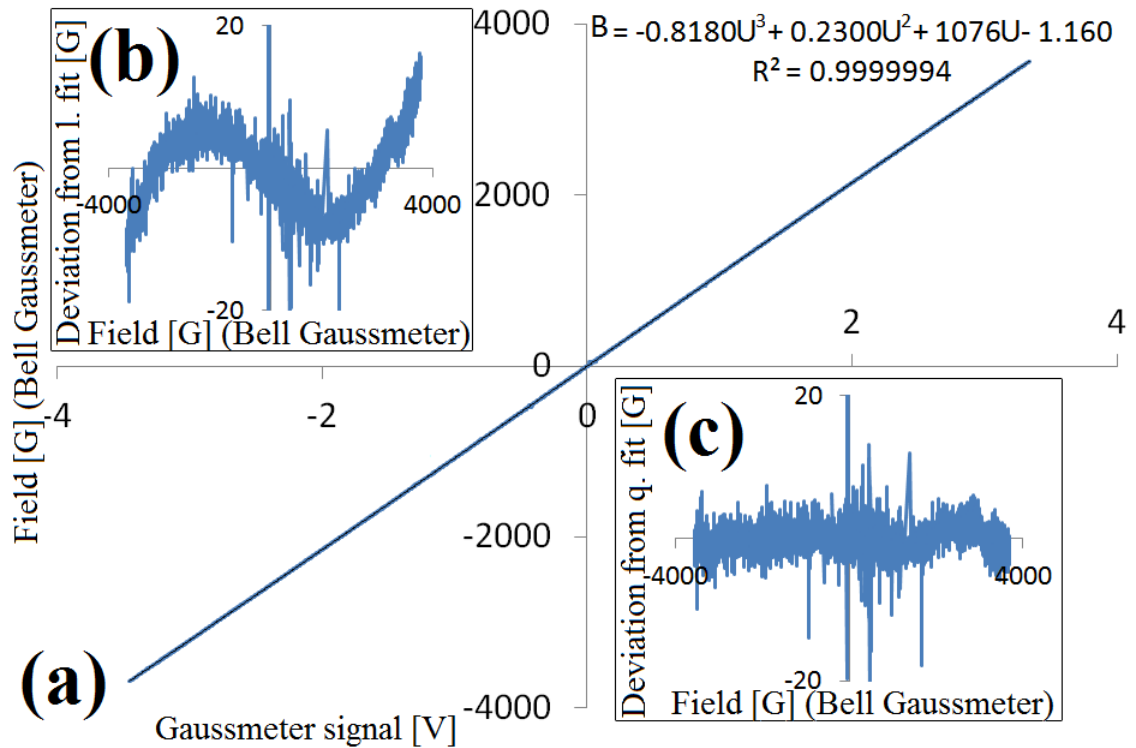


Figure 5.5: Most precise Gaussmeter Calibration measurement with a ramp rate of 0.3 G/s. (a) Measured Voltage of the Gaussmeter vs. Measured field with the F.W.Bell Series 9900 Gaussmeter and third degree polynomial fit. (b) Deviation from linearity. This means the y-Axis shows the measured value of the F.W.Bell Series 9900 Gaussmeter minus value predicted by a linear fit.(c) Deviation from third degree polynomial fit.

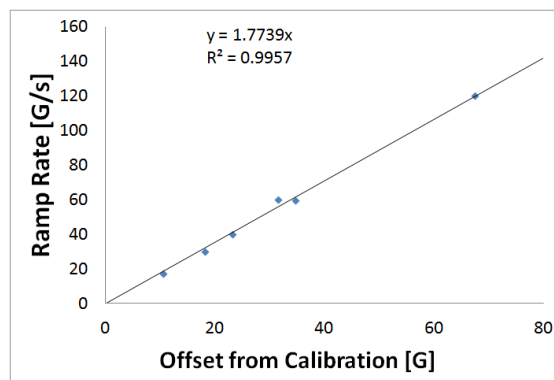


Figure 5.6: Offset due to slower integration times of F.W.Bell Series 9900 Gaussmeter compared with the P.S.U. Magnetometer.

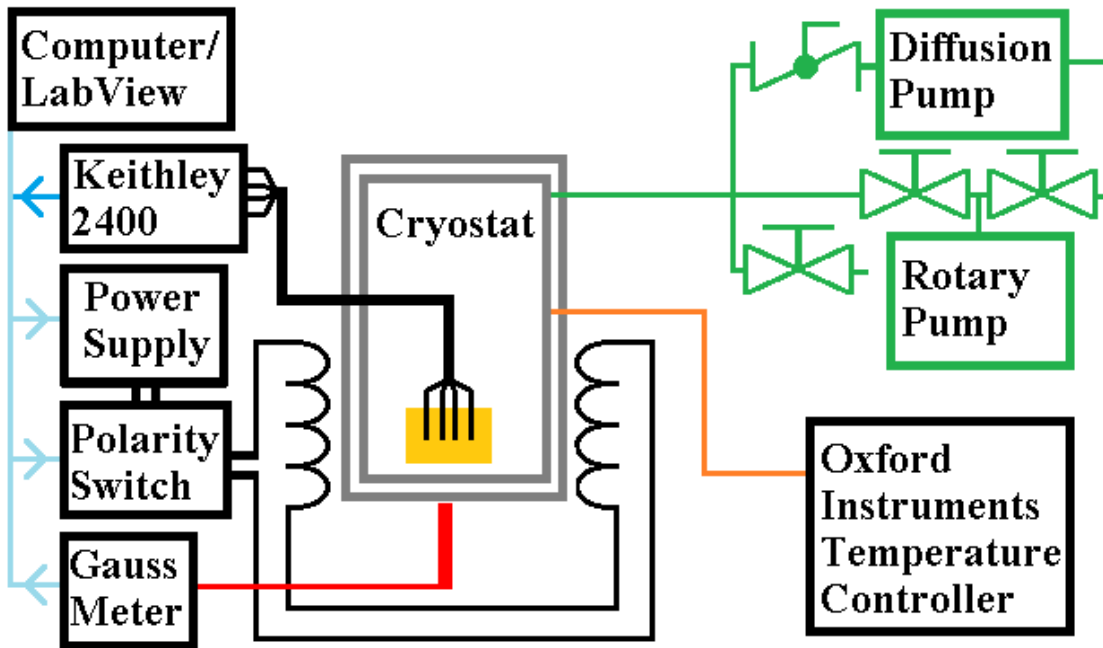


Figure 5.7: DC-MR setup.

improvement was to exchange the stabilized current source, where the current had to be set manually, and the Keithley 2000, which measured the voltage, by a Keithley 2400, setting current and measuring the voltage and the current at the same time. The program now has a number of new features:

- Time stamps for each single measurement.
- Making several loops sequentially.
- Offset compensation can be used: Offset compensated measurements avoid problems resulting e.g. from thermal electromotive forces in the setup.
- Alternating mode can be turned on: A constant current is applied and a measurement is done, then the polarity is switched and a second measurement is done and then the average of both measurements is calculated. This can remove offset voltages e.g. due to static charging of the sample.
- Adjustable integration time and averaging over up to 100 measurements. A single measurement can then take between 0.1s and a few minutes. This is a trade off between fast and accurate measurements.
- Adjustable field settling time.

- Field steps can be varied during a measurement. If a second field step is given the program varies the field step so that smaller field steps are made at lower fields. This enables a higher resolution for lower fields in the region where the magnetization of the sample switches and the high field region is still observable. The disadvantage of this mode is that the ramp rate is not constant. Due to thermal energy the magnetic properties always change with time so they depend on the ramp rate and a variable ramp rate can make it difficult to compare a measurement with other measurements. If the second field step is set to 0 or is equal to the first field step, this function is not activated and a constant field ramp rate results.
- An automatic protocol file is created containing all the settings made in the program and for each loop the file name of the measurement, the start and stop times and dates, maximum magnetoresistance MR_{max} [%] and minimum resistance R_{min} [Ohm] values are recorded.
- A protocol file can be used and the program automatically outputs another protocol file where the measurements are sorted by MR_{max} from small to big and also a file with all measurements and settings is created. This file can be opened in EXCEL and a Macro makes a graph for each measurement and averages over all measurements and shows a graph. After the MR program analyzed a protocol file the distribution of the MR_{max} values is shown. This way it is easy to throw out inaccurate measurements where the maximum MR value differs significantly from the other measurements. This is done by manually deleting the first and/or last few entries in the new protocol file and then running the analysis again with the protocol file.
- 2 probe/4 probe resistance switch.

A number of significant improvements have been made:

- The accuracy of the numbers in the measurement file is now equal to the accuracy of the Keithley 2400 delivers.
- Small field steps no longer crash the program.
- Field steps are more accurate.

- The MR value is calculated by dividing the resistance by the minimum resistance of a whole loop.
- Two measurements of the magnetic field are performed: One before and one after the resistance measurement.
- Any cessation of the program now turns off the magnet power supply and the current through the sample.
- The measured resistance values are not shown in arbitrary units.
- Corrected and enhanced the Gaussmeter calibration.

A step-by-step instruction was written for using the MR setup and a EXCEL macro in Visual Basics for Application (VBA) to average over as many measurements as required. An example of the data is shown in figure 5.8.

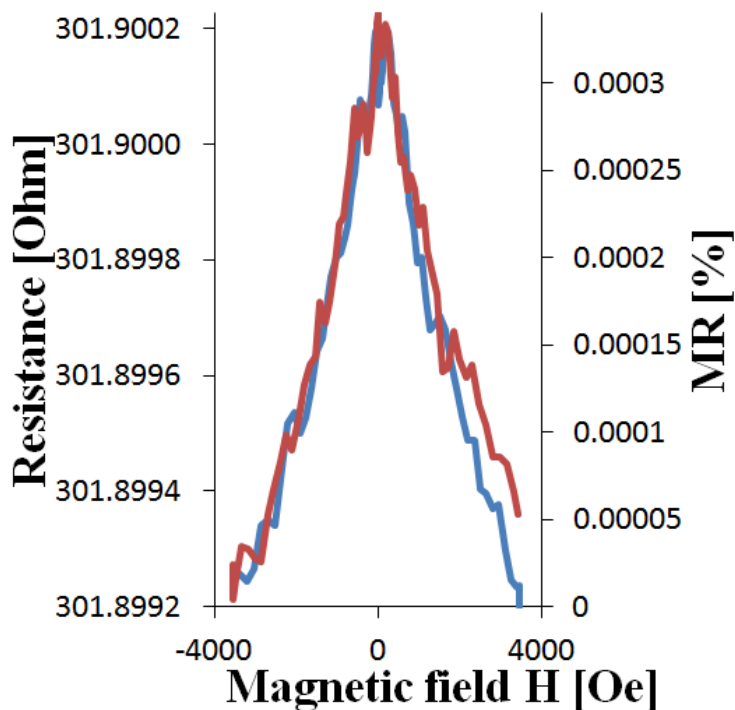


Figure 5.8: An MR measurement at highest resolution.

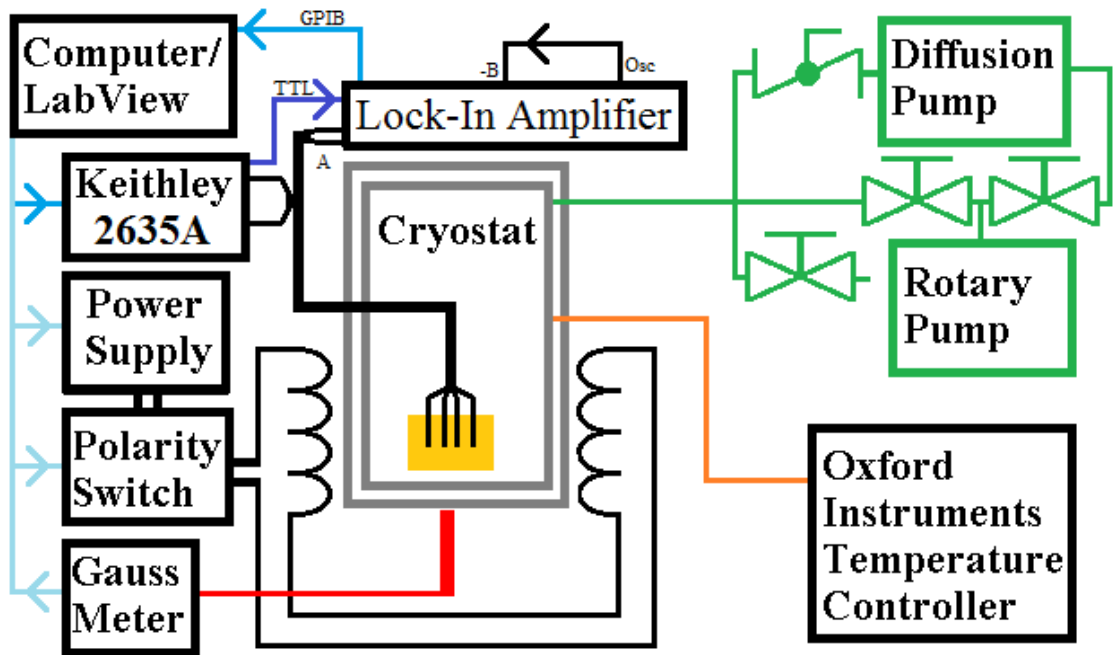


Figure 5.9: AC-MR setup.

AC-MR setup

A setup using alternating current was implemented. As an alternating current source a Keithley 2635A was programmed to deliver a sinusoidal current. The voltage was measured by a Lock In Amplifier with Digital Signal Processing (DSP) and the reference phase was delivered from the Keithley 2635A by its Digital I/O interface to the TTL input of the Lock in Amplifier. A further improvement was tried by subtracting a sinusoidal signal from the measured signal using a signal from the internal oscillator of the Lock-In Amplifier and fed into the -B channel of the Lock-In Amplifier. For each measurement the amplitude was adjusted iteratively to minimize the in-phase signal. This amplitude adjustment together with the in-phase signal is then the measured voltage signal. Unfortunately the setup has 2 major flaws causing the accuracy to be much lower than the DC setup:

Firstly the measurement accuracy of the Lock-In Amplifier is limited by the accuracy of the D to A and A to D converters of the Lock-In amplifier. The Lock-In Amplifier samples the signal to 5 significant figures. This limits the measurement of voltage changes to a minimum of 0.001 % . In reality it was 0.05 % voltage changes that could be resolved. The accuracy of the amplitude of the oscillator has the same limit of 5 significant figures.

That may further reduce the voltage changes that can be measured, if the signal from the sample is of the same shape as the signal of the oscillator.

Secondly the signal produced by the Keithley 2635A is not a perfect sinusoid. The Keithley 2635A runs programs in a language called lua. The program was transmitted to the Keithley 2635A via Lab View and the GPIB interface. The code written is executed line by line and command by command. Each single command needs its own execution time and this time differs depending on the command. The program sets the current to different values one after another and this results in a sinusoidal-like alternating current. The time needed to change the current between different values depends on whether both values have the same sign. Also a command is needed to set the digital output channel to 1 or 0. When the maximum is reached, the digital channel is set to 1 and when the minimum of the sin curve is reached the signal is set to 0. The waiting time at these points does not disturb the sin shape much since the signal has the smallest slope at these points. The waiting time to switch from positive to negative or negative to positive on the other hand disturbs the signal significantly due to being at the highest slope of sin signal when measuring the subtracted signal with an oscilloscope.

It is possible to improve the signal shape by adding waiting time commands between each command. These commands themselves require execution times. In order to make a good sinusoidal signal one needs waiting commands of precisely defined length between each current step. Furthermore the number of steps which are needed to define the sinusoidal signal is important for the quality of the signal shape. The more points per period used the more accurate is the shape of the waveform. However the more points per period used restricts the frequency, that can be obtained. Also with a lower frequency it takes longer to integrate the signal accurately using the Lock-In Amplifier. This results in a trade-off between accuracy and measurement speed. Hence the measurement takes longer than a DC measurement and is less accurate.

5.4 Area measurement using optical Microscope

In order to compare the saturation magnetization of the Fe in the film with the bulk value it is necessary to determine the area of the film precisely. The the samples did not have exactly the same shape and differ from one to another by up to 0.1mm. Also the edges are sometimes rough and there are areas without a film due to the shadow cast by the sample holder during the evaporation. Since two sources were used for evaporation and these sources were at slightly different angels, there are also areas of half shadow. By EDX it was determined that the image seen in the optical microscope had brighter areas of Fe capped with the Au film, while the less bright areas are just the MgO film.

12 pictures per sample of the surface were made with a CCD camera on an optical microscope using the lowest possible magnification. These pictures were combined using MosaicJ software. This ImageJ plug-in provides a 'user-friendly, semi-automated assembly of accurate image mosaics in microscopy' [150]. For reference purpose the length and width of the sample were measured using a vernier calliper with an accuracy of 0.05mm. In the merged image in pixels this results in a scale of $(0.91 \pm 0.01) \frac{\mu m}{px}$ or calculated as an area constant $(0.85 \pm 0.02) \frac{\mu m^2}{px}$. Finally the area covered with Fe could be measured with the standard polygon selection function in ImageJ.

5.5 Measurement of the Saturation Magnetisation

In the M-H curve of a magnet the saturation of the magnetisation is often not completely achieved, since at finite temperature and finite field a few spins are generally not aligned. In order to determine the saturation magnetisation from such a curve a diagram with magnetisation against inverse magnetic field $\frac{1}{H}$ is drawn and the curve is linearly extrapolated back to the y axis. The point of intersection is the saturation magnetisation for an infinite magnetic field and therefore the saturation magnetisation. For the samples measured in this work there is a diamagnetic contribution from the sample holder as well as from the MgO substrate superimposed on the measurement of the M-H curve. This gives a moment proportional to the magnetic field. In the diagram with magnetisation against inverse magnetic field this causes the curve to go to infinity when approaching 0 render-

ing this method useless. The diamagnetic slope must be subtracted from the M-H curve before applying this method. Measuring a sample holder without a sample is one way to determine the diamagnetic contribution. The diamagnetism of the substrate MgO can be found in the literature [62]. Small size differences in the MgO substrates as well as the unknown diamagnetic contribution of the sample holder makes this method inaccurate. For AGFM measurements the determination of the sample holders diamagnetism is also difficult since the resonance frequency with and without sample is fundamentally different and the signal is weak making it difficult to find the resonance frequency.

For all measurements performed, with exception of the as deposited Fe:MgO=1:1 sample, the M-H curve is a straight line at fields higher than 7kOe. The slope of this line is the diamagnetic slope and can be semi-automatically subtracted from the M-H curve. The calculation assumes that saturation magnetisation would be reached at 7kOe. After subtracting the slope, the M-H curve is a horizontal line for magnetic fields higher than 7kOe and the value at this point is taken as the saturation magnetisation. An example of this method of determination of M_S is shown in figure 5.10.

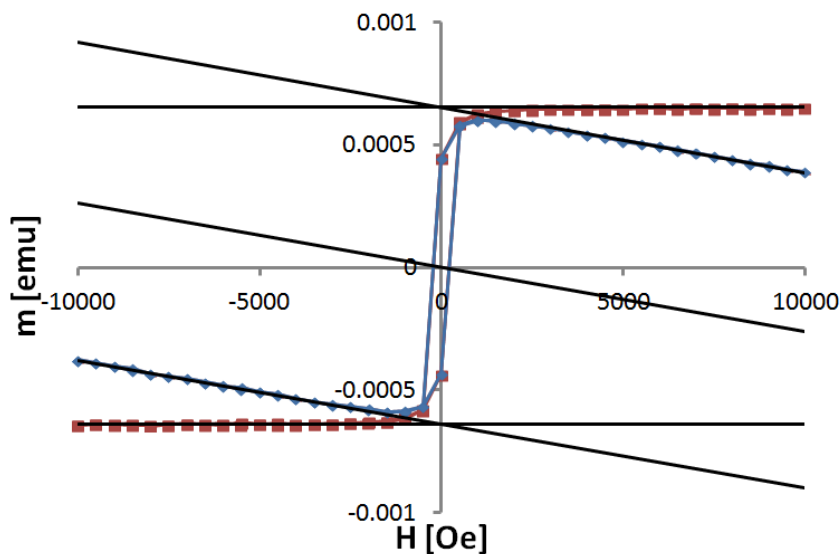


Figure 5.10: m - H curve measured using VSM with and without slope correction.

Chapter 6

Experimental Results

6.1 Magnetization Processes

6.1.1 Properties of the As-deposited Films

The M-H loops of all as deposited samples show uniaxial anisotropy as shown in figure 6.1. For all samples the magnetization saturates at higher fields with higher Fe concentration. In particular for the sample with a ratio of Fe:MgO = 1:1 a field of approximately 10kOe is needed to completely saturate the sample. The M-H curve and the low squareness M_r/M_s of this sample suggests that there might be a significant fraction of superparamagnetic grains. This cannot be confirmed absolutely without superimposition of H/T data [151]. There might also be smaller fractions of superparamagnetic grains in the samples with higher Iron concentration but their contribution to the shape of the curve is not significant.

The coercivity for the hard axis increases with an increasing concentration of MgO in the samples. In particular the coercivity for the Fe:MgO = 1:1 sample is much higher compared to the other samples. The increase in coercivity with the concentration of MgO in the sample might be attributed to an increased number of pinning sites and/or to an increase in the pinning strength of each site. The easy axis coercivity also seems to increase with increasing concentration of MgO in the samples. However the easy axis

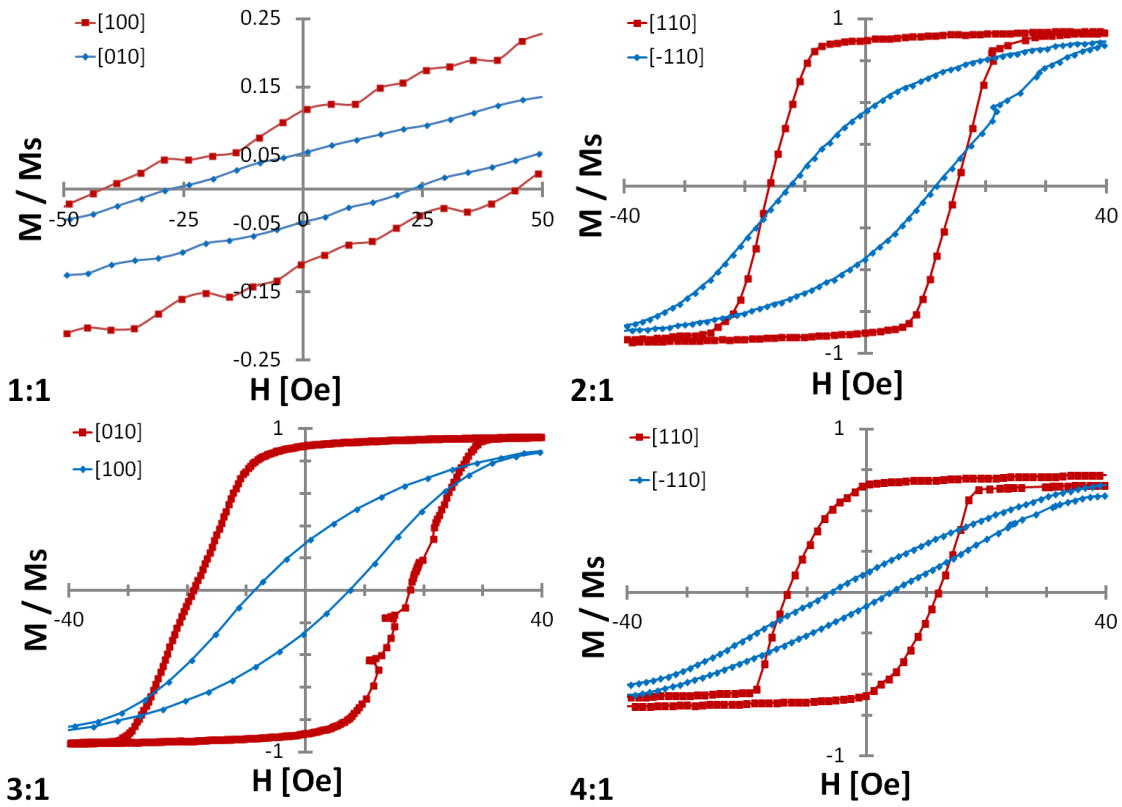


Figure 6.1: As deposited samples of different compositions with easy and hard axis.

of the Fe:MgO = 3:1 has a higher coercivity than Fe:MgO = 2:1. The Fe:MgO = 3:1 sample is also the sample with the highest average moment per Fe atom resulting in the high saturation magnetization shown in table 6.1. Also the hysteresis loop of its hard axis exhibits the highest squareness of all as-deposited samples. The saturation magnetization was calculated by dividing the measured moment by the nominal Fe volume. A detailed error analysis showed that the values were accurate to 12% dominated by the error in the film thickness monitor.

Sample	M_s [emu/cm ³]	e.a. H_c [Oe]	h.a. H_c [Oe]	e.a. M_r/M_s	e.a. H_n [Oe]	e.a. $\frac{dM}{dH} _{H_c}$ [$\frac{10^{-3}}{Oe}$]
	$\pm 12\%$	± 2	± 2	± 0.01	± 5	$\pm 5 \%$
1:1	1165	42	26	0.11	N/A	3.2
2:1	974	16	12	0.87	-10	140
3:1	1786	18	8	0.89	-7	92
4:1	1660	13	5	0.68	36	95

Table 6.1: Parameters of magnetization curves for as-deposited samples.

The easy axis of the samples with Fe:MgO =2:1 or larger show a high squareness M_r/M_s and low coercivity which indicates exchange coupling [37], whereas the Fe:MgO = 1:1 sample shows exchange decoupled behaviour. The samples with Fe:MgO = 2:1 or larger have intergranular exchange coupling which is comparable to the anisotropy which results in the observed high squareness of the easy axis loops. For the Fe:MgO = 2:1 sample the domains start to nucleate after the field direction is reversed at approximately -10 Oe. For the Fe:MgO = 3:1 sample the domains starts to nucleate earlier at approximately -7 Oe and for the Fe:MgO = 4:1 sample, the nucleation of the domain wall starts at approximately 36 Oe before the field direction is reversed. This might be attributed to the higher demagnetization field of the sample due to its higher Fe concentration. The Fe:MgO = 2:1 sample shows the highest slope at the coercivity $\frac{dM(H)}{dH}_{H=H_c}$ which means that after the nucleation of the domain wall it moves fastest in this sample whereas the slope in the Fe:MgO = 3:1 and Fe:MgO = 4:1 is approximately identical. The reversal of the Fe:MgO = 1:1 is not domain wall driven but dominated by rotation of the magnetization within the grains. This results in a very low value of the slope of the loop.

6.1.2 Effects of Annealing in Zero Field

Just the Fe:MgO=1:1 was annealed in zero field. The saturation magnetization decreases by about one third for each hour of additional annealing at 400 ° C as shown in table 6.2. The decrease of the saturation magnetization might be attributed to oxidation of the Fe. The annealed samples saturate more easily at approximately 7kOe. The coercivity increases dramatically for 1h annealing and then decreases on further annealing. The initial increase is probably attributed to the increase in the anisotropy of the grains, while the decrease for further annealing might be attributed to the oxidation of the grains at the grain boundaries. The squareness of the loops also initially increases strongly after 1h annealing and the difference between the easy and hard axis becomes small. For further annealing the squareness decreases. The slope at coercivity after 1h annealing is unchanged for the easy axis and increased for the hard axis. Further annealing reduces the value of the slope for both axes to approximately 0.002 Oe^{-1} .

Sample	M_s [emu/cm ³]	e.a. H_c [Oe]	h.a. H_c [Oe]	e.a. M_r/M_s	e.a. $\frac{dM}{dH} _{H_c}$ [$\frac{10^{-3}}{Oe}$]	e.a. S^*
	$\pm 12\%$	± 2	± 2	± 0.01	$\pm 5\%$	± 0.05
0h	1165	42	26	0.11	3.2	0.18
1h	810	225	234	0.51	3.2	0.29
2h	517	63	59	0.12	1.9	0.00
3h	412	58	55	0.11	2.0	0.05

Table 6.2: Fe:MgO=1:1 sample after different annealing times in zero field.

6.1.3 Effects of Field Annealing

Table 6.3 shows the key parameters for the Fe:MgO = 1:1 samples after field annealing for various times. Unfortunately the sample annealed for 1 hour seem to have suffered significant oxidation and no reliable data could be obtained. The saturation magnetization is much lower and the easy and hard axis are approximately identical. In the 2h annealed sample the saturation magnetization reaches approximately the bulk value of the Iron which is then reduced by further annealing. The hysteresis loop shows a strong anisotropy after 2h annealing which is also reduced by further annealing. The slope of the loop at the coercivity is also highest for the 2h annealed sample and is then reduced by further annealing. The coercivity increases with the annealing time. These changes indicate an increase of the anisotropy of the grains.

Sample	M_s [emu/cm ³]	e.a. H_c [Oe]	h.a. H_c [Oe]	e.a. M_r/M_s	e.a. $\frac{dM}{dH} _{H_c}$ [$\frac{10^{-3}}{Oe}$]	e.a. S^*
	$\pm 12\%$	± 2	± 2	± 0.01	$\pm 5\%$	± 0.05
0h	1165	42	26	0.11	3.2	0.18
2h	1691	99	44	0.71	17	0.57
3h	1064	152	121	0.64	7.9	0.47

Table 6.3: Fe:MgO=1:1 sample after different annealing times in ≈ 70 Oe field.

Table 6.4 shows the values of the field annealed samples with a ratio Fe:MgO=2:1. The saturation magnetization and the easy axis squareness rise with the annealing time and reach almost the bulk value of Fe after 4h annealing. This might be attributed to additional contribution to the saturation magnetization by Fe atoms which were paramagnetic before annealing and therefore were just decreasing the diamagnetic slope correction of the MgO. The diamagnetic slope correction for the as deposited sample is $8 \pm 1 \frac{nm\mu}{Oe}$. The

theoretical slope correction for a $5\text{mm} \times 5\text{mm} \times 0.5\text{mm}$ cuboid of MgO is $11.3 \frac{\text{emu}}{\text{Oe}}$. The slope correction value increases with annealing time. The magnetization values then drop for further annealing probably due to oxidation. The hard axis squareness decreases with annealing time and increases for annealing of more than 4h. So the field-annealing increases the anisotropy. The easy (hard) axis coercivity reaches a maximum (minimum) after 3h annealing. For annealing longer than 4h the coercivity then rises dramatically for hard and easy axes. This might be attributed to areas of oxidation acting as pinning sites. The coercivity squareness of the easy (hard) axis reaches a maximum (minimum) after 3h annealing.

Sample	$M_s [\frac{\text{emu}}{\text{cm}^3}]$	e.a. H_c [Oe]	h.a. H_c [Oe]	e.a. M_r/M_s	e.a. $\frac{dM}{dH} _{H_c} [\frac{10^{-3}}{\text{Oe}}]$	e.a. S^*
	$\pm 12\%$	± 2	± 2	± 0.01	$\pm 5\%$	± 0.05
0h	974	16	12	0.87	140	0.61
1h	1365	83	26	0.90	37	0.70
2h	1162	92	10	0.95	43	0.76
3h	1411	69	10	0.996	121	0.88
4h	1502	72	15	0.97	99	0.86
5h (2h+3h)	640	145	121	0.65	30	0.85
5h (1h+4h)	452	140	128	0.68	9.1	0.46

Table 6.4: Fe:MgO=2:1 sample after different annealing times in ≈ 70 Oe field.

Table 6.5 shows the values of the field annealed samples with a ratio Fe:MgO=3:1. The saturation magnetization shows a significant increase in the magnetic moment per Fe atom compared to bulk Fe. This increase is probably due to the Fe MgO surfaces. Such an increase was predicted by Li and Freeman [65] and observed for Fe particles in an MgO matrix by Matsuo *et al.* [66]. The easy axis direction differs from the samples with other compositions and is not completely aligned to a simple crystalline axis, but slightly off from the [010] axis. The easy axis coercivity and coercivity squareness are largest for 3h annealing and lowest for the as deposited sample. The slope at coercivity for the easy axis is largest after 4h annealing. The nucleation field for the easy axis is -15 Oe after 1h annealing, -29 Oe after 2h annealing -27 Oe after 3h annealing and -26 Oe after 4h annealing, so there seem to be a saturation in the nucleation field after 2h.

Table 6.6 shows the values of the field annealed samples with a ratio Fe:MgO=4:1. Unfortunately the 1h annealed sample broke in two major fragments and some smaller

Sample	M_s [emu/cm ³]	e.a. H_c [Oe]	h.a. H_c [Oe]	e.a. M_r/M_s	e.a. $\frac{dM}{dH} _{H_c}$ [$\frac{10^{-3}}{Oe}$]	e.a. S^*
	$\pm 12\%$	± 2	± 2	± 0.01	$\pm 5\%$	± 0.05
0h	1786	18	8	0.89	92	0.46
1h	2090	29	44	0.94	69	0.53
2h	1887	30	49	0.92	109	0.72
3h	1744	47	71	0.85	86	0.79
4h	1957	38	67	0.87	149	0.85
5h	1843	43	79	0.93	72	0.70

Table 6.5: Fe:MgO=3:1 sample after different annealing times in ≈ 70 Oe field.

during the MR measurement. This seem to have also damaged the Fe:MgO film: The calculated saturation magnetization of the largest fragment is 170 emu/cm³ indicating that most of the film was lost, when the sample broke. No reliable results could be obtained from the fragments.

Annealing seems to increase the coercivity, easy axis squareness and slope at coercivity. However there seem to be some random difference between the samples. However the samples were annealed sequentially. For example the as deposited sample was annealed for 4h and that annealed for 3h was reannealed for 3 hours to give the 5hour sample. The samples are labelled with superscript to indicate which are the same material. The inherent properties of the samples seem to have a greater influence on the magnetic properties than the annealing time and explains the seemingly random rise and fall of the properties with the annealing time. The 0h sample has a much higher calculated saturation magnetization then the 2h and 3h samples. Due to the annealing the saturation magnetization slightly changes for the samples: from 1660 emu/cm³ to 1671 emu/cm³ for the as deposited sample, from 1041 emu/cm³ to 1161 emu/cm³ for the 2h annealed sample and from 1283 emu/cm³ to 1223 emu/cm³ for the 3h annealed sample. The easy axis coercivity increases due to the annealing: from 13 Oe to 54 Oe for the as deposited sample, from 90 Oe to 99 Oe for the 2h annealed sample and from 92 Oe to 105 Oe for the 3h annealed sample. The as deposited sample had the highest increase in coercivity, which fits well to the increase in coercivity of the as deposited samples of other compositions, but after 4h annealing the coercivity is lower than the 3h annealed sample. This can be explained by the much higher saturation magnetization of the sample which causes a stronger external demagnetization field. The squareness of the loops develops through annealing from

0.64 to 0.78 for the as deposited sample, from 0.91 to 0.90 for the 2h annealed sample and from 0.79 to 0.83 for the 3h annealed sample. Again the strongest increase is observed for the as deposited sample, a strong increase for the as deposited samples is also observed at samples of other compositions. However the squareness after reannealing the 2h annealed and 3h annealed samples changes not much, while the differences between these samples are larger. Similar comparisons can be also made for the hard axis coercivity and the slope at the coercivity. This might be attributed to concentration differences between the samples, despite being produced together and indicates a non-uniform stream profile of the sources in the MBE system.

Sample	M_s [emu/cm ³]	e.a. H_c [Oe]	h.a. H_c [Oe]	e.a. M_r/M_s	e.a. $\frac{dM}{dH} _{H_c}$ [$\frac{10^{-3}}{Oe}$]	e.a. S^*
	$\pm 12\%$	± 2	± 2	± 0.01	$\pm 5\%$	± 0.05
^a 0h	1660	13	5	0.64	95	0.48
^b 2h	1041	90	23	0.91	145	0.93
^c 3h	1283	92	30	0.79	123	0.93
^a 4h	1671	54	25	0.78	114	0.87
^b 5h	1161	99	28	0.90	145	0.94
^c 6h	1223	105	26	0.83	127	0.94

Table 6.6: Fe:MgO=4:1 sample after different annealing times in ≈ 70 Oe field.

The data in tables 6.3 to 6.6 shows the difficulty of annealing samples to a high degree of uniformity and reproducibility. For example a general trend of increasing coercivity with annealing is observed for all samples. However the increase is not monotonic. Such an increase is expected due to grain growth. However the coercivity is a balance of reversible and irreversible effects [152]. The true switching behaviour is revealed by the remanent coercivity H_r which is the median switching field of the blocked particles.

6.1.4 Remanence Curves

DCD and IRM curves were measured using the AGFM using carefully calibrated field steps of between 1.5 and 20 Oe to give an adequate number of points across the switching region. Examples of the curves are shown in the montage in Figure 6.2. To reduce the noise the DCD and IRM curves were first smoothed by a second degree polynomial fit

within a moving frame of 5 measurement points. Table 6.7 shows the remanent coercivity H_r , which is given by $DCD(H_r) = 0$ and the FWHM of the (main) peak in the irreversible susceptibility (χ_{irr}) curve as well as the corresponding parameters derived from the IRM curve. For certain samples especially those with high levels of MgO difficulties were experienced in obtaining reliable data at low fields for the DCD curves. This is because the change in the remanence with field was too rapid for the field steps available on the AGFM. Also the absolute value of the remanence was itself small so that the values measured were close to the resolution of the AGFM. The AGFM has a noise base of 2×10^{-8} emu [153] but due to environmental conditions it is usually closer to 10^{-7} emu for practical purposes. Given that the saturation remanence of the samples measured was of the order of 10^{-6} emu or lower this gave an effective signal to noise ratio of 10 or less.

Fe:MgO	Annealing time	Annealing field	H_r [Oe]	FWHM [Oe]	H'_r [Oe]	FWHM [Oe]
1:1	0	N/A	143 ± 5	41 ± 14	97 ± 5	$\approx 45 \pm 30$
1:1	1h	zero	318 ± 5	274 ± 7	339 ± 5	284 ± 7
1:1	2h	zero	273 ± 10	$\approx 300 \pm 50$	206 ± 10	$\approx 380 \pm 45$
1:1	3h	zero	233 ± 3	$\approx 285 \pm 30$	182 ± 3	$\approx 320 \pm 50$
1:1	3h	≈ 70 Oe	183 ± 3	118 ± 4	211 ± 3	151 ± 4
2:1	5h	≈ 70 Oe	151 ± 3	18 ± 4	130 ± 3	15 ± 4
3:1	3h	≈ 70 Oe	46 ± 2	5 ± 3	48 ± 2	7 ± 3
4:1	6h	≈ 70 Oe	91 ± 2	19 ± 3	86 ± 2	21 ± 3

Table 6.7: DCD and IRM parameters after annealing (e.a.).

A further difficulty with remanence measurements is the long measurement time. An AGFM was used because it measures much faster than the VSM. A simple hysteresis loop with about 100 points takes about 20 minutes in the VSM, while a loop with 1000 points can be measured in the AGM within 2 minutes. Still one IRM+DCD measurement took about 30 minutes in the AGFM. Unfortunately the AGFM probe is very sensitive to temperature changes in the room. The AGFM has the largest signal when the probe is driven at its natural resonance frequency. Small temperature changes shift the resonance frequency and therefore the signal during a long measurement decreases slowly. The IRM curve is always measured first, followed by the DCD curve. Therefore for high fields the IRM value is larger than the DCD value. The ΔM curve therefore does not approach 0 for large fields, but a small positive value. To reduce this effect the measurements were

performed as fast as possible by limiting the measurement range to the region of interest after the switching is mostly completed and by measuring as few points as possible. However this effect is visible in most of the ΔM curves.

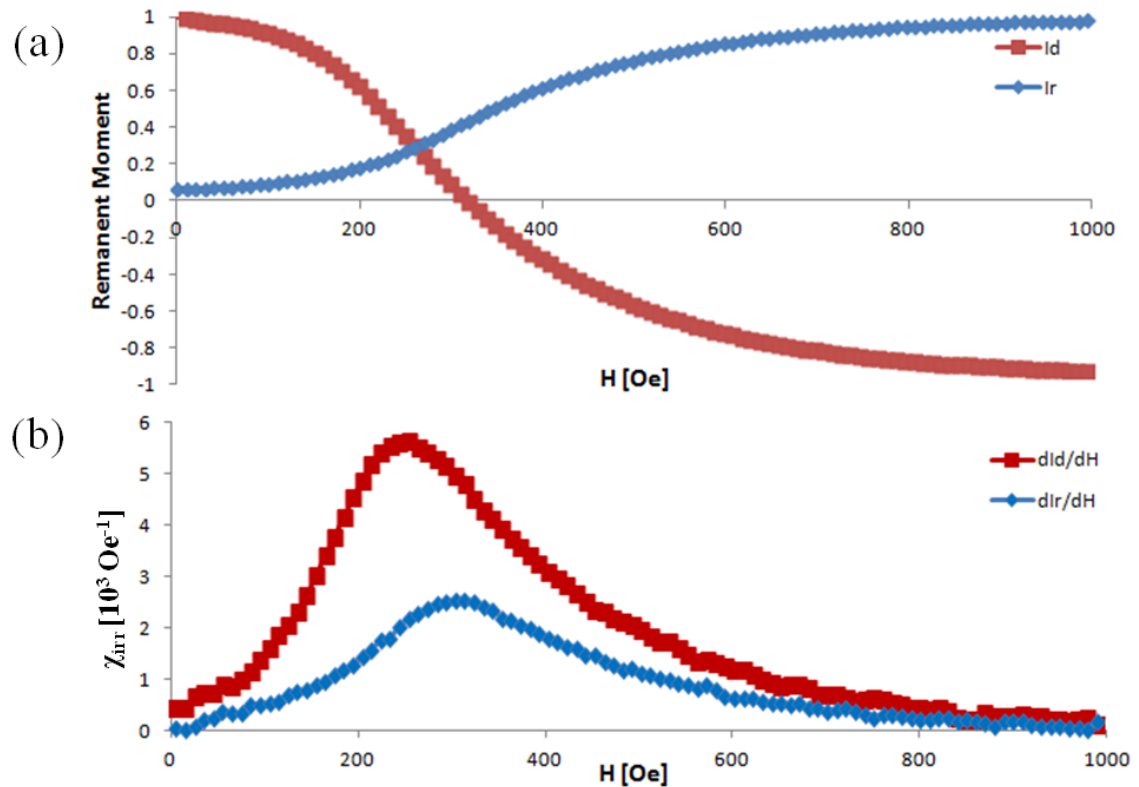


Figure 6.2: (a) DCD+IRM and (b) Irreversible susceptibility curves of the easy axis of the Fe:MgO=1:1 sample after 1h annealing in zero field.

A further difficulty occurred with the measurement of the IRM curves. In addition to the low signal and the shift of the resonance frequency of the probe described above, there was an inherent difficulty in demagnetizing the samples. Several techniques were attempted. The samples were repeatedly demagnetized by DC cyclic erasure [35] and measured. If the initial remanence was more than 10% of the remanence after saturation, the measurement was stopped and the demagnetization repeated. Samples with strong intergranular exchange interaction especially the Fe:MgO = 3:1 could not be demagnetized by DC cyclic erasure. For the Fe:MgO = 3:1 sample after 3h of annealing in ≈ 70 Oe field even with a step size of nominally 0.05 Oe, $\approx 1\%$ of the FWHM of the χ_{irr} curve, the remanent magnetization was still 90% of the maximum value. Saturating the sample perpendicular to the film plane left the sample with a remanent magnetization of 97% of the maximum value. Also AC erasure with a coil did not demagnetize the sample. The sample was pulled very slowly out of an AC coil with and without decreasing the

current through the coil. The remanent magnetization was always more than 30% of the remanent magnetization after saturation. A commercial AC tape head demagnetizer [154] could demagnetize the sample to approximately 10 % of the remanence after saturation after repeated exposures. This remanence after demagnetization is reflected in an offset at the start of the IRM curve of 0.1 and an offset at the start of the ΔM curve of 0.2. The difficulties in demagnetizing this sample is due to the large activation volume of reversal associated with cooperative reversal [35].

As expected the remanent coercivity values are larger than the coercivity values for all samples. The change of the coercivity with annealing time is reflected in the remanence coercivity. For example for Fe:MgO=1:1 the remanent coercivity is lowest for the as deposited sample. After 1h annealing in zero field the remanent coercivity increases strongly by more than a factor 2 but further annealing decreases the value.

Samples with Fe:MgO = 2:1 or higher have much narrower peaks in the irreversible susceptibility due to the intergranular exchange interaction compared with the exchange decoupled Fe:MgO = 1:1 sample. This result is as expected for an exchange coupled granular system exhibiting cooperative reversal. Similar results have been predicted by several models of longitudinal thin film media [36]. Experimental observations of similar effects again in thin film media were made by Mayo *et al.* [33].

Reference to table 6.7 and particularly the data for the Fe:MgO = 1:1 sample shows that the values of H_r do not even follow a smooth trend. Hence the grain growth is not uniform and the results will also be affected significantly by the strong exchange and dipole-dipole interactions. The energy barrier distribution for the demagnetizing process in the films are expected to shift to higher fields and broaden as the admixture concentration increases [155]. The DCD curve is the integral over the energy barrier distribution and the H_r value is therefore the mean of this distribution. When comparing field annealed samples the H_r value tends to increase with the concentration of MgO in the sample. However the Fe:MgO= 3:1 concentration does not fit into this trend. This is probably related to the unusually high moment per Fe atom the strong intergranular exchange coupling. Probably for the same reason the FWHM of χ_{irr} is much smaller than that of any other samples. The FWHM values of the other samples seem not to contradict the expectation of the broadening with increasing MgO concentration. The difference between the Fe:MgO =

1:1 sample and those of lower MgO concentrations is significant, but the FWHM of the Fe:MgO = 2:1 and 4:1 sample have overlapping error intervals.

Table 6.7 shows that for the Fe:MgO = 1:1 sample annealing tends to broaden the switching field distribution (FWHM). The wider distributions may be attributed to a wider distribution of grain sizes and a wider distribution of shape anisotropies. These features were probably obtained by grain growth through annealing. The broadening seems to be wider for zero field annealing than for annealing in a field. The reason is probably that the anisotropy axis direction is more random for zero field annealed films compared with field annealed films. The direction results from elongation of the grains. This therefore indicates a preferred growth and aggregation in this direction due to the field during annealing [19]. This also suggests the average elongation and therefore the shape anisotropy may be larger than in the zero field annealed sample. This can probably explain why the switching field distribution is much smaller than for the zero field annealed sample.

For Fe:MgO = 1:1 the peak position in the χ_{irr} curve for the demagnetizing process is at lower fields than that of the magnetizing process. In contrast for higher Fe concentrations the peak position in the χ_{irr} curve for the demagnetizing process is at higher fields than that of the magnetizing process, with the exception of the sample which was very difficult to demagnetize. This order of the positions is indicating negative (positive) interaction if the peak of demagnetizing is at lower(higher) fields than the magnetizing peak [33].

6.1.5 ΔM Curves

All ΔM measurements of Fe:MgO = 1:1 samples exhibit a dip in the ΔM curve which indicates negative intergranular interaction. The samples with larger Fe:MgO ratios exhibit positive intergranular interactions. With decreasing concentration of MgO in the film, the distance between the Fe grains decrease. This decrease in the distance causes an increase in the interactions, in particular the intergranular exchange interaction increases strongly. The intergranular exchange interaction becomes dominant when the concentration is Fe:MgO = 2:1 or higher. Such a result is expected from theoretical predictions [36] as well as from experimental work [33, 66]. Annealing can lead to grain growth and

aggregation of nanoparticles and therefore increase the ΔM value. [42]

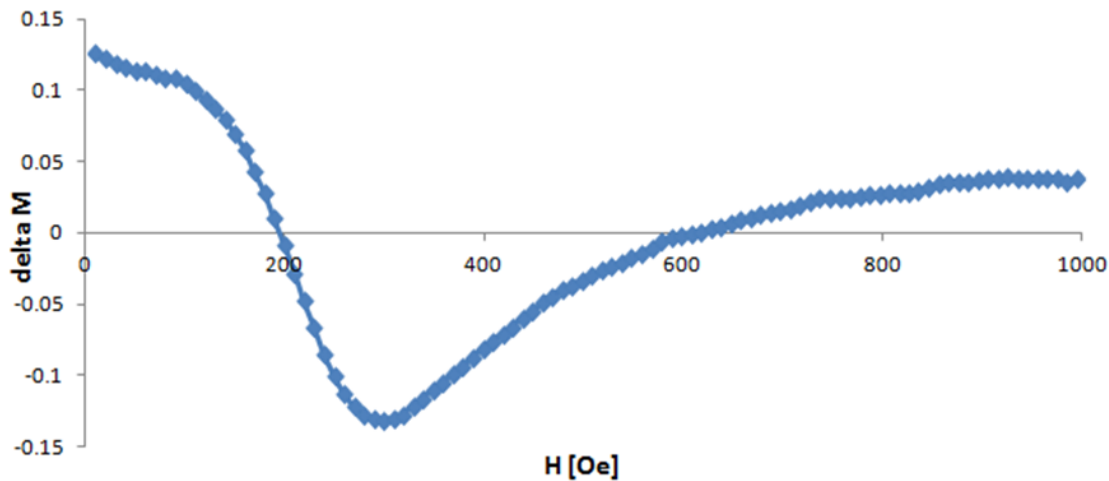


Figure 6.3: ΔM curve of the easy axis of the Fe:MgO=1:1 sample after 1h annealing in zero field.

The development of the ΔM curve of the Fe:MgO = 1:1 sample through annealing exemplifies the changes of the interactions through annealing. The dip width, amplitude and position indicate a grain growth and a small increase in the positive interaction through annealing. The dip width correlates strongly with the FWHM parameters and is indicating the region in which the switching happens. However the exact width is very difficult to determine, in particular for the sample after 2h and 3h annealing due to the low signal and to the influences of the offsets. When analysing the ΔM curves the offsets due to incomplete demagnetization and the shift of the resonance frequency of the AGFM probe with time, as described in section 6.1.4 always need to be considered. Figure 6.3 shows the ΔM curves of the easy axis of the Fe:MgO=1:1 sample after 1h annealing in zero field. The curve should ideally start and finish at 0, but the curve starts approximately at 0.12, indicating that the sample had $\approx 0.06M_r(\infty)$ remanent magnetization at the start of the IRM measurement. For high fields the ΔM curve approaches ≈ 0.04 instead of 0 which exemplifies the problem with the frequency shift as outlined in section 6.1.4. The width is therefore not quantified and does not give additional information, since the switching field distribution was already discussed with the help of the FWHM of the χ_{irr} in section 6.1.4. The amplitude of the dip is estimated as the average distance of the offsets to the dip. For the as deposited samples the amplitude of the dip is approximately 0.24 ± 0.03 . The annealing in zero field to 1h, 2h and 3h decreases the amplitude of the dip to 0.21 ± 0.03 , 0.21 ± 0.03 and 0.17 ± 0.03 respectively. This indicates a slight increasing

positive interaction due to grain growth [42], but the negative dipole-dipole interaction still dominates the intergranular interactions. The dip position of the as deposited 1:1 sample is 60 ± 10 Oe. After 1h annealing in zero field the position of the dip increases to 298 ± 10 Oe. Further annealing to 2h and 3h decreases the dip position to 220 ± 40 Oe and 120 ± 20 Oe, respectively. The dip position of the 1:1 samples are above the coercivity and below the remanent coercivity as determined by DCD and IRM. The dip position shows a good correlation to the remanent coercivity and therefore reflects the development of the median switching field with annealing. The strong initial increase after 1h of annealing is probably caused by aggregation and grain growth, while the decrease for longer annealing times might be attributed to oxidations in the film.

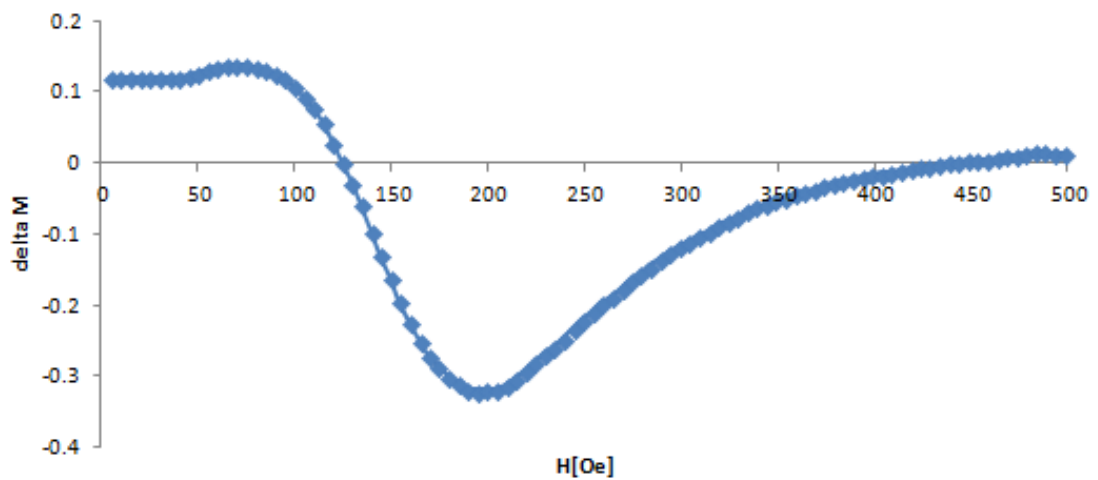


Figure 6.4: ΔM curve of the easy axis of the Fe:MgO=1:1 sample after 3h annealing in ≈ 70 Oe field.

Figure 6.4 shows the ΔM curve of a Fe:MgO=1:1 sample after 3h annealing in ≈ 70 Oe field. This figure looks qualitatively similar to figure 6.3 of the zero field annealed sample. A small difference is found at the start of the curve, where the ΔM value increases with the field with a maximum at approximately 70 ± 10 Oe. This maximum is just 0.02 higher than the offset start value. This small positive shoulder probably arises probably from a negligible exchange coupling contribution [156]. This shoulder is followed by a deep dip with an amplitude of 0.38 ± 0.03 . This may suggests a stronger dipole-dipole interaction or a weaker intergranular exchange interaction between the grains for field annealed films compared to zero field annealed films. This might indicate that the field supports the separation of the phases during annealing and the creation of larger MgO barriers between the Fe grains. The peak position is at 200 ± 10 Oe. This position is slightly above the

remnant coercivity as determined by DCD and quasi identical (overlapping error intervals) to the remnant coercivity as determined by IRM. Figure 6.5 shows the ΔM curve

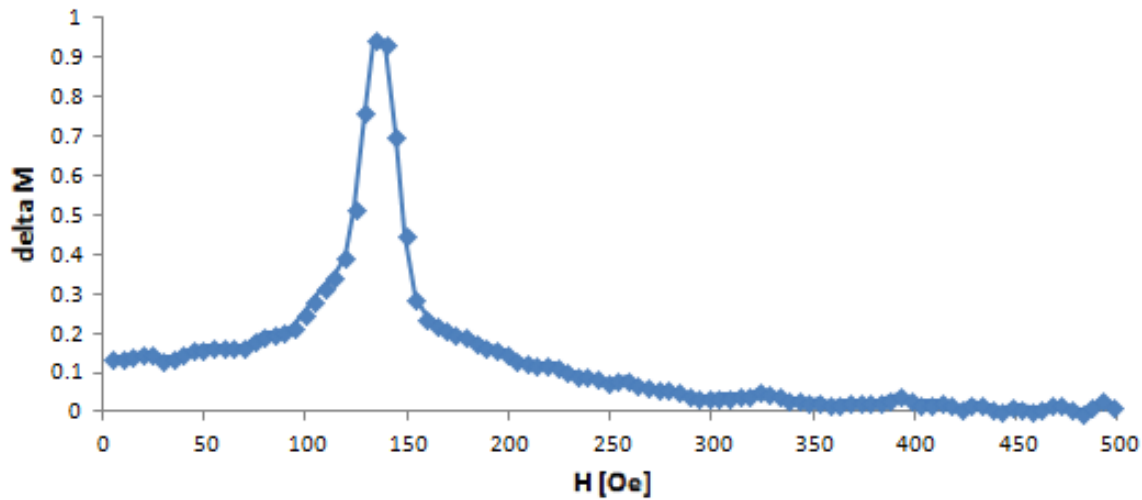


Figure 6.5: ΔM curve of the easy axis of the Fe:MgO=2:1 sample after 5h annealing in ≈ 70 Oe field.

of a Fe:MgO = 2:1 sample. The offset at low field is due to 7% saturation remanence at the start of the IRM measurement. The offset for high field is very small 0.01. The curve has a peak with an amplitude of 0.88 ± 0.02 . This is a clear indication of intergranular exchange interaction between the Fe grains in the sample. The peak position is below the remnant coercivity as determined from the DCD curve and quasi identical (overlapping error intervals) to the remnant coercivity as determined from the IRM curve.

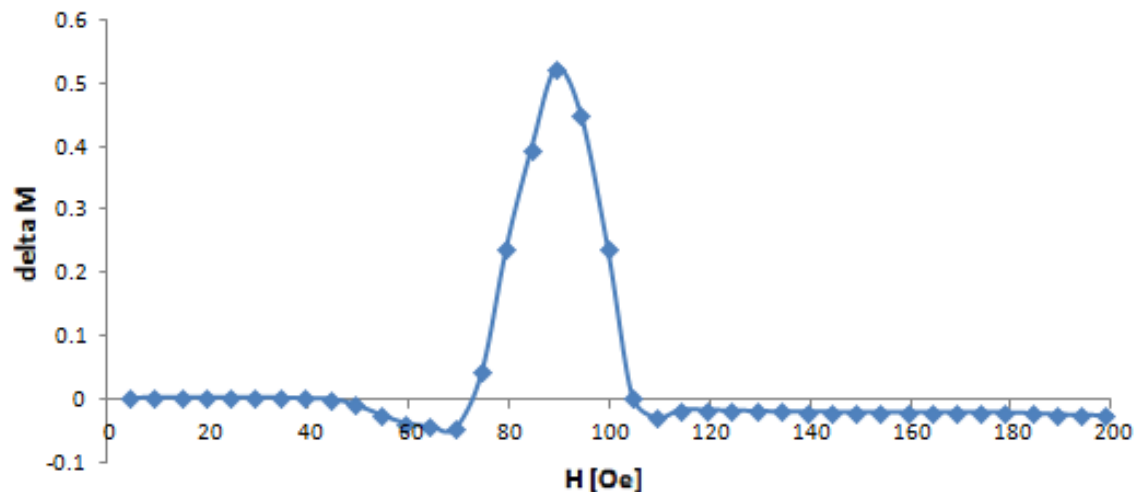


Figure 6.6: ΔM curve of the easy axis of the Fe:MgO=4:1 sample after 6h annealing in ≈ 70 Oe field.

Figure 6.6 shows the ΔM curve of a Fe:MgO = 4:1 sample. The ΔM curve shows a large peak at 89 ± 3 Oe with an amplitude of 0.51 ± 0.02 . Comparing this to the Fe:MgO = 2:1 sample the peak height is much lower. This suggests an decrease of the positive interaction or an increase in negative interactions. Since the Fe concentration is higher, the distance between the grains should be lower and the exchange interaction higher. However the magnetization is also higher leading to a larger demagnetization field of the sample, which acts as a negative interaction and reduces the peak amplitude of the ΔM curve. This finding is in accordance with the comparison of nucleation fields of the as deposited samples of different concentrations in section 6.1.1.

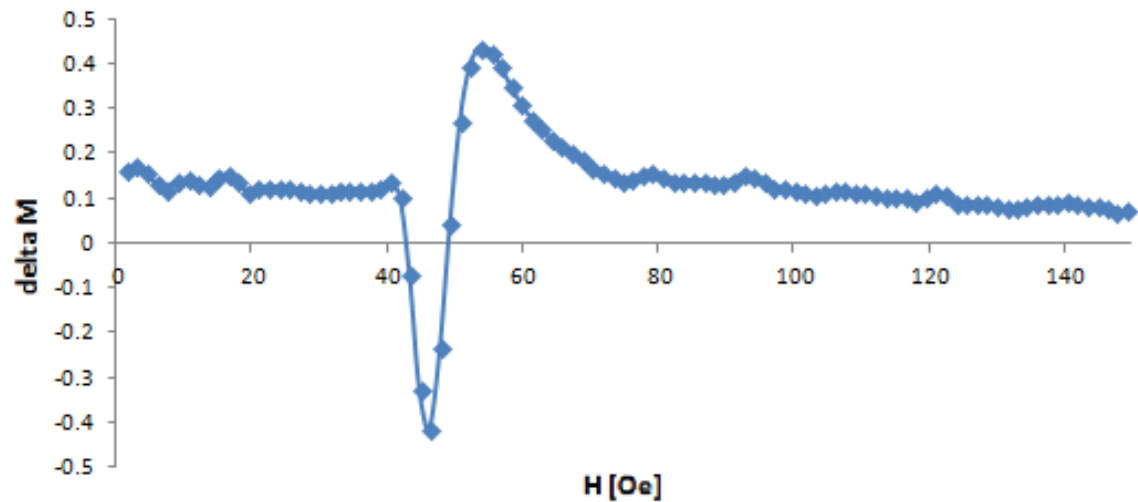


Figure 6.7: ΔM curve of the easy axis of the Fe:MgO=3:1 sample after 3h annealing in ≈ 70 Oe field.

Figure 6.7 shows the ΔM curve of a Fe:MgO = 3:1 sample. The ΔM curve looks very irregular with a dip before the peak. The sample was barely enough demagnetized for an acceptable IRM measurement. It was most difficult to demagnetize the sample and the irregular shape of the ΔM curve suggests that the demagnetized state was in fact not a properly demagnetized state. For each fraction of switching fields there should be no net magnetization. Assuming a material with no interaction and that the fractions of lower switching fields have a net magnetization in direction of the applied field for the IRM measurement and the fractions of higher switching fields have an opposing but equal net magnetization, then the material appears to be demagnetized. Such a state would result in an initial dip of the ΔM curve, because the fractions with lower switching field are already predominantly pointing in the field direction in the IRM measurement, while the grains start to switch in the DCD measurement. Such an improperly demagnetized state

of the sample was probably responsible for the dip before the peak in the ΔM curve. The difficulties to demagnetize the sample are a good indicator for very strong intergranular exchange interactions. It is not possible to make valid conclusions from this measurement.

The ΔM curves confirm the dependence of the interaction on the ratio of Fe:MgO. For Fe:MgO \geq 2:1 there is a dominating intergranular exchange interaction in the film dominating the reversal process. Annealing has not much influence on the interactions in the film, but it widens the switching field distribution.

6.2 Magnetoresistance Studies

As explained in section 2.9 magneto-resistance (MR) mainly derives from electron spin scattering when the charge carriers move through regions magnetized in different directions. Hence if the magnetization, which represents the degree of magnetic order, in the system varies with field via different mechanisms this will be reflected in the variation of MR with applied field. As described in section 6.1 the ratio of Fe to MgO in the samples studied in this work changes the magnetization process and hence the MR response. Also the enhanced easy axis induced by the growth process and subsequent field annealing affects the magnetic and hence the electrical properties. Thus a study of the electrical behaviour has been undertaken systematically so as to identify those effects which affect the MR.

For technical reasons the measurements were undertaken just with the current parallel to the MgO [110] or [-110] directions: The outer 2 pins of the 4 pins are 6mm apart, but the substrate in MgO [100] and [010] directions is just 5mm wide. By combining parallel and transverse magnetoresistance measurements, the AMR contribution of spin scattering can be separated from other MR effects [157]. Hence every sample was measured in 4 different configurations. These 4 geometries are shown schematically in figure 6.8. In this figure the black frame represents the sample. The orientations can be distinguished by triangle areas at the edges of the sample. These represent the areas without film due to shadowing during growth as described in section 4.4. The 4 black dots on the sample represent the 4 pins used for the resistance measurement and indicate the current direction.

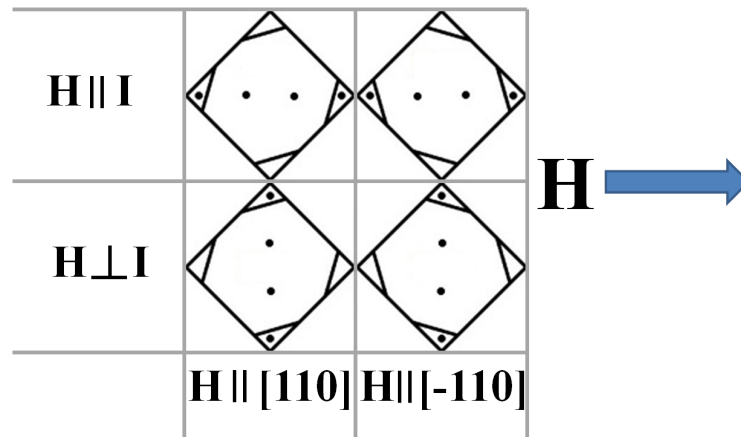


Figure 6.8: Schematic of the 4 different MR measurement geometries used.

The samples exhibit different MR effects. All samples show an isotropic MR effect at high fields. At low fields most samples show an anisotropic MR effect. The field annealed Fe:MgO = 1:1 sample shows additionally another MR effect, which is most likely a TMR or GMR effect.

6.2.1 MR at high fields

All samples exhibit a negative MR at high-fields which decreases quasi linearly out to the largest fields that it was possible to apply (≈ 3600 Oe). The slope varies between 0.1×10^{-3} and $17 \times 10^{-3}\%/kOe$. This negative MR is most likely a granular TMR or GMR effect due to the electron transport through superparamagnetic grains [64]. It may also be associated with the magnetic field suppression of spin-disorder scattering [158] or it could also originate from a suppression of the surface scattering in the thin film due to the Lorentz force. It is possible that all three of these effects are present and superimpose. Their contributions cannot be separated. However it is most likely that the effect is dominated by the granular TMR/GMR effect, since the other two effects are usually both very weak and require very high magnetic fields. Temperature dependent measurements and larger fields would be necessary draw definitive conclusions about the origin of this MR effect [20]. The granular TMR mechanism is outlined in section 2.9. Granular GMR usually requires magnetic grains in a non-magnetic metallic matrix. The materials studied in this work consist of magnetic Fe grains which might be separated by MgO. Instead of tunnelling through the MgO the electrons can also move through the

Au capping layer instead if the grains are in contact with the Au. Therefore the high field MR may be dominated by a granular GMR rather than TMR. This GMR seems similar to an in-plane GMR effect. The resistance change for in-plane GMR seems to originate mostly from interface scattering [5]. It is therefore plausible that the orientation of the magnetization of Fe grains in contact with the Au film are influencing the surface scattering at the Au film surface. This orientations will be field dependent.

The as deposited sample of Fe:MgO=1:1 shows a small slope of just $(1.9 \pm 0.8) \times 10^{-3} \%/\text{kOe}$. This value increases strongly after 1h annealing in zero field to $(15.5 \pm 0.8) \times 10^{-3} \%/\text{kOe}$. The annealing seems to have caused grain growth. Larger thermally activated grains are easier to align than smaller grains. Whereas for the as deposited sample about 10kOe were necessary to saturate the sample, less than 7kOe was enough to saturate the sample completely after 1h of annealing. This may explain the larger slope of the high field MR. Further annealing decreases the value to the lowest MR values measured in this work of $0.35 \times 10^{-3} \%$ with a slope of $0.1 \times 10^{-3} \%/\text{kOe}$ as was found in the Fe:MgO = 1:1 after 2h of annealing in zero field in a measurement with the current perpendicular to the magnetic field. This measurement took about 15 hours and is the result of averaging over 161 single loop measurements. Each resistance measurement is an average over 6 measurements with an 0.06 s integration time, 3 of them with +5mA current and 3 with -5mA current. Such long measurements were not performed in all directions and for all samples. The MR measurement is shown in figure 5.8 on page 86 and demonstrates the principal possibilities of the MR measurement setup. The other directions also show very small MR, but they are noisier and therefore less accurate. After annealing the sample for another hour in zero field, the MR measurements of the first few loops in all 4 measurement geometries showed that the MR was similarly small so the measurements were not continued. Annealing for more than 1h induced oxidation in the sample and therefore MR effects were almost completely suppressed.

The as deposited Fe:MgO = 2:1 sample shows a slope of $(2.1 \pm 0.4) \times 10^{-3} \%/\text{kOe}$ which is, within error, identical to the Fe:MgO = 1:1 sample. Again the annealing strongly increases the slope. The highest slope value of $(17 \pm 1) \times 10^{-3} \%/\text{kOe}$ was found after 5h (2h+3h) of annealing in a field of ≈ 70 Oe. Interestingly the other 5h annealed sample (1h+4h) has a slope of just $(5.8 \pm 0.8) \times 10^{-3} \%/\text{kOe}$. All other annealed samples with this ratio of Fe:MgO lay in between these values with no general trend.

For the Fe:MgO = 3:1 sample the slopes after field annealing are similar for different samples between 4.2×10^{-3} and 4.9×10^{-3} %/kOe. The samples were not oxidized, however the slope is lower than the slope for other ratios with the exception of the oxidized and as deposited samples. This suggests that these samples have just a small fraction of thermally activated or blocked grains or that the sizes of the thermally activated grains are smaller or a combination of these. Additionally the strong intergranular exchange interaction may reduce the size of TMR effects in granular systems [23].

For the Fe:MgO = 4:1 sample the slopes after field annealing are similar for different samples between 6.7×10^{-3} and 8.2×10^{-3} %/kOe. The lower variation between the samples with Fe:MgO = 3:1 and 4:1 indicates that the samples are more uniform. For the 4:1 sample that seems to contradict the M-H results, which suggested non-uniform growth profile during the fabrication of the film in the MBE system. However the higher Fe concentration in these samples seems to give more uniform conduction properties. This may indicate that in these samples tunnelling plays just a minor role in the electron transport and the high field MR probably originates from a granular GMR effect in these samples. For the GMR just the interface is relevant and not the actual thickness of the Fe-MgO-film. Therefore the magnetisation reversal parameters and the saturation magnetization may vary strongly between different samples, while the MR effects in these different samples are quite similar. This is a good indication, that there are GMR contributions in the Fe:MgO =4:1 sample and it is plausible that such contributions also exist in the high field MR of samples of different composition.

6.2.2 MR at low fields

In the low field region an anisotropic MR component is found for most samples i.e. the resistance depends on the direction between the current and the magnetic field. An example is shown in figure 6.14 on page 115 .For current parallel to the magnetic field, the resistance decreases in the vicinity of H=0 and for a current perpendicular the resistance increases. This MR effect seems to be superimposed on the negative MR at high-fields. This anisotropic MR component is probably due to an ordinary AMR effect. Some samples do not show this effect, when the magnetic field is applied along the easy axis, but do show it along the hard axis. This indicates that the reversal has no significant rotational

component and the reversal is caused by domain wall motion. Fe:MgO = 1:1 samples after annealing in a field of ≈ 70 Oe exhibit an additional MR contribution which cannot be explained by the high field slope or the AMR effect. This may indicate the presence of a GMR or TMR effect between grains that are switched.

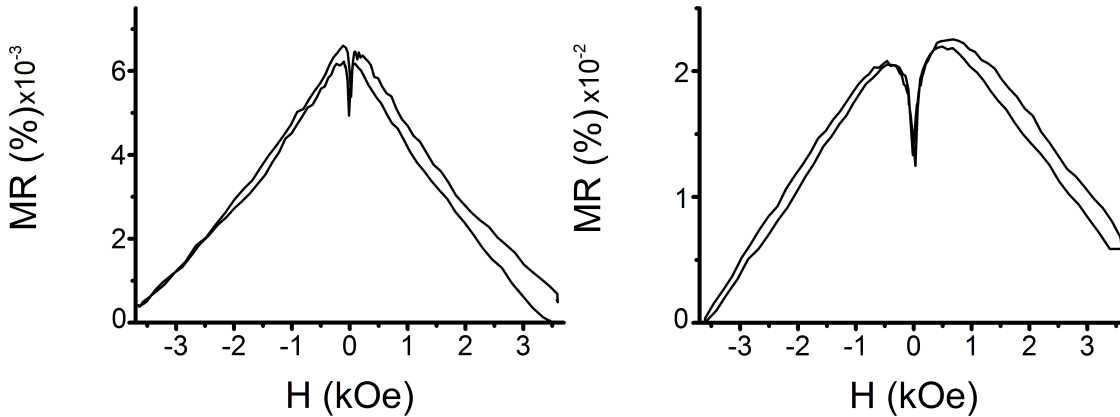


Figure 6.9: MR curve of Fe : MgO = 2:1 in easy axis direction with current parallel to the magnetic field. left: As deposited sample. right: Sample after 4h annealing in ≈ 70 Oe field.

It was more difficult to measure as deposited samples than samples after annealing. The MR measurements of these samples have larger noise and the MR values are smaller. The signal to noise ratio is therefore much larger, so some measurements just show noise. It seems that the as deposited samples show qualitatively the same reversal mechanisms as the samples after annealing. For example the as deposited Fe:MgO = 1:1 sample resembles the measurements after annealing in zero field: These measurements show negative MR with a single peak in the vicinity of the coercivity. The peak size is larger for current perpendicular to the field compared to current parallel to the field. Another good example is the measurement of the as deposited Fe:MgO = 2:1 sample. The measurement with current parallel to the magnetic field and along the easy axis is qualitatively the same as the measurement after 4h annealing in ≈ 70 Oe field as shown in figure 6.9. The MR values are approximately 3 times larger for the sample after annealing. The large noise and low MR in the as deposited samples is probably due to the low saturation magnetization value of the sample and probably a large fraction of thermally activated grains. It is therefore likely that the high field slope has a significant contribution from the granular TMR/GMR effect due to the electron transport through the grains [64].

The Fe:MgO=1:1 samples after annealing in a field of ≈ 70 Oe exhibit the most com-

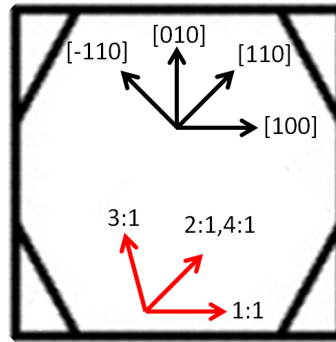


Figure 6.10: Schematic of the sample with easy axes and crystalline directions.

plex MR curve as shown in figure 6.11. The field is applied parallel to the current and parallel to the MgO [110] direction. The measurements on Fe:MgO = 1:1 samples were undertaken with the current at 45° to the easy axis because the pins do not fit onto the sample in direction of the easy axis. The geometry is shown schematically in figure 6.10. In figure 6.11 the blue line indicates the first half of the loop from positive to negative field and the red line the other half of the loop.

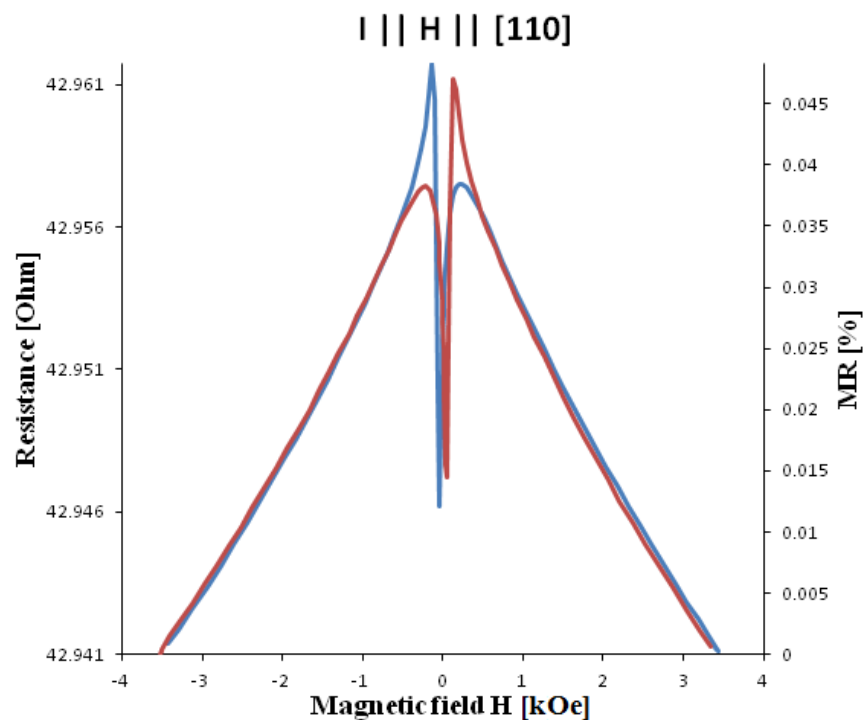


Figure 6.11: Magnetoresistance curve for the Fe:MgO=1:1 sample after 2h annealing in 70 Oe field.

The sample exhibits the typical high field negative MR as discussed previously. The resistance starts to drop when approaching zero magnetic field. This drop is most likely

due to reversible rotation processes, when the magnetization relaxes into the easy axis direction: Due to the fact that the angle between the magnetization and the current increases, the resistance decreases due to the AMR effect. The decrease accelerates dramatically after the magnetic field switches polarity. The moments of the grains are probably dragged away from the easy axis and the angle between the magnetization direction of the grains and current increases further. The MR curve reaches a minimum at the coercivity as shown in figure 6.12. Considering that the easy axis is at 45° to the magnetic field, the anisotropy axis of the grains are probably mainly aligned in this direction. According to the Stoner-Wolfarth model as discussed in section 2.4.2 the coercivity is equal to the critical switching field for this angle. After reaching the minimum the resistance suddenly increases to its highest value. This sudden jump is probably due to irreversible switching processes: When the critical field to overcome the anisotropy is reached, the grains switch irreversibly and the new angle of the magnetization is now between the easy axis and the field direction and therefore the angle between the current and magnetization is much smaller after the switching. Due to the AMR effect the resistance of a grain rises when it switches. This effect can account for the rise from the dip to the resistance value before the resistance started decreasing. The other effect contributing to the sharp peak is the resistance increase due to the electron transport between grains of different magnetization directions; in other words between grains which are already switched and which are not yet switched. This sharp peak is a clear indication of a granular TMR or GMR effect.

The MR loops with current perpendicular to the field of the Fe:MgO = 1:1 sample after annealing in a field of ≈ 70 Oe are less complex and show a single peak close to the coercivity. The peak is superimposed on the slope of the high field negative MR. The peak probably contains the same AMR and TMR contributions as in the case of current parallel to the magnetic field but with opposing sign for the AMR contribution. The TMR/GMR contribution is probably the largest, when half of the magnetic volume is switched and switching decreases the AMR contribution in this geometry. Therefore a peak is reached, when the decrease in the AMR overcomes the increase of the TMR/GMR shortly before the TMR/GMR contribution reached its maximum. The peak position is therefore at a slightly higher field than the coercivity.

The 1:1 samples before and after annealing in zero field have just one peak in each half-loop for all measurement geometries. The measurement taken after 1h of annealing

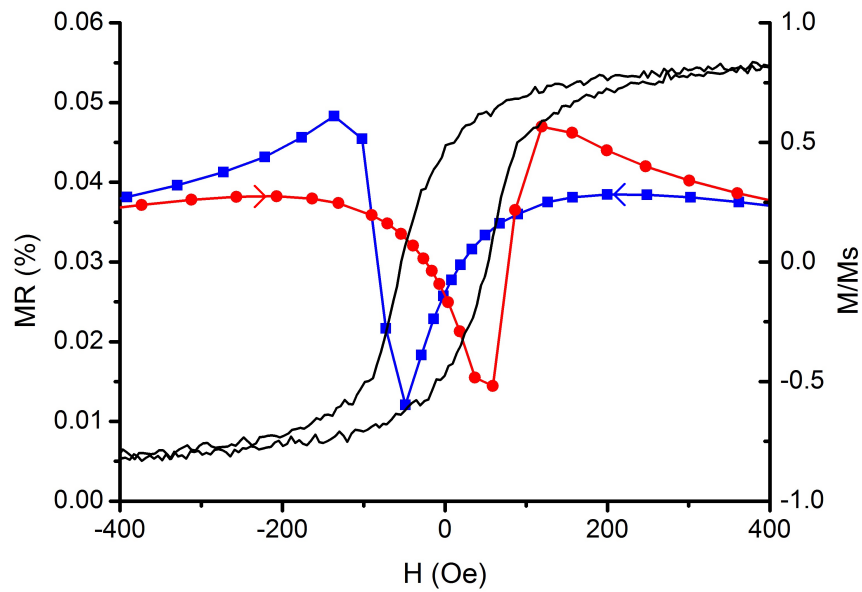


Figure 6.12: Superimposed magnetoresistance (red and blue) and M-H (black) curve for the Fe:MgO=1:1 sample after 2h annealing in 70 Oe field.

shows that the peak is superimposed on the high field negative MR slope. The signals for the other annealing times are too low to clearly distinguish between the different MR effects. For the measurement after 1h annealing the peak size is approximately 1/3 smaller for the H parallel to I (MR=0.11%) compared with H perpendicular I (MR=0.16%). The measurements of the as deposited sample and the sample after 2h annealing show the same trend. The lack of the dip in the case of current parallel to the magnetic field probably means that due to the more random anisotropy axis direction of the grains, the field sensitivity is smaller and the MR effects are smeared out over a wide field range [23]. The difference in the peak amplitude between current parallel and perpendicular to the magnetic field indicates that AMR is present in the film in addition to the granular TMR/GMR effects. After 3h annealing the sample was too oxidized to show any significant AMR contribution.

MR measurements of Fe:MgO = 1:1 samples indicate rotation as the major reversal mechanism for this concentration. The measurements also suggest the presence of TRM/GMR effects between super-paramagnetic and non-superparamagnetic grains. A decrease of the MgO concentration in the sample leads to a change in the reversal mechanism, which is reflected in the MR measurements. Figure 6.13 shows MR loops with the magnetic field applied along the easy (a) and hard (b) axis direction for Fe:MgO = 4:1 after

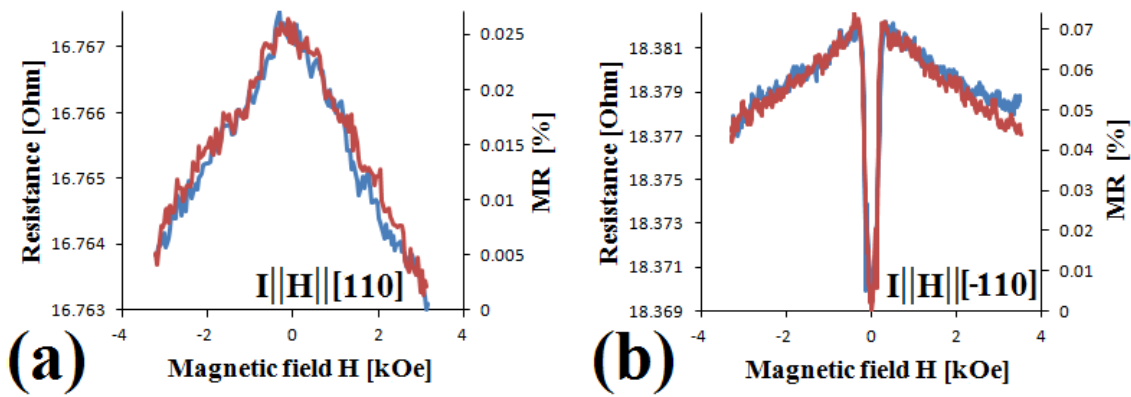


Figure 6.13: MR curves of the 4h annealed samples consisting of Fe:MgO = 4:1. The directions of the current and magnetic field applications are indicated in the figures. The magnetic field is parallel to the current and parallel to the easy axis (a) and hard axis (b). The blue line denotes signals obtained under a decreasing magnetic field from the maximum positive field to the maximum negative field while the red line denotes those under an increasing magnetic field. [9]

4h of annealing in ≈ 70 Oe field. The current is applied parallel to the magnetic field. For the magnetic field applied along the easy axis (a) no dip is found. This suggests that the magnetization direction is not rotating during the reversal, hence no AMR contribution can be seen. This may be understood by a reversal through domain wall motion in the sample with 180° domain walls. The (A)MR of the domain wall(s) is expected to be negligible small. All domains have their magnetization direction always parallel to the current direction and antiparallel to each other. For the measurement in the hard axis direction the domain or domains rotate their magnetization to the easy axis with decreasing external field. This causes the magnetization direction to become perpendicular to the current in the vicinity of $H=0$. The perpendicular magnetization direction has a lower resistance due to AMR. The magnitude of the dip can be up to 0.09% for the sample after 5 h annealing. The dip seems to be caused by the AMR effect as the comparison of loops with current perpendicular to the magnetic field and parallel to the magnetic field suggests. Such a comparison is shown in Figure 6.14. This curve is comparable in size and shape with that reported by Granberg *et al.* [159] for thin single crystal iron films where the spin-orbit coupling causes an anisotropic electron scattering [160]. This confirms that the samples become magnetically uniform for Fe:MgO = 4:1 due to the low MgO concentration in the film which means a small amount and/or weak pinning sites in the film. This finding is consistent with the results of the saturation magnetization and with the high squareness

of the hysteresis loops. The reversal mechanism through domain wall motion clearly indicates that the grains in the film are exchange coupled and reverse co-operatively. This is in accordance with the positive peak found in ΔM curves for Fe:MgO=4:1 samples.

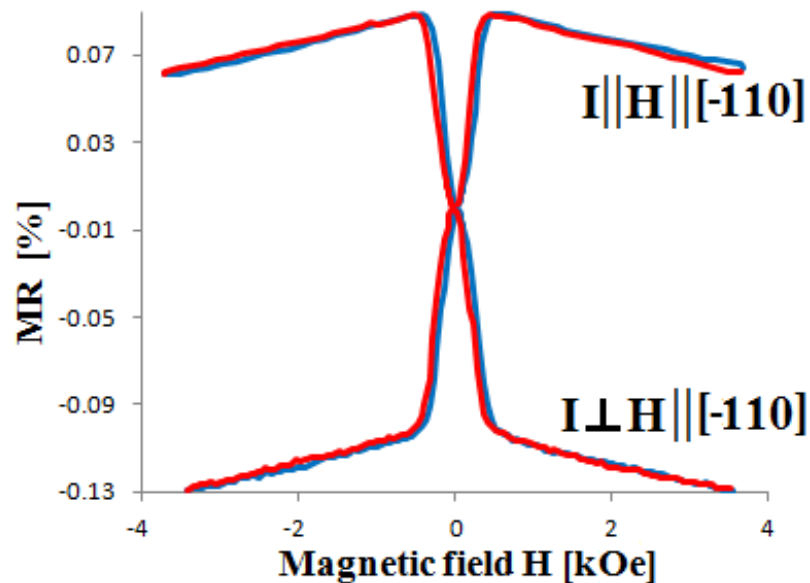


Figure 6.14: MR curves of the 5h annealed sample consisting of Fe:MgO = 4:1. The magnetic field is applied in the hard axis of the sample, while the current is applied parallel and perpendicular to the magnetic field for the top and bottom curves, respectively. [9]

The transition between reversal by domain wall motion and rotation can be seen in the Fe:MgO = 2:1 samples. Figure 6.9 shows MR loops with the magnetic field applied along the easy axis direction for Fe:MgO = 2:1. The current is applied parallel to the magnetic field. The measurements show a dip in the vicinity of $H = 0$, but otherwise the MR measurements of all geometries are qualitatively similar to the measurements of samples with lower MgO concentrations. This suggests that the reversal is mainly by domain wall motion but there seem to be small fractions of the film reversing by rotation. Another explanation of the dip could be that there are fractions of grains in the film with different easy axes. Deviating easy axes are possible since aggregation of grains can induce random axes. The dip in the hard axis directions are also wider than in samples with lower concentration of MgO. This may indicate less strong coupling between the magnetic moments in the domains and less magnetic uniformity in the film. Some Fe:MgO = 2:1 samples do not show the small dip in the vicinity of $H=0$ for the magnetic field in the easy axis and current parallel to the field. This suggests that for Fe:MgO = 2:1 the MgO content is barely sufficient to cause a minor contribution from rotation in the rever-

sal mechanism. This is also in accordance with overall positive interaction found by ΔM curves for Fe:MgO=2:1 samples.

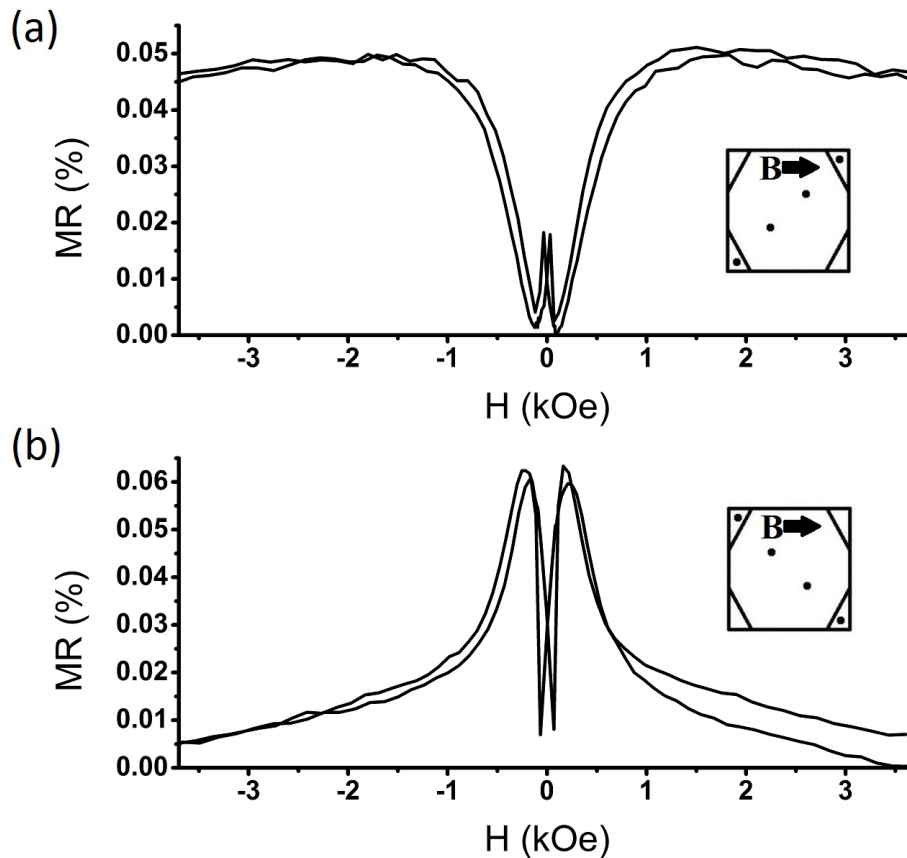


Figure 6.15: Magneto-resistance curve of Fe:MgO sample after 4h annealing in ≈ 70 Oe field. The directions of current and field are indicated in the inlay drawing.

The Fe:MgO = 3:1 samples also reverse cooperatively as does the Fe:MgO= 4:1. The deviation of the easy axes in the Fe:MgO = 3:1 samples from the MgO[010] direction can be seen in the MR measurements when applying the magnetic field along MgO[100] and applying the current at 45° to the magnetic field. Figure 6.15 shows two such measurements. When decreasing the magnetic field the magnetic moment of the film rotates in the direction of the nearest easy axis. In figure 6.10 the rotation is clockwise and the resistance in MgO[110] (MgO[-110]) reaches a minimum (maximum) when the magnetization directions passes MgO[-110] due to the AMR effect. When the magnetization direction reaches the easy axis in the vicinity of $H=0$, the resistance shows a local maximum (minimum). Reversing the field direction the magnetization then switches 180° by domain wall motion and after switching the increasing field rotates the magnetization again towards MgO[-110] resulting in a second maximum (minimum) when passing this

direction. The MR clearly shows the rotation direction of the magnetization. Since the rotation always passes through MgO[-110] but not MgO[110], a 180° reversal via domain wall motion is indicated. This proves the deviation of the easy axis from MgO[010] and also shows that the reversal is via domain wall motion. This is consistent with the indication of strong exchange coupling in the Fe:MgO = 3:1 sample as discussed in section 6.1. The strong AMR effect in these measurements suggests that the magnetization rotates predominantly uniformly and in the same direction. Multiple domains which rotate in opposing directions would greatly reduce the magnitude of the AMR. However this AMR is almost as large as that in the hard axis measurements with current parallel to the field for the Fe:MgO=2:1 and 4:1 samples (for technical reasons it was not possible to measure this in the Fe:MgO = 3:1 sample) where the rotation direction of the domains plays no role for the AMR contribution. This again confirms the extraordinarily strong coupling in the Fe:MgO = 3:1 sample which makes the magnetic film behave almost like a single domain. Such behaviour is typical for strongly exchange coupled thin films [3] and explains the great difficulty in demagnetizing the Fe:MgO = 3:1 samples.

Chapter 7

Conclusions and Further Work

7.1 Conclusions

Films of co-evaporated Fe:MgO on MgO substrate were investigated including the concentration and the annealing influence on the magnetization reversal and the magnetoresistance of the samples.

In this work it was shown that for films with the concentration Fe:MgO = 1:1 the dipole-dipole interaction dominates the magnetization reversal and for Fe:MgO = 2:1 or higher, intergranular exchange interactions dominate. This finding was supported by the squareness of the magnetization loops, the irreversible susceptibilities and the ΔM curves derived from IRM and DCD measurements. In samples with dominant dipole-dipole interactions the magnetization reversal is mainly by rotation, whereas in samples with dominant intergranular exchange interactions, the magnetisation reversal is mainly by domain wall motion. This was confirmed by MR measurements. The films with a ratio of Fe:MgO = 4:1 are magnetically uniform since the MR measurements show an AMR effect comparable to that of a thin single crystalline Fe film [159]. The Fe:MgO = 2:1 samples contains a small fraction of the film reversing by rotation instead of domain wall motion. All samples exhibit a negative MR at high-fields which decreases quasi linearly out to the largest fields that it was possible to apply (≈ 3600 Oe). This is probably a granular TMR or GMR effect due to electron transport through thermally activated grains [64]. Finally

the MR curves of Fe:MgO=1:1 after annealing in ≈ 70 Oe field show strong indications of granular TMR or GMR in non-thermally activated grains.

There are indications of grain growth through annealing: The remanence curves, the field necessary to reach saturation magnetization, the saturation magnetization value and the development of the MR are indicative of grain growth through annealing. Furthermore ΔM curves and MR measurements of the Fe:MgO = 1:1 sample indicate that annealing in a field leads to a preferred anisotropy axis in the films which might be attributed to a preferred growth direction [19]. The MR measurements suggest that field annealing leads to an aligned easy axis and an enhanced field sensitivity as expected from simulations [23]. There are clear indications that annealing can lead to oxidation in the films which decreases the MR, squareness, anisotropy and (saturation) magnetization but increases the coercivity.

The Fe:MgO = 3:1 sample shows an enhancement of the magnetic moment per Fe atom in the film of up to 20 %. The sample also shows very strong intergranular exchange coupling. This made it almost impossible to demagnetize the sample with the given equipment.

Some additional work was done as a part of my research. A brief conclusion of this work can be found in the Appendix.

7.2 Further Work

For further research in this area it would be interesting to produce samples without the Au capping layer. This layer short-circuited the Fe:MgO film and therefore lowered the MR. It is difficult to estimate this effect, since an Au thin film of 5nm thickness can have a lower resistance than that measured depending on the substrate on which it is grown [71]. The MR effect for the samples with higher MgO concentration could be significantly larger. As an alternative capping layer MgO would be ideal, however it has been claimed that this made it impossible to drive a current through the film [161]. Alternatively thin films with a higher resistance could be used like Palladium. Another alternative could be to use no capping layer at all. The sample would oxidize when taken out of the vacuum

chamber, so the measurements have to be done in situ. It is also possible to form contacts prior to film growth. This would enable a direct investigation of the electrical properties while the film is growing.

Further research would be temperature dependent measurements of the MR and M-H curves in particular of the Fe:MgO = 1:1 sample. This could confirm if the grains are superparamagnetic, which may be responsible for the shape of the M-H curve as well as for the negative high field MR. The high frequency magnetic properties of the material may be another property of interest, since such films may be used in high frequency inductors or noise filters [19]

Furthermore structural analysis using TEM could give insights in the nanostructure of the material and its changes through annealing. samples annealed in the TEM and the changes in the material could also be investigated directly.

There is also a case for research into FeCoB:MgO coevaporated films. In spin valves Ikeda *et al.* [21] showed that this system can result in higher TMR effects than the Fe/MgO system and the annealing temperature for this system has already been optimized.

Appendix

Requirements for a Nano-Spin Motor

As a part of my research I studied designs for nano-spin motors. The nano-spin motor is a research proposal of Dr. Atsufumi Hirohata [161]. The setup he proposed is similar to the Spin-Transistor of Datta and Das [14], which was realized by Koo *et al.* [10] in 2009. A spin polarized current is injected into a 2 dimensional electron gas (2DEG). The spin current is transported to another magnetic terminal and detected. A gate electrode can apply an electric field perpendicular to the 2DEG causing the spins of the electrons to precesses. The axis of this precession is perpendicular to the wave vector of the electron and the electrical field. Koo *et al.* implemented the spin injection using a non-local setup as shown in figure 1 It was planned to replace the detector terminal by an Iron disk. The precessing electrons are then injected into the disc and the magnetic moments in the disc start to rotate in the same way as the electrons due to spin transfer torque (STT). STT requires a high current density of the order of $10^8 \frac{A}{cm^2}$ [162] to move the magnet. The lowest literature value is $2.5 \cdot 10^6 \frac{A}{cm^2}$ [163]. The injector current density in the experiment of Koo *et al.* [10] was $3.1 \cdot 10^4 \frac{A}{cm^2}$ and half of the spin polarized electrons in a non-local geometry will not move in the direction of the detector. To reach a higher spin polarization it was planned to inject the electrons through a tunnel barrier. A tunnel barrier permits only electrons with their wave vector perpendicular to the 2DEG while a 2DEG by definition just contains electrons with wave vectors within this plane. This makes it impossible for them to tunnel directly into the 2DEG. It was claimed [161] a real 2DEG would not be necessary. It can be easily shown that in a 2DEG the phase shift of the spin of electrons due to a perpendicular electric field travelling between 2 points is independent of the path. However if electrons have the possibility to move with a

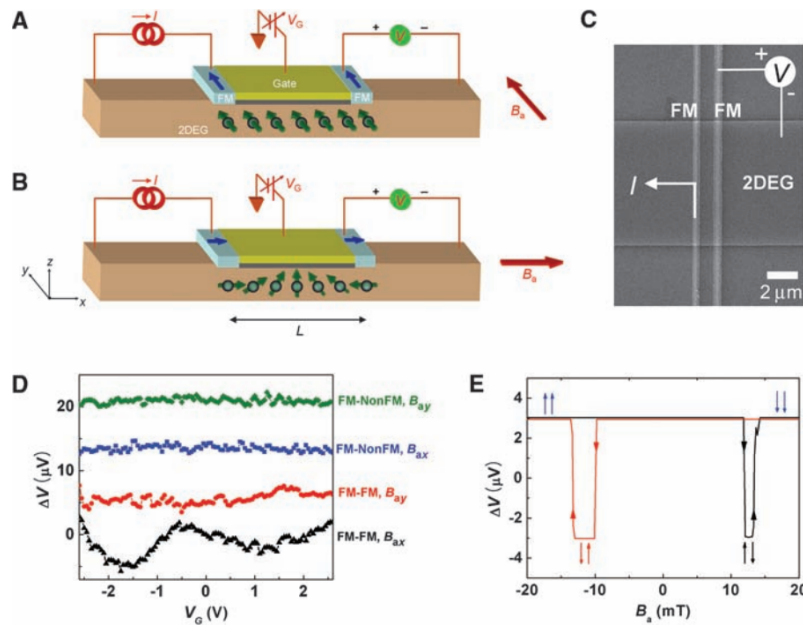


Figure 1: SpinFET experiment of Koo *et al.* [10]. (A) setup with magnetization of terminals in y direction. (B) SpinFET setup. (C) SEM of setup, before construction of gate. (D) Signal dependence on gate voltage for different experiments. Plots of different experiments are shifted for clarity. (E) Spin valve MR measurement.

component perpendicular to the 2DEG plane, the phase shift differs. It was planned [161] to have the magnetization of the injector as shown in figure 1A. Koo *et al.* [10] showed experimentally that the spins in such a setup do not precess.

It was then proposed [161] to make a nano-spin motor in an all-metallic system. There is no metallic 2DEG, so the rotation needs to be implemented differently. There are two possible solutions:

1. Assuming a SDP with uniaxial anisotropy in an alternating external magnetic field at an angle of e.g. 45° to the easy axis. The magnetization of this particle will rotate in the field according to the Stoner-Wohlfarth theory [3]. The external magnetic field could be replaced by a spin polarized current from an injector with its magnetization at e.g. 45° to the easy axis. An alternating current through the injector would cause an alternating spin polarization in the current and has therefore the same effect as the external magnetic field. However the movement of the magnetization will be rather irregular and micromagnetic computations are necessary to adjust the parameters of this system. However the rotation direction is always fixed

by the geometry.

2. It is also possible to conceive of using two separate injectors to mix the torques transmitted onto the disc. This leads to the concept of a nonvolatile multiple-valued memory.

Nonvolatile Multiple-Valued Memory

In conventional MRAM the magnetization of the free layer can have 2 different directions, indicating a 1bit. A single domain particle with low anisotropy can have the magnetic moment in any direction. Any direction which can be distinguished by a measurement can be seen as a value. The two-injector nano-spin motor can mix the torque arbitrarily and set the magnetic moment in any direction. Notches at the edge of the disc may create an anisotropy or a domain wall pin to ensure thermal stability. The MR of the circuit through the notched disc measures the projection of the magnetization on an injector. The combination of both MR values gives the magnetization vector and therefore the stored value. Figure 2 shows a design of a Nonvolatile Multiple-Valued Memory. The depicted area is $1.7\mu\text{m} \times 1.7\mu\text{m}$. Red is copper, yellow is gold, black is permalloy and blue the insulating substrate. The white arrows indicate the magnetization direction. For clarification, the edge of the notched disc and the edges of the injectors shine through the copper. The first production step is the patterning of the Au back-contact by lithography with lift-off or perpendicular milling. Next an insulator is deposited onto the substrate. Low-angle milling is then used to expose the top of the out Au contact. Permalloy is then deposited onto the substrate and capped with 1nm of Cu. Lithography and perpendicular milling cut out the notched disc on top of the Au contact and the two injectors. In the last patterning step the Cu contacts are formed. The notched disc in figure 2 has 6 easy axes due to the shape anisotropy and therefore 12 possible values. An alignment accuracy of 20nm is sufficient for this design. The notched disc is 200nm in diameter. The injectors are head to foot allowing flux closure which minimizes the stray field. The moments can be brought into this configuration by applying a magnetic field from bottom left to top right. After the magnetic field is turned off the moments relax into their easy axes. The wire coming out top left is connected to ground, while wires coming out at bottom left and top right have voltages applied. Small voltages are used to measure the MR

over the notched disk to the Gold electrode. This measurement will be done individually for each injector. Larger voltages will cause a high enough current for the magnetic moment to switch. Except for the magnetization directions parallel or anti-parallel to one of the terminals there will be voltages applied at both terminals causing a mixture of spin polarized electrons and an effective torque to set the magnetization in a certain direction. The advantage of this design is that the stored information per magnet is much greater,

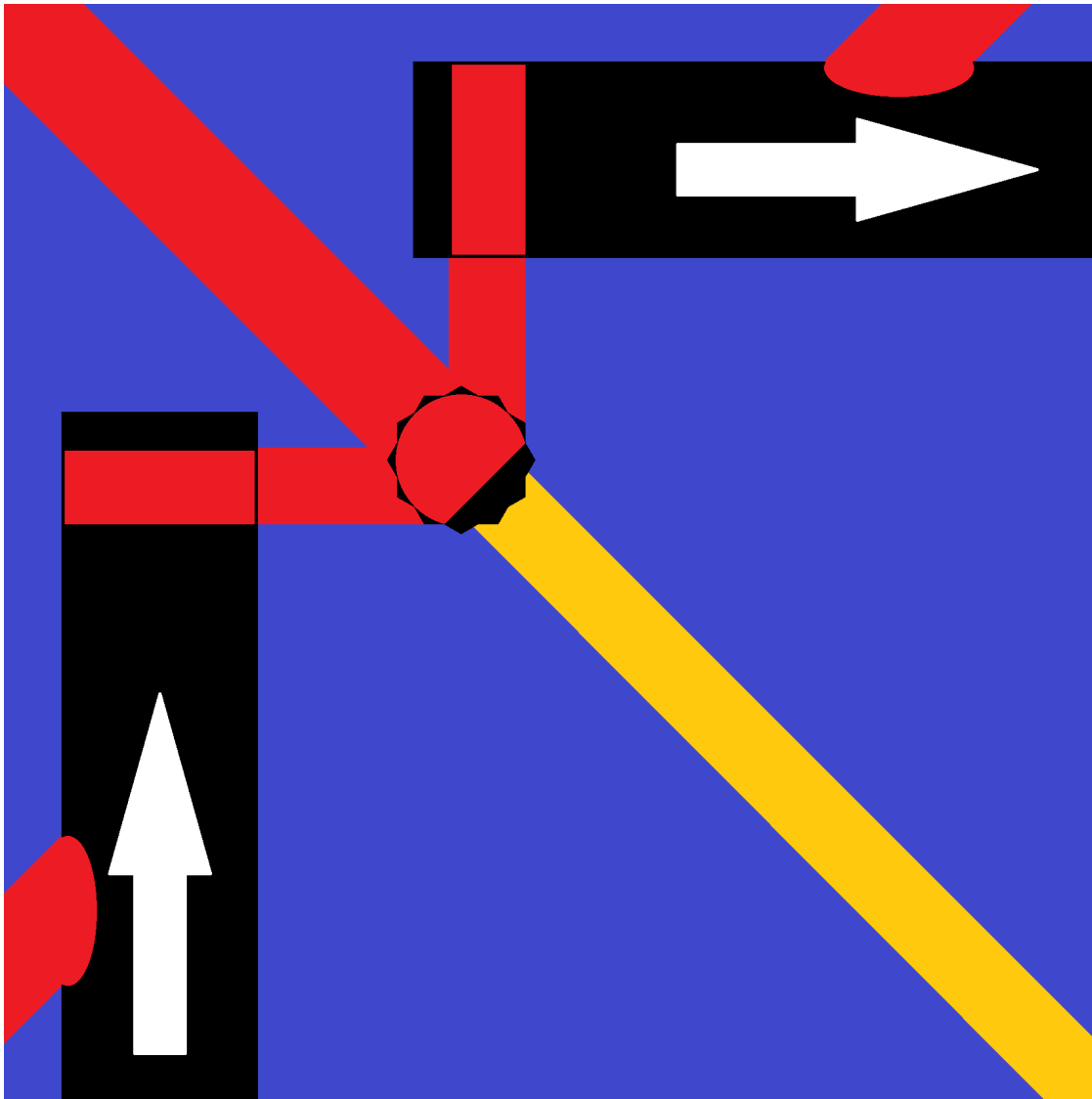


Figure 2: Nonvolatile Multiple-Valued Memory.

which can lead to a higher information density on an MRAM chip. The production of such a device should be possible in a state-of-the-art laboratory using EBL or a chip factory with 22nm node technology. A further development of this idea could be to have a notched sphere and read/write a 3D magnetization vector instead of a 2D vector.

List of Symbols

α	parameter of Langevin function
a	short semi axis of prolate ellipsoid
β	viscous damping parameter
b	short semi axis of prolate ellipsoid $b=a$
\vec{B}, B	magnetic flux density (vectoriell and absolut)
χ_{irr}	irreversible susceptibility
c	long semi axis of prolate ellipsoid
c_0	speed of light
C^*	Intergranular exchange coupling constant
C_{mobil}	mobility of domain wall
C_{MR}	geometric coefficient for calculating ordinary MR
ΔM	parameter for deviation from Wohlfarth model
$DOS_{\uparrow}, DOS_{\downarrow}$	densities of electrons with spin up, number of electrons with spin down
ϵ	angle between free and fixed layer in GMR or TMR sensor
e	Euler's number ≈ 2.71828 . Commonly used in exponential functions e.g. e^{x^2}
$\vec{e}_x, \vec{e}_y, \vec{e}_z$	Unit vectors of a coordinate system
E_{an}	anisotropy energy
E_b	energy barrier to magnetization reversal
E_C	energy necessary to generate a pair of neighbouring charged grains during tunnelling process
E_e	Intergranular exchange coupling energy
E_F	Fermi energy
E_{mr}	energy value associated with spin-flip scattering
f_0	frequency factor
γ	angle between easy axis and external magnetic field
\hbar	reduced Planck constant
h	normalized intergranular exchange interaction magnetic field strength
\vec{h}_e	normalized magnetic field strength
H	magnetic field strength
H_0	constant for the field which needs to be overcome to have a constant movement of the domain wall
\vec{H}_e	effective field representing the intergranular exchange interaction

H_c	coercivity
H_f	fluctuation field
H_n	nucleation field
H_K	anisotropy field
H_r	remanent coercivity
J^*	Intergranular exchange coupling energy constant
κ	wave vector
K	anisotropy energy density
k_B	Boltzmann's constant
\vec{m}	magnetic moment
λ^*	effective mean free path constant
ln	natural logarithm function
μ_{mobil}	mobility of electrons
m^*	effective electron mass
m_{3d}^* and m_{4s}^*	effective electron mass of 3d and 4s band electrons, respectively
m_e	mass of a free electron
\vec{m} , m	magnetic moment (vectoriell and absolut)
m_x, m_y, m_z	components of the vector \vec{m}
M	magnetization
M_d	value of DCD measurement
$\overline{M_d}$	normalized value of DCD measurement
M_r	value of IRM measurement
$\overline{M_r}$	normalized value of IRM measurement
M_R	remanent magnetization
M_s	saturation magnetization
MR	magneoresistace calculated as $MR = \frac{R - R_{min}}{R_{min}} 100\%$
MR_{max}	maximum MR values of a measurement
P, P₁, P₂	Spin polarization
P1,P2,P3,P4	solutions to the equation $\tau_{dp} + \tau_{an} = 0$ i.e. points of equilibrium of torques
ϕ	angle between magnetic moment and external magnetic field
π	Pi i.e ≈ 3.14159
px	pixel
q	charge

Q	quality factor of a resonance
ρ	resistivity
ρ_0	bulk resistivity
R	electrical resistance
R_+	electrical resistance of majority electrons
R_-	electrical resistance of minority electrons
$R_{\uparrow\uparrow}$	electrical resistance of TRM device with parallel aligned magnetizations
$R_{\uparrow\downarrow}$	electrical resistance of TRM device with anti-parallel aligned magnetizations
$R_{nonmagnet}$	electrical resistance of the non-magnetic metal
R_{s+s+}	electrical resistance contribution from electrons scattering within the s-band of the majority spin state of the charge carriers
R_{s-s-}	electrical resistance contribution from electrons scattering within the s-band of the minority spin state of the charge carriers
R_{s+d+}	electrical resistance contribution from electrons scattering from the s-band to the d-band of the majority spin state of the charge carriers
R_{s-d-}	electrical resistance contribution from electrons scattering from the s-band to the d-band of the minority spin state of the charge carriers
R^2	coefficient of determination
r_{cc}	centre-to-centre distance of grains
R_{max}	maximum resistance during a measurement
R_{min}	minimum resistance during a measurement
RA	resistance area product
Σ	sum
s	mean separation of Fe particles
S	time dependence coefficient
S*	coercivity squareness
sin	sine-function
θ	angle between magnetic moment and easy axis
θ_C	critical angle for irreversible switching
$\bar{\tau}$	average scattering time
τ_N	relaxation time
τ_{an}	torque on a magnetic moment by anisotropy
τ_{dp}	torque on a magnetic moment by a magnetic field

tan	tangents-function
t	thickness
t_0	time constant
T	temperature
T_B	blocking temperature
t_M	elapsed time
TMR	TMR ratio
U	voltage
U_{bar}	effective potential barrier
v	velocity (e.g. speed of the domain wall)
V	volume
V_{ac}	activation volume
V_P	critical particle volume
W	work per unit volume
·, ×	multiplication
·	a vector dot-product in equations between vectors
×	cross product in equations between vectors
°	degree as in ° C for temperature or for angel measure

List of Abbreviations

2DEG	2 Dimensional Electron Gas
AC	Alternating Current
AGFM	Alternating Gradient Force Magnetometer
Al_2O_3	Auminium Oxide also known as Alumina
AMR	Anisotropic Magnetoresistance
Au	Gold (Latin: Aurum)
B	Boron
bcc	b ody- c entred c ubic
BFP	B ack- F ocal P lane
CCD	C arge- C oupled D evice
CIP	C urrent i n P lane (geometry/setup)
Co	C obalt

CoFeB	C obalt- I ron- B oron
CPP	C urrent P erpendicular to the P lane (geometry/setup)
Cu	C opper (Latin: C uprum)
CVD	C hemical V apour D eposition
DAQ	D ata A cquisition
DC	D irect C urrent
DCD	D C- D emagnetisation
DOS	D ensity of S tates
DP	D iffraction P attern
DSP	D igital S ignal P rocessing
e.a.	e asy a xis
EDX	E nergy- D ispersive X -ray spectroscopy
fcc	f ace- c entred c ubic
Fe	I ron (Latin: F errum)
FET	F ield E ffect T ransistor
FIB	F ocused I on B eam
FWHM	F ull W idth H alf M aximum
GaAs	G alium A rsenide
Ge	G ermanium
GMR	G iant M agneto r esistance
h.a.	h ard a xis
hcp	h exagonal c lose- p acked
HiTUS	H igh T arget U tutilisation S puttering
IPA	I sopropyl a lcohol
IRM	I sothermal R emance M agnetization
MBE	M olecular B eam E pitaxy
Mg	M agnesium
MgO	M agnesium O xide
MIBK	M ethyl i sobutyl k etone
MOKE	M agneto- o ptic K err e ffect
MR	M agneto r esistance
MRAM	M agneto r esistive R andom A ccess M emory
O	O xigen

PIPS	P recession I on P olishing S ystem
PLD	P ulsed L aser D eposition
PMMA	P oly M ethyl M ethacrylate
PVD	P hysical V apour D eposition
QD	Q uantum D ot
RHEED	R eflection H igh E nergy E lectron D iffraction
RT	R oom T emperature
sccm	standard cubic centimeter per minute
SDP	S ingle D omain P article
SEM	S canning E lectron M icroscope
SET	S ingle- E lectron- T ransistor
SOI	S pin O rbital I nteraction
STT	S pin T ransfer T orque
Ta	Tantalum
TEM	T ransmission E lectron M icroscope
TMR	T unneling M agneto R esistance
UHV	U ltra H igh V acuum
VSM	V ibrating S ample M agnetometer

Bibliography

- [1] B. Kaeswurm, "Finite size effects in exchange bias systems," Ph.D. dissertation, The University of York, Department of Physics, April 2011. 3, 82
- [2] A. Hubert and R. Schäfer, *Magnetic domains: the analysis of magnetic microstructures*. Springer, 1998. [Online]. Available: <http://books.google.com/books?id=1BLBWbPXrUgC> 9, 24, 25
- [3] B. Cullity and C. Graham, *Introduction to magnetic materials*. Wiley-IEEE Press, 2009. [Online]. Available: <http://books.google.com/books?id=kk1el8vB4HoC> 9, 23, 24, 26, 28, 33, 35, 36, 43, 44, 46, 117, 124
- [4] M.-P.-G. zur Förderung der Wissenschaften, *Jahrbuch 2006*. K.G. Saur, 2006, vol. Forschungsbericht 2006 - Max-Planck-Institut für Mikrostrukturphysik. [Online]. Available: <http://www.mpg.de/415574/forschungsSchwerpunkt>
- [5] T. Shinjo, *Nanomagnetism and spintronics*. Elsevier Science, 2009. [Online]. Available: <http://books.google.co.uk/books?id=0fLXcCl3HikC> 9, 20, 61, 108
- [6] J. Vossen and W. Kern, Eds., *Thin film processes II*. Academic Press, 1991, vol. 2. [Online]. Available: <http://books.google.com/books?id=esrnRuSz2u8C> 10, 67, 72
- [7] L. R. Fleet, "Interface and transport properties of fe/gaas(001) heterostructures," Ph.D. dissertation, The University of York, Department of Physics, Mar. 2012. [Online]. Available: <http://etheses.whiterose.ac.uk/2341/> 10, 62, 64, 73
- [8] J. Mallinson, "Magnetometer coils and reciprocity," *J. Appl. Phys.*, vol. 37, no. 6, pp. 2514–2515, May 1966. [Online]. Available: <http://dx.doi.org/10.1063/1.1708848> 10, 77

- [9] M. Rummey, L. R. Fleet, H. Hing, X. Zhang, and A. Hirohata, "Magnetic properties of epitaxial co-evaporated fe:mgo anti-granular films," *Magnetics, IEEE Transactions on*, vol. 48, no. 11, pp. 4010–4013, 2012. [Online]. Available: <http://dx.doi.org/10.1109/TMAG.2012.2198456> 11, 21, 47, 114, 115
- [10] H. C. Koo, J. H. Kwon, J. Eom, J. Chang, S. H. Han, and M. Johnson, "Control of spin precession in a spin-injected field effect transistor," *Science*, vol. 325, no. 5947, pp. 1515–1518, 2009. [Online]. Available: <http://www.sciencemag.org/cgi/content/abstract/325/5947/1515> 11, 19, 62, 123, 124
- [11] V. G. Lewis, "Development and applications of an alternating gradient force magnetometer," Ph.D. dissertation, School of Electronic Engineering and Computer Systems, University of Wales, Bangor, Gwynedd, Jan. 1995. 15, 80
- [12] G. Binasch, P. Grünberg, F. Saurenbach, and W. Zinn, "Enhanced magnetoresistance in layered magnetic structures with antiferromagnetic interlayer exchange," *Phys. Rev. B*, vol. 39, pp. 4828–4830, Mar 1989. [Online]. Available: <http://link.aps.org/doi/10.1103/PhysRevB.39.4828> 19, 51, 59
- [13] M. N. Baibich, J. M. Broto, A. Fert, F. N. Van Dau, F. Petroff, P. Etienne, G. Creuzet, A. Friederich, and J. Chazelas, "Giant magnetoresistance of (001)fe/(001)cr magnetic superlattices," *Phys. Rev. Lett.*, vol. 61, no. 21, pp. 2472–2475, Nov. 1988. [Online]. Available: <http://link.aps.org/doi/10.1103/PhysRevLett.61.2472> 19, 51, 59
- [14] S. Datta and B. Das, "Electronic analog of the electro-optic modulator," *Applied Physics Letters*, vol. 56, no. 7, pp. 665–667, 1990. [Online]. Available: <http://dx.doi.org/10.1063/1.102730> 19, 62, 123
- [15] J. C. Slonczewski, "Current-driven excitation of magnetic multilayers," *Journal of Magnetism and Magnetic Materials*, vol. 159, no. 1-2, pp. L1–L7, Jun. 1996. [Online]. Available: <http://www.sciencedirect.com/science/article/pii/0304885396000625> 19
- [16] L. Berger, "Emission of spin waves by a magnetic multilayer traversed by a current," *Phys. Rev. B*, vol. 54, no. 13, pp. 9353–9358, Oct. 1996. [Online]. Available: <http://link.aps.org/doi/10.1103/PhysRevB.54.9353> 19

- [17] A. Hatfield, "Everspin debuts first spin-torque mram for high performance storage systems," Press release on webpage of Everspin Technologies, Inc. (www.everspin.com) from 12th, Nov. 2012. [Online]. Available: http://www.everspin.com/PDF/ST-MRAM_Press_Release.pdf 19
- [18] H. Fujimori, S. Mitani, and S. Ohnuma, "Tunnel-type gmr in metal-nonmetal granular alloy thin films," *Materials Science and Engineering: B*, vol. 31, pp. 219–223, Apr. 1995. [Online]. Available: <http://www.sciencedirect.com/science/article/pii/0921510794080321> 20, 53
- [19] S. Ohnuma, M. Ohnuma, H. Fujimori, and T. Masumoto, "Metal-insulator type nano-granular soft magnetic thin films investigations on mechanism and applications," *Journal of Magnetism and Magnetic Materials*, vol. 310, no. 2, Part 3, pp. 2503–2509, Mar. 2007. [Online]. Available: <http://www.sciencedirect.com/science/article/pii/S0304885306024322> 20, 101, 120, 121
- [20] H. Fujimori, S. Ohnuma, N. Kobayashi, and T. Masumoto, "Spintronics in metal-insulator nanogranular magnetic thin films," *Journal of Magnetism and Magnetic Materials*, vol. 304, no. 1, pp. 32–35, Sep. 2006. [Online]. Available: <http://www.sciencedirect.com/science/article/pii/S0304885306001715> 20, 107
- [21] S. Ikeda, J. Hayakawa, Y. Ashizawa, Y. M. Lee, K. Miura, H. Hasegawa, M. Tsunoda, F. Matsukura, and H. Ohno, "Tunnel magnetoresistance of 604300 k by suppression of ta diffusion in cofeb/mgo/cofeb pseudo-spin-valves annealed at high temperature," *Appl. Phys. Lett.*, vol. 93, no. 8, pp. 082 508–3, Aug. 2008. [Online]. Available: <http://dx.doi.org/10.1063/1.2976435> 20, 53, 60, 65, 121
- [22] N. Kobayashi, S. Ohnuma, S. Murakami, T. Masumoto, S. Mitani, and H. Fujimori, "Enhancement of low-field-magnetoresistive response of tunnel-type magnetoresistance in metal-nonmetal granular thin films," *Journal of Magnetism and Magnetic Materials*, vol. 188, no. 1-2, pp. 30–34, Sep. 1998. [Online]. Available: <http://www.sciencedirect.com/science/article/pii/S0304885398001693> 21
- [23] Z. Mao and X. Chen, "Tunnelling magnetoresistance in disordered interacting nanoparticles," *Journal of Physics D: Applied Physics*, vol. 43, no. 42, pp. 425 001–

- , 2010. [Online]. Available: <http://stacks.iop.org/0022-3727/43/i=42/a=425001>
21, 55, 56, 109, 113, 120
- [24] R. H. Wade, “The determination of domain wall thickness in ferromagnetic films by electron microscopy,” *Proceedings of the Physical Society*, vol. 79, no. 6, pp. 1237–, 1962. [Online]. Available: <http://stacks.iop.org/0370-1328/79/i=6/a=318>
26
- [25] Y. Kryuchkov, “Concentration dependence of the mean interparticle distance in disperse systems,” vol. 42, no. 11-12, pp. 390–392–, 2001. [Online]. Available: <http://dx.doi.org/10.1023/A%3A1015071103237> 26
- [26] O. Durand, J. Childress, P. Galtier, R. Bisaro, and A. Schuhl, “Origin of the uniaxial magnetic anisotropy in fe films grown by molecular beam epitaxy,” *Journal of Magnetism and Magnetic Materials*, vol. 145, no. 1-2, pp. 111–117, Mar. 1995. [Online]. Available: <http://www.sciencedirect.com/science/article/pii/030488539401308X> 27
- [27] K. O’Grady, R. Chantrell, J. Popplewell, and S. Charles, “The low temperature magnetisation of a system of fine cobalt particles,” *Magnetics, IEEE Transactions on*, vol. 16, no. 5, pp. 1077–1079, 1980. 29
- [28] W. F. Brown, Jr., “The fundamental theorem of fine-ferromagnetic-particle theory,” *J. Appl. Phys.*, vol. 39, no. 2, pp. 993–994, Feb. 1968. [Online]. Available: <http://dx.doi.org/10.1063/1.1656363> 29
- [29] A. Aharoni, “Brown’s ‘fundamental theorem’ revisited,” *J. Appl. Phys.*, vol. 90, no. 9, pp. 4645–4650, Nov. 2001. [Online]. Available: <http://dx.doi.org/10.1063/1.1407313> 30
- [30] G. Di Fratta, C. Serpico, and M. d’Aquino, “A generalization of the fundamental theorem of brown for fine ferromagnetic particles,” *Physica B: Condensed Matter*, vol. 407, no. 9, pp. 1368–1371, May 2012. [Online]. Available: <http://www.sciencedirect.com/science/article/pii/S0921452611010519> 30
- [31] E. C. Stoner and E. P. Wohlfarth, “A mechanism of magnetic hysteresis in heterogeneous alloys,” *Philosophical Transactions of the Royal Society of London. Series A, Mathematical and Physical Sciences*, vol. 240, no. 826, pp. 599–642,

- May 1948. [Online]. Available: <http://rsta.royalsocietypublishing.org/content/240/826/599.abstract> 30, 35
- [32] D. Jiles, *Introduction to Magnetism and Magnetic Materials*, 2nd ed. Chapman & Hall, 1998. [Online]. Available: <http://books.google.com/books?id=axyWXjsdorMC> 30
- [33] P. I. Mayo, K. O'Grady, P. E. Kelly, J. Cambridge, I. L. Sanders, T. Yogi, and R. W. Chantrell, "A magnetic evaluation of interaction and noise characteristics of conic thin films," *J. Appl. Phys.*, vol. 69, no. 8, pp. 4733–4735, Apr. 1991. [Online]. Available: <http://dx.doi.org/10.1063/1.348263> 37, 38, 42, 100, 101
- [34] E. P. Wohlfarth, "Relations between different modes of acquisition of the remanent magnetization of ferromagnetic particles," *J. Appl. Phys.*, vol. 29, no. 3, pp. 595–596, Mar. 1958. [Online]. Available: <http://dx.doi.org/10.1063/1.1723232> 39
- [35] M. El-Hilo, K. O'Grady, and R. Chantrell, "Demagnetised states and activation volumes in thin-film media," *Journal of Magnetism and Magnetic Materials*, vol. 120, no. 1-3, pp. 244–246, Mar. 1993. [Online]. Available: <http://www.sciencedirect.com/science/article/pii/0304885393913333> 39, 99, 100
- [36] C. Mee and E. Daniel, *Magnetic Recording: Technology*, 2nd ed. McGraw-Hill, 1987, no. v. 1. [Online]. Available: <http://books.google.co.uk/books?id=LUITAAAAMAAJ> 40, 100, 101
- [37] J.-G. Zhu and H. N. Bertram, "Micromagnetic studies of thin metallic films," *Journal of applied physics*, vol. 63, no. 8, pp. 3248–3253, 1988. 41, 93
- [38] C. D. Mee and E. D. Daniel, Eds., *Magnetic recording technology*, 2nd ed. McGraw-Hill (New York), 1996. 41
- [39] P. E. Kelly, K. O'Grady, P. I. Mayo, and R. Chantrell, "Switching mechanisms in cobalt-phosphorus thin films," *Magnetics, IEEE Transactions on*, vol. 25, no. 5, pp. 3881–3883, 1989. [Online]. Available: <http://dx.doi.org/10.1109/20.42466> 42
- [40] D. L. Leslie-Pelecky and R. D. Rieke, "Magnetic properties of nanostructured materials," *Chem. Mater.*, vol. 8, no. 8, pp. 1770–1783, Jan. 1996. [Online]. Available: <http://dx.doi.org/10.1021/cm960077f> 42

- [41] M. Sun, G. Zangari, M. Shamsuzzoha, and R. M. Metzger, "Electrodeposition of highly uniform magnetic nanoparticle arrays in ordered alumite," *Appl. Phys. Lett.*, vol. 78, no. 19, pp. 2964–2966, May 2001. [Online]. Available: <http://dx.doi.org/10.1063/1.1370986> 42
- [42] H. Zeng, S. Sun, T. S. Vedantam, J. P. Liu, Z.-R. Dai, and Z.-L. Wang, "Exchange-coupled fept nanoparticle assembly," *Appl. Phys. Lett.*, vol. 80, no. 14, pp. 2583–2585, Apr. 2002. [Online]. Available: <http://dx.doi.org/10.1063/1.1467976> 42, 102, 103
- [43] M. Willard, L. Kurihara, E. Carpenter, S. Calvin, and V. Harris, "Chemically prepared magnetic nanoparticles," *International Materials Reviews*, vol. 49, no. 3-4, pp. 125–170, 2004-06-01T00:00:00. [Online]. Available: <http://dx.doi.org/10.1179/095066004225021882> 42
- [44] C. Cannas, A. Musinu, A. Ardu, F. Orrù, D. Peddis, M. Casu, R. Sanna, F. Angius, G. Diaz, and G. Piccaluga, "Cofe₂o₄ and cofe₂o₄/sio₂ core/shell nanoparticles: Magnetic and spectroscopic study," *Chem. Mater.*, vol. 22, no. 11, pp. 3353–3361, Apr. 2010. [Online]. Available: <http://dx.doi.org/10.1021/cm903837g> 42
- [45] V. Iannotti, S. Amoruso, G. Ausanio, X. Wang, L. Lanotte, A. C. Barone, G. Margaris, K. N. Trohidou, and D. Fiorani, "Interplay between particle anisotropy and exchange interaction in fe nanoparticle films," *Phys. Rev. B*, vol. 83, no. 21, pp. 214422–, Jun. 2011. [Online]. Available: <http://link.aps.org/doi/10.1103/PhysRevB.83.214422> 42
- [46] H. Zeng, M. Zheng, R. Skomski, D. J. Sellmyer, Y. Liu, L. Menon, and S. Bandyopadhyay, "Magnetic properties of self-assembled co nanowires of varying length and diameter," *J. Appl. Phys.*, vol. 87, no. 9, pp. 4718–4720, May 2000. [Online]. Available: <http://dx.doi.org/10.1063/1.373137> 42
- [47] I. A. Al-Omari and D. J. Sellmyer, "Magnetic properties of nanostructured cosm/feco films," *Phys. Rev. B*, vol. 52, no. 5, pp. 3441–3447, Aug. 1995. [Online]. Available: <http://link.aps.org/doi/10.1103/PhysRevB.52.3441> 42
- [48] W. C. Chang, D. Y. Chiou, S. H. Wu, B. M. Ma, and C. O. Bounds, "High performance alpha-fe/nd₂fe₁₄b-type nanocomposites," *Appl.*

- Phys. Lett.*, vol. 72, no. 1, pp. 121–123, Jan. 1998. [Online]. Available: <http://dx.doi.org/10.1063/1.121446> 42
- [49] T. Yogi, G. L. Gorman, C. Hwang, M. A. Kakalec, and S. E. Lambert, “Dependence of magnetics, microstructures and recording properties on underlayer thickness in conic/cr media,” *Magnetics, IEEE Transactions on*, vol. 24, no. 6, pp. 2727–2729, 1988. [Online]. Available: <http://dx.doi.org/10.1109/20.92226> 42
- [50] J.-G. Zhu and H. N. Bertram, “Self-organized behavior in thin-film recording media,” *J. Appl. Phys.*, vol. 69, no. 8, pp. 4709–4711, Apr. 1991. [Online]. Available: <http://dx.doi.org/10.1063/1.348255> 43
- [51] P. Gaunt, “Magnetic viscosity and thermal activation energy,” *J. Appl. Phys.*, vol. 59, no. 12, pp. 4129–4132, Jun. 1986. [Online]. Available: <http://dx.doi.org/10.1063/1.336671> 44, 45
- [52] R. Street and J. C. Woolley, “A study of magnetic viscosity,” *Proceedings of the Physical Society. Section A*, vol. 62, no. 9, pp. 562–, 1949. [Online]. Available: <http://stacks.iop.org/0370-1298/62/i=9/a=303> 44, 45
- [53] L. Néel, “Le traînage magnétique,” *J. Phys. Radium*, vol. 12, no. 3, pp. 339–351, 1951. [Online]. Available: <http://hal.archives-ouvertes.fr/jpa-00234392> 44, 45
- [54] A. de Witte, K. O’Grady, G. Coverdale, and R. Chantrell, “Activation volumes of reversal in ultrafine particles and recording media,” *Journal of Magnetism and Magnetic Materials*, vol. 88, no. 1-2, pp. 183–193, Jul. 1990. [Online]. Available: <http://www.sciencedirect.com/science/article/pii/S0304885397900287> 44, 45
- [55] M. El-Hilo, K. O’Grady, R. Chantrell, and D. Dickson, “Time dependent magnetisation in systems with distributed energy barriers,” *Journal of Magnetism and Magnetic Materials*, vol. 123, no. 1-2, pp. 30–34, May 1993. [Online]. Available: <http://www.sciencedirect.com/science/article/pii/030488539390010Y> 45
- [56] E. P. Wohlfarth, “The coefficient of magnetic viscosity,” *Journal of Physics F: Metal Physics*, vol. 14, no. 8, pp. L155–, 1984. [Online]. Available: <http://stacks.iop.org/0305-4608/14/i=8/a=005> 45

- [57] W. D. Doyle, L. Varga, L. He, and P. J. Flanders, "Reptation and viscosity in particulate recording media in the time-limited switching regime," *J. Appl. Phys.*, vol. 75, no. 10, pp. 5547–5549, May 1994. [Online]. Available: <http://dx.doi.org/10.1063/1.355684> 45
- [58] H. Danan, A. Herr, and A. J. P. Meyer, "New determinations of the saturation magnetization of nickel and iron," *J. Appl. Phys.*, vol. 39, no. 2, pp. 669–670, Feb. 1968. [Online]. Available: <http://dx.doi.org/10.1063/1.2163571> 45
- [59] J. Graham, C. D., "Magnetocrystalline anisotropy constants of iron at room temperature and below," *Phys. Rev.*, vol. 112, no. 4, pp. 1117–1120, Nov. 1958. [Online]. Available: <http://link.aps.org/doi/10.1103/PhysRev.112.1117> 46
- [60] A. García-García, A. Vovk, J. A. Pardo, P. Štrichovanec, C. Magén, E. Snoeck, P. A. Algarabel, J. M. De Teresa, L. Morellón, and M. R. Ibarra, "Magnetic properties of $\text{Fe}^{\bullet}\text{mgo}$ granular multilayers prepared by pulsed laser deposition," *Journal of Applied Physics*, vol. 105, no. 6, pp. –, 2009. [Online]. Available: <http://scitation.aip.org/content/aip/journal/jap/105/6/10.1063/1.3093945> 46
- [61] H. Kronmüller, "Micromagnetism of hard magnetic nanocrystalline materials," *Nanostructured Materials*, vol. 6, no. 1-4, pp. 157–168, 1995. [Online]. Available: <http://www.sciencedirect.com/science/article/pii/0965977395000399> 46
- [62] R. Weast, *CRC handbook of chemistry and physics*, 64th ed., R. Weast, M. Astle, and W. Beyer, Eds. CRC Press Inc., Boca Raton, Florida, 1985. [Online]. Available: <http://books.google.com/books?id=Jj9CAQAIAAJ> 46, 80, 90
- [63] J. Mathon and A. Umerski, "Theory of tunneling magnetoresistance of an epitaxial $\text{Fe}/\text{mgo}/\text{Fe}(001)$ junction," *Phys. Rev. B*, vol. 63, no. 22, pp. 220 403–, May 2001. [Online]. Available: <http://link.aps.org/doi/10.1103/PhysRevB.63.220403> 46, 47, 53, 60
- [64] A. García-García, A. Vovk, J. A. Pardo, P. Štrichovanec, P. A. Algarabel, C. Magén, J. M. De Teresa, L. Morellón, and M. R. Ibarra, "Tunneling magnetoresistance in Fe/mgo granular multilayers," *Journal of Applied Physics*, vol. 107, no. 3, pp. 033 704–4, Feb. 2010. [Online]. Available: <http://dx.doi.org/10.1063/1.3298504> 47, 53, 55, 56, 107, 110, 119

- [65] C. Li and A. J. Freeman, “Giant monolayer magnetization of fe on mgo: A nearly ideal two-dimensional magnetic system,” *Phys. Rev. B*, vol. 43, no. 1, pp. 780–787, Jan. 1991. [Online]. Available: <http://link.aps.org/doi/10.1103/PhysRevB.43.780> 47, 95
- [66] S. Matsuo, T. Matsuura, I. Nishida, and N. Tanaka, “Magnetic properties of codeposited fe/mgo composite films,” *Japanese Journal of Applied Physics*, vol. 33, no. Part 1, No. 7A, pp. 3907–3912, 1994. [Online]. Available: <http://jjap.jsap.jp/link?JJAP/33/3907/> 47, 53, 95, 101
- [67] C. Kittel and P. McEuen, *Introduction to solid state physics*, 8th ed. Wiley New York, 2005. [Online]. Available: <http://books.google.com/books?id=kym4QgAACAAJ> 47
- [68] K. L. Chopra and M. R. Randlett, “Influence of a superimposed film on the electrical conductivity of thin metal films,” *J. Appl. Phys.*, vol. 38, no. 8, pp. 3144–3147, Jul. 1967. [Online]. Available: <http://dx.doi.org/10.1063/1.1710078> 47, 48
- [69] C. A. Neugebauer and M. B. Webb, “Electrical conduction mechanism in ultrathin, evaporated metal films,” *J. Appl. Phys.*, vol. 33, no. 1, pp. 74–82, Jan. 1962. [Online]. Available: <http://dx.doi.org/10.1063/1.1728531> 48
- [70] M. Jałochowski and E. Bauer, “Resistance oscillations and crossover in ultrathin gold films,” *Phys. Rev. B*, vol. 37, no. 15, pp. 8622–8626, May 1988. [Online]. Available: <http://link.aps.org/doi/10.1103/PhysRevB.37.8622> 48
- [71] J. R. Sambles, K. C. Elsom, and D. J. Jarvis, “The electrical resistivity of gold films,” *Philosophical Transactions of the Royal Society of London. Series A, Mathematical and Physical Sciences*, vol. 304, no. 1486, pp. pp. 365–396, 1982. [Online]. Available: <http://www.jstor.org/stable/37007> 48, 120
- [72] N. F. Mott, “The electrical conductivity of transition metals,” *Proceedings of the Royal Society of London. Series A, Mathematical and Physical Sciences*, vol. 153, no. 880, pp. 699–717, Feb. 1936. [Online]. Available: <http://www.jstor.org/stable/96578> 49, 50

- [73] —, “The resistance and thermoelectric properties of the transition metals,” *Proceedings of the Royal Society of London. Series A, Mathematical and Physical Sciences*, vol. 156, no. 888, pp. 368–382, Aug. 1936. [Online]. Available: <http://www.jstor.org/stable/96600> 49
- [74] N. Mott, “Electrons in transition metals,” *Advances in Physics*, vol. 13, no. 51, pp. 325–422, Jul. 1964. [Online]. Available: <http://dx.doi.org/10.1080/00018736400101041> 49
- [75] I. A. Campbell, A. Fert, and R. Pomeroy, “Evidence for two current conduction iron,” *Philosophical Magazine*, vol. 15, no. 137, pp. 977–983, May 1967. [Online]. Available: <http://dx.doi.org/10.1080/14786436708221641> 49
- [76] A. Fert and I. A. Campbell, “Two-current conduction in nickel,” *Phys. Rev. Lett.*, vol. 21, no. 16, pp. 1190–1192, Oct. 1968. [Online]. Available: <http://link.aps.org/doi/10.1103/PhysRevLett.21.1190> 49
- [77] —, “Electrical resistivity of ferromagnetic nickel and iron based alloys,” *Journal of Physics F: Metal Physics*, vol. 6, no. 5, pp. 849–, 1976. [Online]. Available: <http://stacks.iop.org/0305-4608/6/i=5/a=025> 49
- [78] P. C. van Son, H. van Kempen, and P. Wyder, “Boundary resistance of the ferromagnetic-nonferromagnetic metal interface,” *Phys. Rev. Lett.*, vol. 58, no. 21, pp. 2271–2273, May 1987. [Online]. Available: <http://link.aps.org/doi/10.1103/PhysRevLett.58.2271> 49
- [79] T. Valet and A. Fert, “Theory of the perpendicular magnetoresistance in magnetic multilayers,” *Phys. Rev. B*, vol. 48, no. 10, pp. 7099–7113, Sep. 1993. [Online]. Available: <http://link.aps.org/doi/10.1103/PhysRevB.48.7099> 49
- [80] Y. Xu and S. M. Thompson, *Spintronic materials and technology*. CRC Press, 2007, vol. 1. [Online]. Available: <http://books.google.com/books?id=jzSDQQSWw8wC> 49
- [81] S. . Tumanski, *Thin Film Magnetoresistive Sensors Series in Sensors*. Taylor & Francis, 2001. [Online]. Available: <http://dx.doi.org/10.1201/9781420033243.fmatt> 51

- [82] M. Jullière, “Tunneling between ferromagnetic films,” *Physics Letters A*, vol. 54, no. 3, pp. 225–226, Sep. 1975. [Online]. Available: <http://www.sciencedirect.com/science/article/pii/0375960175901747> 53
- [83] T. Miyazaki and N. Tezuka, “Giant magnetic tunneling effect in fe/al₂o₃/fe junction,” *Journal of Magnetism and Magnetic Materials*, vol. 139, no. 3, pp. L231–L234, Jan. 1995. [Online]. Available: <http://www.sciencedirect.com/science/article/pii/0304885395900012> 53
- [84] J. S. Moodera, L. R. Kinder, T. M. Wong, and R. Meservey, “Large magnetoresistance at room temperature in ferromagnetic thin film tunnel junctions,” *Phys. Rev. Lett.*, vol. 74, no. 16, pp. 3273–3276, Apr. 1995. [Online]. Available: <http://link.aps.org/doi/10.1103/PhysRevLett.74.3273> 53
- [85] I. Žutić, J. Fabian, and S. Sarma, “Spintronics: Fundamentals and applications,” *Rev. Mod. Phys.*, vol. 76, no. 2, p. 323, Apr. 2004. [Online]. Available: <http://link.aps.org/doi/10.1103/RevModPhys.76.323> 53
- [86] M. Nagao, N. Tanaka, and K. Mihama, “Electron microscopy of composite films of titanium and magnesium oxide,” *Jpn. J. Appl. Phys.*, vol. 26, no. Part 2, No. 3, pp. L215–L217, 1987. [Online]. Available: <http://jjap.jsap.jp/link?JJAP/26/L215/> 53
- [87] K. Takanashi, “Creation and control of spin current in solids,” *Jpn. J. Appl. Phys.*, vol. 49, no. 11, pp. 110 001–, 2010. 54
- [88] S. Takahashi and S. Maekawa, “Effect of coulomb blockade on magnetoresistance in ferromagnetic tunnel junctions,” *Phys. Rev. Lett.*, vol. 80, no. 8, pp. 1758–1761, Feb. 1998. [Online]. Available: <http://link.aps.org/doi/10.1103/PhysRevLett.80.1758> 55
- [89] A. I. Rae, *Quantum Mechanics*, 5th ed. Taylor & Francis, 2008, iSBN 978-1-58488-970-0. 55
- [90] S. J. Shin, J. J. Lee, H. J. Kang, J. B. Choi, S.-R. E. Yang, Y. Takahashi, and D. G. Hasko, “Room-temperature charge stability modulated by quantum effects in a nanoscale silicon island,” *Nano Lett.*, vol. 11, no. 4, pp. 1591–1597, Mar. 2011. [Online]. Available: <http://dx.doi.org/10.1021/nl1044692> 55

- [91] T. Zhu and Y. J. Wang, “Enhanced tunneling magnetoresistance of FeAl_2O_3 granular films in the coulomb blockade regime,” *Phys. Rev. B*, vol. 60, no. 17, pp. 11 918–11 921, Nov. 1999. [Online]. Available: <http://link.aps.org/doi/10.1103/PhysRevB.60.11918> 55
- [92] J. Inoue and S. Maekawa, “Theory of tunneling magnetoresistance in granular magnetic films,” *Phys. Rev. B*, vol. 53, no. 18, pp. R11 927–R11 929, May 1996. [Online]. Available: <http://link.aps.org/doi/10.1103/PhysRevB.53.R11927> 55, 56
- [93] S. Mitani, S. Takahashi, K. Takanashi, K. Yakushiji, S. Maekawa, and H. Fujimori, “Enhanced magnetoresistance in insulating granular systems: Evidence for higher-order tunneling,” *Phys. Rev. Lett.*, vol. 81, pp. 2799–2802, Sep 1998. [Online]. Available: <http://link.aps.org/doi/10.1103/PhysRevLett.81.2799> 55
- [94] C. Wang, Z. Guo, Y. Rong, and T. Hsu (Xu Zuyao), “A modified theoretical model on tunnelling giant magnetoresistance of granular films,” *Physics Letters A*, vol. 329, no. 3, pp. 236–243, Aug. 2004. [Online]. Available: <http://www.sciencedirect.com/science/article/pii/S0375960104009661> 55
- [95] Y. Yang, S. Shen, Q. Ye, L. Lin, and Z. Huang, “The roles of the exchange and dipole couplings on the magnetoresistance for the nanoparticle arrays,” *Journal of Magnetism and Magnetic Materials*, vol. 303, no. 2, pp. e312–e314, Aug. 2006. [Online]. Available: <http://www.sciencedirect.com/science/article/pii/S0304885306000540> 55, 56
- [96] C. Wickles and W. Belzig, “Electronic transport in ferromagnetic conductors with inhomogeneous magnetic order parameter and domain-wall resistance,” *Phys. Rev. B*, vol. 80, no. 10, pp. 104 435–, Sep. 2009. [Online]. Available: <http://link.aps.org/doi/10.1103/PhysRevB.80.104435> 57
- [97] H. Hoffmann, “Static wall coercive force in ferromagnetic thin films,” *Magnetics, IEEE Transactions on*, vol. 9, no. 1, pp. 17–21, 1973. [Online]. Available: <http://dx.doi.org/10.1109/TMAG.1973.1067560>
- [98] H. S. Jung, W. D. Doyle, and S. Matsunuma, “Influence of underlayers on the soft properties of high magnetization fcco films,” *J. Appl. Phys.*, vol. 93, no. 10, pp. 6462–6464, May 2003. [Online]. Available: <http://dx.doi.org/10.1063/1.1557653>

- [99] M. Vopsaroiu, K. O'Grady, M. T. Georgieva, P. J. Grundy, and M. J. Thwaites, "Growth rate effects in soft coFe films," *Magnetics, IEEE Transactions on*, vol. 41, no. 10, pp. 3253–3255, 2005.
- [100] W. H. Butler, X.-G. Zhang, T. C. Schulthess, and J. M. MacLaren, "Spin-dependent tunneling conductance of Fe/MgO sandwiches," *Phys. Rev. B*, vol. 63, no. 5, pp. 054416–, Jan. 2001. [Online]. Available: <http://link.aps.org/doi/10.1103/PhysRevB.63.054416> 60
- [101] C. Palmstrom, "Epitaxial Heusler alloys: New materials for semiconductor spintronics," *MRS Bulletin-Materials Research Society*, vol. 28, no. 10, pp. 725–728, 2003. [Online]. Available: <http://lib.semi.ac.cn:8080/tsh/dzzy/wsqq/MRS%20proceedings/MRS%20Bulletin/vol28/28-725.pdf> 60
- [102] S. S. P. Parkin, "Systematic variation of the strength and oscillation period of indirect magnetic exchange coupling through the 3d, 4d, and 5d transition metals," *Phys. Rev. Lett.*, vol. 67, no. 25, pp. 3598–3601, Dec. 1991. [Online]. Available: <http://link.aps.org/doi/10.1103/PhysRevLett.67.3598> 60, 61
- [103] A. E. Berkowitz, J. R. Mitchell, M. J. Carey, A. P. Young, S. Zhang, F. E. Spada, F. T. Parker, A. Hutten, and G. Thomas, "Giant magnetoresistance in heterogeneous Cu-Co alloys," *Phys. Rev. Lett.*, vol. 68, no. 25, pp. 3745–3748, Jun. 1992. [Online]. Available: <http://link.aps.org/doi/10.1103/PhysRevLett.68.3745> 61
- [104] T. Kimura, Y. Otani, and J. Hamrle, "Switching magnetization of a nanoscale ferromagnetic particle using nonlocal spin injection," *Phys. Rev. Lett.*, vol. 96, no. 3, pp. 037201–, Jan. 2006. [Online]. Available: <http://link.aps.org/doi/10.1103/PhysRevLett.96.037201> 62
- [105] T. Yang, T. Kimura, and Y. Otani, "Giant spin-accumulation signal and pure spin-current-induced reversible magnetization switching," *Nat Phys*, vol. 4, no. 11, pp. 851–854, Nov. 2008. [Online]. Available: <http://dx.doi.org/10.1038/nphys1095> 62
- [106] T. Kimura, J. Hamrle, and Y. Otani, "Estimation of spin-diffusion length from the magnitude of spin-current absorption: Multiterminal ferromagnetic/nonferromagnetic hybrid structures," *Phys. Rev. B*,

- vol. 72, no. 1, pp. 014461–, Jul. 2005. [Online]. Available: <http://link.aps.org/doi/10.1103/PhysRevB.72.014461> 62
- [107] F. J. Jedema, A. T. Filip, and B. J. van Wees, “Electrical spin injection and accumulation at room temperature in an all-metal mesoscopic spin valve,” *Nature*, vol. 410, no. 6826, pp. 345–348, Mar. 2001. [Online]. Available: <http://dx.doi.org/10.1038/35066533> 62
- [108] J. M. Kikkawa and D. D. Awschalom, “Lateral drag of spin coherence in gallium arsenide,” *Nature*, vol. 397, no. 6715, pp. 139–141, Jan. 1999. [Online]. Available: <http://dx.doi.org/10.1038/16420> 62
- [109] X. Jiang, R. Wang, R. M. Shelby, R. M. Macfarlane, S. R. Bank, J. S. Harris, and S. S. P. Parkin, “Highly spin-polarized room-temperature tunnel injector for semiconductor spintronics using mgo(100),” *Phys. Rev. Lett.*, vol. 94, no. 5, pp. 056601–, Feb. 2005. [Online]. Available: <http://link.aps.org/doi/10.1103/PhysRevLett.94.056601> 62
- [110] G. Salis, R. Wang, X. Jiang, R. M. Shelby, S. S. P. Parkin, S. R. Bank, and J. S. Harris, “Temperature independence of the spin-injection efficiency of a mgo-based tunnel spin injector,” *Appl. Phys. Lett.*, vol. 87, no. 26, pp. 262503–3, Dec. 2005. [Online]. Available: <http://dx.doi.org/10.1063/1.2149369> 62
- [111] G. Schmidt, D. Ferrand, L. W. Molenkamp, A. T. Filip, and B. J. van Wees, “Fundamental obstacle for electrical spin injection from a ferromagnetic metal into a diffusive semiconductor,” *Phys. Rev. B*, vol. 62, no. 8, pp. R4790–, Aug. 2000. [Online]. Available: <http://link.aps.org/doi/10.1103/PhysRevB.62.R4790> 62
- [112] A. T. Hanbicki, B. T. Jonker, G. Itskos, G. Kioseoglou, and A. Petrou, “Efficient electrical spin injection from a magnetic metal/tunnel barrier contact into a semiconductor,” *Appl. Phys. Lett.*, vol. 80, no. 7, pp. 1240–1242, Feb. 2002. [Online]. Available: <http://dx.doi.org/10.1063/1.1449530> 62
- [113] R. Jansen, “Silicon spintronics,” *Nat Mater*, vol. 11, no. 5, pp. 400–408, May 2012. [Online]. Available: <http://dx.doi.org/10.1038/nmat3293> 63
- [114] L. Fleet, K. Yoshida, H. Kobayashi, Y. Ohno, H. Kurebayashi, J.-Y. Kim, C. Barnes, and A. Hirohata, “Schottky barrier height in fe/gaas films,” *Magnetics*,

- IEEE Transactions on*, vol. 46, no. 6, pp. 1737–1740, 2010. [Online]. Available: http://ieeexplore.ieee.org/xpls/abs_all.jsp?arnumber=5467484 63
- [115] W. O'Mara, R. Herring, and L. Hunt, *Handbook of semiconductor silicon technology*. Noyes Publications, 1990. [Online]. Available: <http://books.google.co.uk/books?id=COcVgAtqeKkC> 63
- [116] I. Uschmann, T. Kämpfer, F. Zamponi, A. Lübcke, U. Zastrau, R. Loetzsch, S. Höfer, A. Morak, and E. Förster, “Investigation of fast processes in condensed matter by time-resolved x-ray diffraction,” *Applied Physics A*, vol. 96, no. 1, pp. 91–98, 2009. [Online]. Available: <http://dx.doi.org/10.1007/s00339-009-5187-1> 63
- [117] R. Wyckoff, *Crystal Structures*. Interscience Publishers, 1960, no. v. 4. [Online]. Available: <http://books.google.co.uk/books?id=jNwgAAAAMAAJ> 63
- [118] G. Paglia, “Determination of the structure of γ -alumina using empirical and first principle calculations combined with supporting experiments,” Ph.D. dissertation, Curtin University of Technology, Department of Applied Physics & Department of Applied Chemistry, 2004. [Online]. Available: <http://espace.library.curtin.edu.au/R?func=search-simple-go&ADJACENT=Y&REQUEST=adt-WCU20040621.123301> 63, 64
- [119] E. R. Jette and F. Foote, “Precision determination of lattice constants,” *J. Chem. Phys.*, vol. 3, no. 10, pp. 605–616, Oct. 1935. [Online]. Available: <http://dx.doi.org/10.1063/1.1749562> 63
- [120] G. A. Prinz, “Stabilization of bcc co via epitaxial growth on gaas,” *Phys. Rev. Lett.*, vol. 54, no. 10, pp. 1051–1054, Mar. 1985. [Online]. Available: <http://link.aps.org/doi/10.1103/PhysRevLett.54.1051> 63, 64
- [121] H. Hasegawa and D. G. Pettifor, “Microscopic theory of the temperature-pressure phase diagram of iron,” *Phys. Rev. Lett.*, vol. 50, no. 2, pp. 130–133, Jan. 1983. [Online]. Available: <http://link.aps.org/doi/10.1103/PhysRevLett.50.130> 64
- [122] M. Hashimoto, J. Herfort, H.-P. Schonherr, and K. H. Ploog, “Epitaxial heusler alloy $\text{Co}_2\text{FeSi}/\text{GaAs}(001)$ hybrid structures,” *Appl. Phys. Lett.*, vol. 87, no. 10, pp. 102506–3, Sep. 2005. [Online]. Available: <http://dx.doi.org/10.1063/1.2041836> 64

- [123] L. T. Vinh, J. Chevrier, and J. Derrien, “Epitaxial growth of fe-si compounds on the silicon (111) face,” *Phys. Rev. B*, vol. 46, no. 24, pp. 15 946–15 954, Dec. 1992. [Online]. Available: <http://link.aps.org/doi/10.1103/PhysRevB.46.15946> 64
- [124] C. Liu and L. Chen, “Epitaxial growth of metastable face-centered cubic co on (111) si with a thin intermediate cu layer,” *Materials Chemistry and Physics*, vol. 46, no. 2-3, pp. 233–237, Nov. 1996. [Online]. Available: <http://www.sciencedirect.com/science/article/pii/S0254058496018044> 64
- [125] K. Hamaya, K. Ueda, Y. Kishi, Y. Ando, T. Sadoh, and M. Miyao, “Epitaxial ferromagnetic fe₃si/si(111) structures with high-quality heterointerfaces,” *Appl. Phys. Lett.*, vol. 93, no. 13, pp. 132 117–3, Sep. 2008. [Online]. Available: <http://dx.doi.org/10.1063/1.2996581> 64
- [126] S. Yamada, K. Hamaya, K. Yamamoto, T. Murakami, K. Mibu, and M. Miyao, “Significant growth-temperature dependence of ferromagnetic properties for co₂fesi/si(111) prepared by low-temperature molecular beam epitaxy,” *Appl. Phys. Lett.*, vol. 96, no. 8, pp. 082 511–3, Feb. 2010. [Online]. Available: <http://dx.doi.org/10.1063/1.3330895> 64
- [127] D. Reisinger, M. Schonecke, T. Brenninger, M. Opel, A. Erb, L. Alff, and R. Gross, “Epitaxy of fe₃o₄ on si(001) by pulsed laser deposition using a tin/mgo buffer layer,” *J. Appl. Phys.*, vol. 94, no. 3, pp. 1857–1863, Aug. 2003. [Online]. Available: <http://dx.doi.org/10.1063/1.1587885> 64
- [128] *Specification sheet: ES2-PSA SAPPHIRE EPI READY POLISHED SUBSTRATE*, Rubicon Technology, Inc. 900 E. Green Street | Bensenville, IL 60106 Std. [Online]. Available: http://rubicon-es2.com/pdf/RubiconSpec_EpiPolished.pdf 65
- [129] G. Imthurn, “The history of silicon-on-sapphire,” Peregrine Semiconductor Corporation, Tech. Rep., 2012. [Online]. Available: http://www.psemi.com/articles/PSemi_SOSHHistory_73-0020-03.pdf 65
- [130] H. Wado, T. Shimizu, and M. Ishida, “Epitaxial growth of gamma - al₂o₃ layers on si(111) using al solid source and n₂o gas molecular beam epitaxy,” *Appl. Phys. Lett.*, vol. 67, no. 15, pp. 2200–2202, Oct. 1995. [Online]. Available: <http://dx.doi.org/10.1063/1.115102> 65

- [131] S. P. Dash, S. Sharma, R. S. Patel, M. P. de Jong, and R. Jansen, "Electrical creation of spin polarization in silicon at room temperature," *Nature*, vol. 462, no. 7272, pp. 491–494, Nov. 2009. [Online]. Available: <http://dx.doi.org/10.1038/nature08570> 65
- [132] O. M. J. van 't Erve, G. Kioseoglou, A. T. Hanbicki, C. H. Li, B. T. Jonker, R. Mallory, M. Yasar, and A. Petrou, "Comparison of fe/schottky and fe/al[₂]o[₃] tunnel barrier contacts for electrical spin injection into gaas," *Appl. Phys. Lett.*, vol. 84, no. 21, pp. 4334–4336, May 2004. [Online]. Available: <http://dx.doi.org/10.1063/1.1758305> 65
- [133] S. S. P. Parkin, C. Kaiser, A. Panchula, P. M. Rice, B. Hughes, M. Samant, and S.-H. Yang, "Giant tunnelling magnetoresistance at room temperature with mgo (100) tunnel barriers," *Nat Mater*, vol. 3, no. 12, pp. 862–867, Dec. 2004. [Online]. Available: <http://dx.doi.org/10.1038/nmat1256> 65
- [134] D. D. Djayaprawira, K. Tsunekawa, M. Nagai, H. Maehara, S. Yamagata, N. Watanabe, S. Yuasa, Y. Suzuki, and K. Ando, "230magnetoresistance in cofeb/mgo/cofeb magnetic tunnel junctions," *Appl. Phys. Lett.*, vol. 86, no. 9, pp. 092 502–3, Feb. 2005. [Online]. Available: <http://dx.doi.org/10.1063/1.1871344> 65
- [135] K.-R. Jeon, B.-C. Min, I.-J. Shin, C.-Y. Park, H.-S. Lee, Y.-H. Jo, and S.-C. Shin, "Electrical spin accumulation with improved bias voltage dependence in a crystalline cofe/mgo/si system," *Applied Physics Letters*, vol. 98, no. 26, p. 262102, 2011. [Online]. Available: <http://dx.doi.org/10.1063/1.3600787> 65
- [136] S. Yuasa, T. Nagahama, A. Fukushima, Y. Suzuki, and K. Ando, "Giant room-temperature magnetoresistance in single-crystal fe/mgo/fe magnetic tunnel junctions," *Nat Mater*, vol. 3, no. 12, pp. 868–871, Dec. 2004. [Online]. Available: <http://dx.doi.org/10.1038/nmat1257> 65
- [137] D. Chrisey and G. Hubler, Eds., *Pulsed laser deposition of thin films*. Wiley-VCH, May 2003, vol. 1. 68
- [138] K. K. Schuegraf, Ed., *Handbook of thin-film deposition processes and techniques: principles, methods, equipment, and applications*. Noyes Publications, 1988. 68

- [139] E. Bauer, “Phänomenologische theorie der kristallabscheidung an oberflächen. i,” *Zeitschrift für Kristallographie - Crystalline Materials*, vol. 110, no. 1-6, pp. 372–394, Jan. 1958. [Online]. Available: <http://dx.doi.org/10.1524/zkri.1958.110.1-6.372> 69
- [140] F. C. Frank and J. H. van der Merwe, “One-dimensional dislocations. ii. misfitting monolayers and oriented overgrowth,” *Proceedings of the Royal Society of London. Series A. Mathematical and Physical Sciences*, vol. 198, no. 1053, pp. 216–225, Aug. 1949. [Online]. Available: <http://rspa.royalsocietypublishing.org/content/198/1053/216.abstract> 69
- [141] M. Volmer and A. Weber, “Keimbildung in übersättigten gebilden,” *Zeitschrift für physikalische Chemie*, vol. 119, pp. 277–301, 1926. 69
- [142] L. Krastanov and I. Stranski, “Über die kristallisation von alkalihalogenidkristallen auf fluorit,” *Zeitschrift für Kristallographie*, vol. 99, no. 5, pp. 444–451, 1938. 69
- [143] G. Sauerbrey, “Verwendung von schwingquarzen zur wägung dünner schichten und zur mikrowägung,” *Zeitschrift für Physik*, vol. 155, no. 2, pp. 206–222, 1959. [Online]. Available: <http://dx.doi.org/10.1007/BF01337937> 70
- [144] P. Dhez and C. Weisbuch, *Physics, fabrication, and applications of multilayered structures*. Plenum Publishing Corporation, 1988, vol. 182. 71
- [145] I. Brodie and J. Muray, *The physics of microfabrication*. New York, Plenum Press, 1982. 72
- [146] M. Nagao, N. Tanaka, and K. Mihama, “High resolution electron microscopy of composite films of iron and magnesium oxide,” *Jpn. J. Appl. Phys.*, vol. 25, no. Part 2, No. 7, pp. L614–L616, 1986. [Online]. Available: <http://jjap.jsap.jp/link?JJAP/25/L614> 75
- [147] A. Rollett and F. Humphreys, *Recrystallization and Related Annealing Phenomena*. Elsevier Science, 2004. [Online]. Available: <http://books.google.co.uk/books?id=52Gloa7HxGsC> 75
- [148] S. Foner, “Vibrating sample magnetometer,” *Rev. Sci. Instrum.*, vol. 27, no. 7, pp. 548–548, Jul. 1956. [Online]. Available: <http://dx.doi.org/10.1063/1.1715636> 77

- [149] —, “Versatile and sensitive vibrating-sample magnetometer,” *Rev. Sci. Instrum.*, vol. 30, no. 7, pp. 548–557, Jul. 1959. [Online]. Available: <http://dx.doi.org/10.1063/1.1716679> 77
- [150] P. Thévenaz and M. Unser, “User-friendly semiautomated assembly of accurate image mosaics in microscopy,” *Microscopy Research and Technique*, vol. 70, no. 2, pp. 135–146, February 2007. [Online]. Available: <http://bigwww.epfl.ch/publications/thevenaz0701.html> 89
- [151] C. P. Bean and J. D. Livingston, “Superparamagnetism,” *J. Appl. Phys.*, vol. 30, no. 4, pp. S120–S129, Apr. 1959. [Online]. Available: <http://dx.doi.org/10.1063/1.2185850> 91
- [152] K. O’Grady, “Private communication.” 97
- [153] K. O’Grady, V. G. Lewis, and D. P. E. Dickson, “Alternating gradient force magnetometry: Applications and extension to low temperatures (invited),” *J. Appl. Phys.*, vol. 73, no. 10, pp. 5608–5613, May 1993. [Online]. Available: <http://dx.doi.org/10.1063/1.353613> 98
- [154] “Maker unknown.” 100
- [155] M. El-Hilo, K. O’Grady, T. Nguyen, P. Baumgart, and I. Sanders, “Interactions in CoPtCr/SiO_2 composite thin films,” *Magnetics, IEEE Transactions on*, vol. 29, no. 6, pp. 3724–3726, 1993. [Online]. Available: <http://dx.doi.org/10.1109/20.281282> 100
- [156] M. El-Hilo, K. O’Grady, P. Mayo, R. Chantrell, I. Sanders, and J. Howard, “The effects of different demagnetisation processes on interaction effects in thin film media,” *Magnetics, IEEE Transactions on*, vol. 28, no. 5, pp. 3282–3284, 1992. [Online]. Available: http://ieeexplore.ieee.org/xpls/abs_all.jsp?arnumber=179784 103
- [157] M. Viret, D. Vignoles, D. Cole, J. M. D. Coey, W. Allen, D. S. Daniel, and J. F. Gregg, “Spin scattering in ferromagnetic thin films,” *Phys. Rev. B*, vol. 53, no. 13, pp. 8464–8468, Apr. 1996. [Online]. Available: <http://link.aps.org/doi/10.1103/PhysRevB.53.8464> 106

- [158] J. Yu, U. Ruediger, A. D. Kent, R. F. C. Farrow, R. F. Marks, D. Weller, L. Folks, and S. S. P. Parkin, "Magnetotransport and magnetic properties of molecular-beam epitaxy Mn/Fe thin films," *J. Appl. Phys.*, vol. 87, no. 9, pp. 6854–6856, May 2000. [Online]. Available: <http://dx.doi.org/10.1063/1.372864>
- [159] P. Granberg, P. Isberg, T. Baier, B. Hjörvarsson, and P. Nordblad, "Anisotropic behaviour of the magnetoresistance in single crystalline iron films," *Journal of Magnetism and Magnetic Materials*, vol. 195, no. 1, pp. 1 – 8, 1999. [Online]. Available: <http://www.sciencedirect.com/science/article/pii/S0304885398011688>
- [160] J. Smit, "Magnetoresistance of ferromagnetic metals and alloys at low temperatures," *Physica*, vol. 17, no. 6, pp. 612–627, Jun. 1951. [Online]. Available: <http://www.sciencedirect.com/science/article/pii/0031891451901176>
- [161] A. Hirohata, "Private communication." 120, 123, 124
- [162] I. Mihai Miron, G. Gaudin, S. Auffret, B. Rodmacq, A. Schuhl, S. Pizzini, J. Vogel, and P. Gambardella, "Current-driven spin torque induced by the rashba effect in a ferromagnetic metal layer," *Nat Mater*, vol. 9, no. 3, pp. 230–234, Mar. 2010. [Online]. Available: <http://dx.doi.org/10.1038/nmat2613>
- [163] T. Kishi, H. Yoda, T. Kai, T. Nagase, E. Kitagawa, M. Yoshikawa, K. Nishiyama, T. Daibou, M. Nagamine, M. Amano, S. Takahashi, M. Nakayama, N. Shimomura, H. Aikawa, S. Ikegawa, S. Yuasa, K. Yakushiji, H. Kubota, A. Fukushima, M. Oogane, T. Miyazaki, and K. Ando, "Lower-current and fast switching of a perpendicular tmr for high speed and high density spin-transfer-torque mram," in *Electron Devices Meeting, 2008. IEDM 2008. IEEE International*, 2008, pp. 1–4. [Online]. Available: <http://dx.doi.org/10.1109/IEDM.2008.4796680>